DEPOSITION OF METHYLAMMONIUM LEAD TRI-IODIDE ORGANOMETALLIC HALIDE PEROVSKITES USING CLOSE SPACE VAPOR TRANSPORT

by

Trishelle M. Copeland-Johnson

A thesis submitted to the Faculty of the University of Delaware in partial fulfillment of the requirements for the degree of Master of Chemical Engineering

Fall 2016

DEPOSITION OF METHYLAMMONIUM LEAD TRI-IODIDE ORGANOMETALLIC HALIDE PEROVSKITES USING CLOSE SPACE VAPOR TRANSPORT

by

Trishelle M. Copeland-Johnson

Approved: _____
Robert W. Birkmire, Ph.D.
Professor in charge of thesis on behalf of the Advisory Committee

Approved: _____
Raul F. Lobo, Ph.D.
Professor in charge of thesis on behalf of the Advisory Committee

Approved: _____
Abraham M. Lenhoff, Ph.D.
Chair of the Department of Chemical and Biomolecular Engineering

Approved: _____
Babatunde A. Ogunnaike, Ph.D.
Dean of the College of Engineering

Approved: _____
Ann L. Ardis, Ph.D.
Senior Vice Provost for Graduate and Professional Education

ACKNOWLEDGMENTS

To my mother for her unfathomable amount of patience every time I called her at midnight to issue a feverish rant about my uncertain future.

TABLE OF CONTENTS

LIST OF TABLES

LIST OF FIGURES

ABSTRACT

Organometallic halide perovskites (OHPs) are a class of materials that are currently being heavily investigated as an absorber material for thin-film photovoltaic devices due to their favorable optoelectronic properties and flexible fabrication options. The first report of an OHP PV device was published in 2009 with a conversion efficiency of only 3.9% (Kojima et al. 2009; Snaith 2013) and the current most efficient research cell, certified by National Renewable Energy Laboratory (NREL), has an efficiency greater than 22.1% (NREL 2016). However, the technology is not without its challenges. The material properties of films depend on the processing conditions and the deposition technique, compromising reproducibility (Du et al. 2015). Films deposited using solution-based techniques, are especially unreliable. Solution deposition, namely one-step spin coating, is the most prominent choice due to easy accessibility for laboratory scale experiments and operation at ambient conditions. However, challenges with reproducibility, control over film thickness and uniformity, manufacturing scalability, and the lack of environmental control make it a less desirable choice for commercialization (Petrović et al. 2015). Characterization of films spun cast in this investigation were consistent with these shortcomings, exhibiting poor surface coverage, non-uniform composition, and acute sensitivity to humidity.

In contrast, vapor deposition techniques provide better control over film morphology and deposition environment, minimizing degradation of OHP films and ensuring reliable data on their material properties (Ono et al. 2016). Close space vapor transport (CSVT) is a novel, highly controllable vapor deposition technique for fabricating OHP films, originally developed for manufacturing of CdTe thin-film solar

devices. The potential of CSVT as a scalable technique for OHP PV fabrication was demonstrated in this thesis through the development of a mass transport model for predicting the deposition flux of sublimated reactants methylammonium iodide (MAI) and PbI_2 in an assembled pilot plant system. These two materials were sequentially deposited to fabricate $CH_3NH_3PbI_3$ thin-films. Flux values calculated at various source temperature and system pressures overestimated actual values obtained under the same conditions by at least an order of magnitude. Some of the assumptions used to develop the model attributed to the large deviation from the actual flux, namely a constant temperature gradient and isolation of deposition to only the designated deposition region. Furthermore, more accurate diffusivities for MAI and PbI_2 vapor are needed. Future research should focus on obtaining better estimates for reactant diffusivities through empirically instead of theoretically, quantifying the actual temperature gradient during system operation, and confirming if convective heat transport is in fact applicable to this system.

Chapter 1

ORGANOMETALLIC HALIDE PEROVSKITES (OHPs) IN PHOTOVOLTAIC (PV) TECHNOLOGY

Identifying alternatives to fossil fuels has been a demanding topic for a number of decades, as renewable sources hold the promise of minimizing the negative environmental impact and dependency associated with fossil fuels. Prominent examples of renewable energy include hydroelectric, geothermal, wind, and solar. Solar energy, namely photovoltaic (PV) technology, has gained a significant amount of attention within the past few years given its versatility and rapid technological advancements. PV technology can generate electricity in applications as small as handheld devices to residential/commercial rooftop arrays to megawatt-scale projects, offsetting peak electricity demand and dependence on grid power. Monocrystalline and multi-crystalline silicon PV are the most mature technologies, a culmination of decades of R&D and extensive financial ventures (Green 2005). Record research cell efficiency is 25.6% while the best commercial modules achieve 20% with a degradation rate in performance of about 1% per year over the course of their operational lifetime of twenty years (Jordan and Kurtz 2013; Green et al. 2015). The performance and durability of silicon PV has set the standard criteria for the commercialization of upcoming PV technologies, particularly thin-films. Thin-film PV cells are comprised of layers of semiconductor materials with thicknesses on the order of nanometers to microns, lowering material consumption and costs per unit watt of generated power while maximizing power-to-weight ratio. Some of the more

notable examples are cadmium telluride (CdTe), copper-indium-gallium-diselenide (CIGS) and amorphous silicon (Hegedus 2006; L. Chen et al. 2014; Soltanmohammad et al. 2014). Upcoming technologies include dye-sensitized and organic PV, though these have yet to reach their full potential.

Organometallic halide perovskites (OHPs) are a recently introduced class of materials that have gained extensive recognition within the PV community as an upcoming contender to that of successful CIGS and CdTe. Close space vapor transport (CSVT) is a simple yet novel vapor deposition technique for OHPs. Originally developed for the deposition of CdTe solar cells, this thesis will document the use of CSVT to deposit methylammonium lead tri-iodide OHPs or $CH_3NH_3PbI_3$ ($MAPbI_3$). This thesis will also discuss the novelty of CSVT and how the fundamentalshave been adapted to optimize the film quality of OHPs.

Background on OHPs

Defining a Perovskite

The term “perovskite” is associated with any compound that has the same structure as that of the titular perovskite, calcium titanium oxide ($CaTiO_3$), named after Russian mineralogist Lev Perovski (1792-1856) (Snaith 2013). While there are a multitude of compounds under this designation, they all share the same basic chemical composition and crystal structure of AMX_3, where A is a cation, M is a metallic ion, and X is an anion (Mitzi 2001). The figure below shows the basic structure of a perovskite.

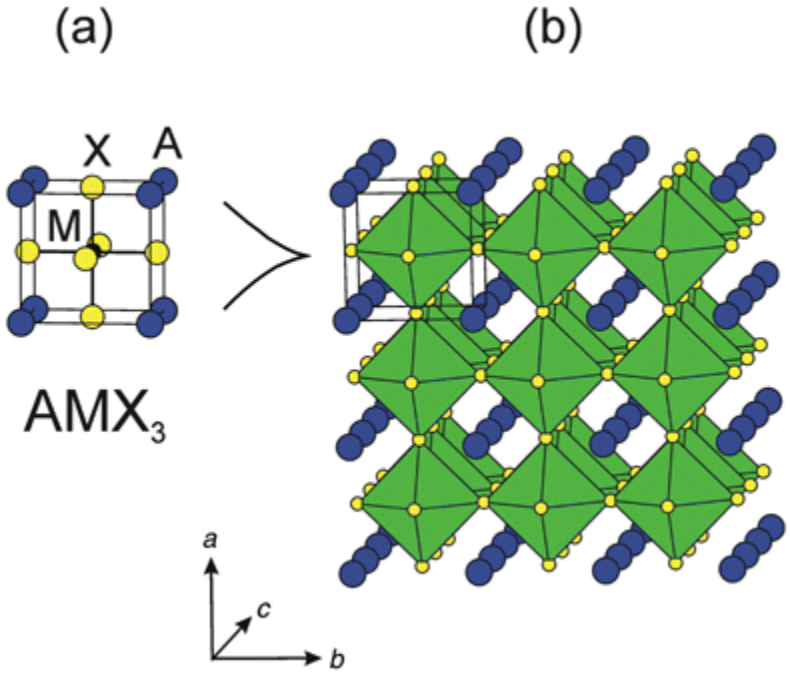

Figure 1 Unit perovskite structure depicted as a) a ball and stick model and b) a three-dimensional model, where the octagonal units are formed from the metallic ions. Reproduced from (Mitzi 2001) with permission of The Royal Society of Chemistry.

For OHPs, the cationic (A) groups are usually methylammonium $(CH_3NH_3)^+$ and formamidinium $(NH_2CH{=}NH_2)^+$ compounds, though larger variations have also been considered, including ethylammonium $(CH_3CH_2NH_3)^+$, imidazolium $[C_3N_2H_5]^+$, and hydroxylammonium $[H_3NOH]^+$ (Boix et al. 2015 Feb). Divalent lead or tin ions are normally chosen for the metallic (B) group. Finally, the anion is at least one of three members from the halide group: chloride (Cl^-), bromide (Br^-), or iodide (I^-) (Jung and Park 2014). The most notable phases are $MAPbI_3$, $MAPbCl_3$, and $MAPbBr_3$ along with mixed-halide variants, including MAPb(I,Cl), MAPb(I,Br), and $MAPbBr_{3-x}Cl_x$ (Bretschneider et al. 2014).

Application of OHPs in Photovoltaic Technology

The first investigations incorporating OHPs into semiconductor devices were in the 1990s, where they were embedded into light-emitting diodes and transistors. The application of OHPs to PV did not occur until around 2006, when $MAPbI_3$ perovskites were introduced into dye-sensitized solar cells (DSSC) in an effort to produce thinner cells with better performance. The major turning point was in 2009 when the first peer-reviewed journal article involving these perovskite DSSCs was published by Miyasaka *et al*. However, the devices they produced quickly degraded due to the perovskite's solubility in the polar electrolyte of the cell (Snaith 2013). Later investigations uncovered the potential of OHPs for absorbing materials for solar cells. Sufficient modifications made to the DSSCs established the meso-superstructured or mesoporous solar cells (MSSC) perovskite-based PV architecture, one of the most complex designs, shown in the figure on page 5. The main feature of this design is that the electron transporting material (ETM) is embedded within the hole-transporting layer (HTM), comprised of TiO_2 or AlO_2 nanoparticles coated in the perovskite suspended in the medium.

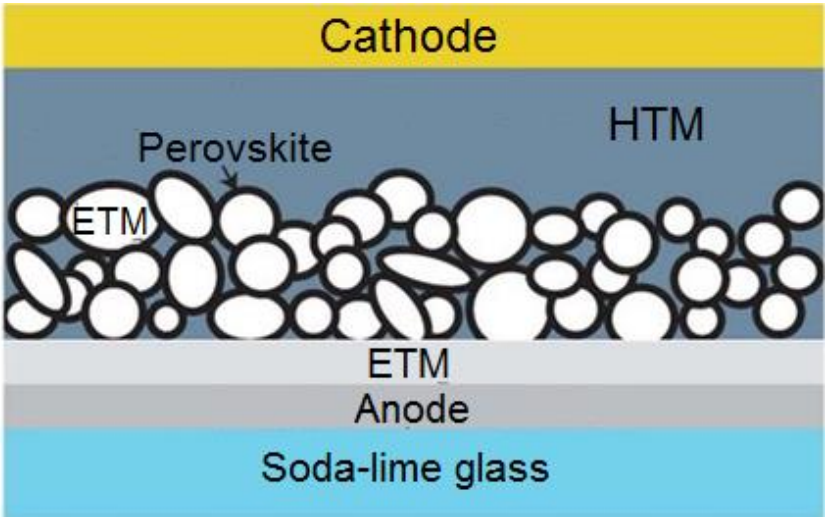

Figure 2 Diagram of an MSSC, depicting the ETM nanoparticles coated in the perovskite absorber layer, suspended in the HTM. Reprinted by permission from Macmillan Publishers Ltd: [Nature Materials] (Loi and Hummelen 2013), copyright (2013).

By 2012, perovskite solar cells with conversion efficiencies around 9.3% had been developed (Kim et al. 2012) . A year later, Snaith developed perovskite PV cells through vapor deposition techniques reaching efficiencies around 15.6% (Liu et al. 2013), exhibiting the more simplified planar heterojunction design where a continuous layer of perovskite was sandwiched in between the HTM and ETM materials, illustrated below.

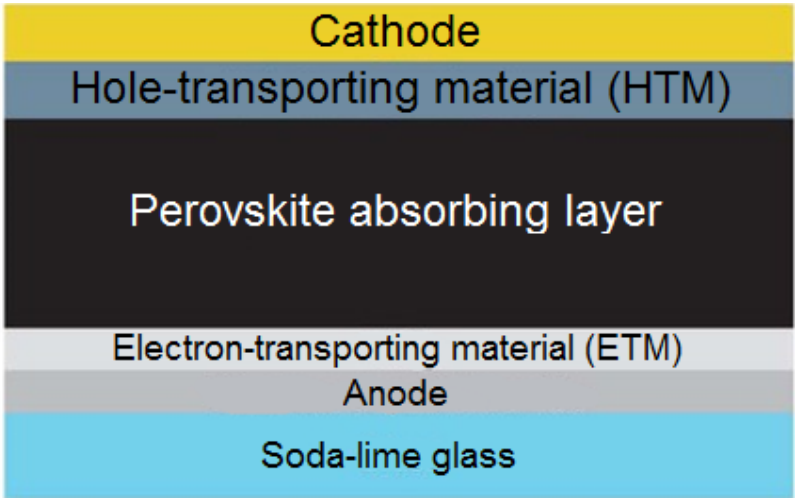

Figure 3 Diagram of a planar heterojunction photovoltaic cell featuring the continuous perovskite, HTM, and ETM layers. Reprinted by permission from Macmillan Publishers Ltd: [Nature Materials] (Loi and Hummelen 2013), copyright (2013).

In 2015, researchers at École polytechnique fédérale de Lausanne (EPFL) obtained National Renewable Energy Laboratory (NREL) certification for a device exhibiting 21 % conversion efficiency. The current record is 22.1% (NREL 2016).

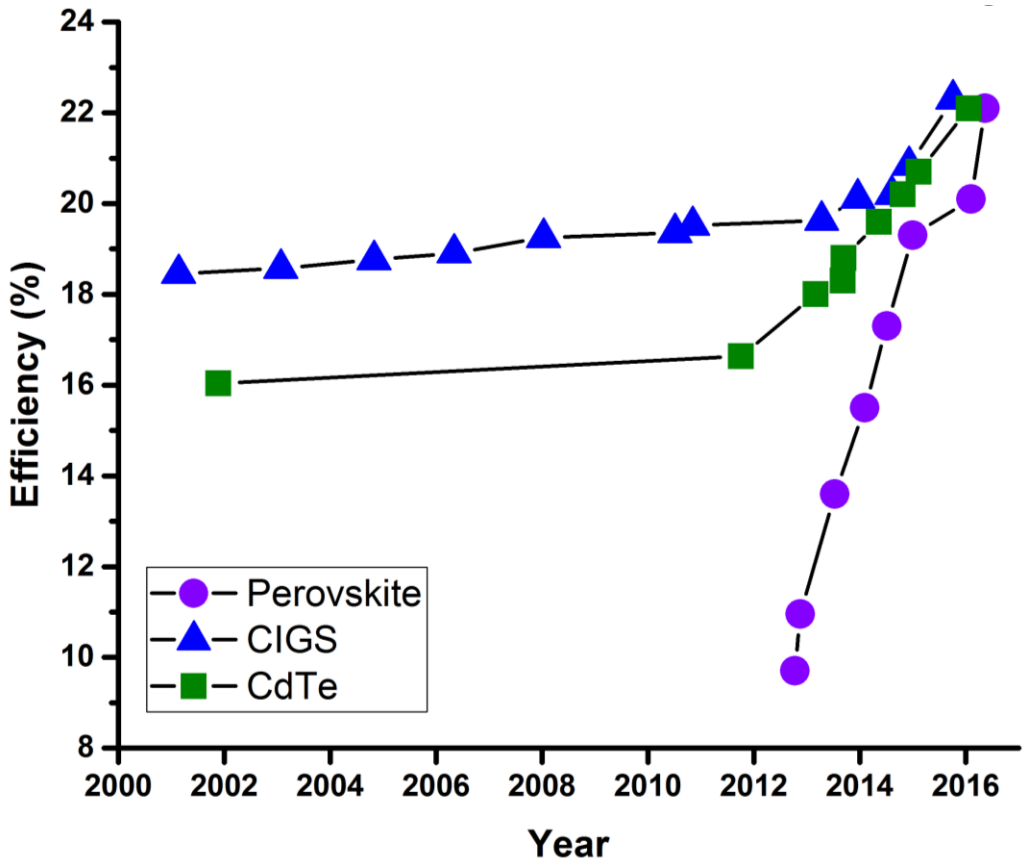

Figure 4 NREL-certified conversion efficiencies for perovskite thin-film PV versus CIGS and CdTe from 2000 to present. The first certified perovskite PV cell was not recorded until five-years after its initial debut in the publication by Miyasaka *et al.* (NREL 2016).

This rapid development is primarily attributed to the optoelectronic properties of the material. The band gap of these perovskites can be tuned between 1.5 and 3.1 eV, depending on the A, B, and X site (Bretschneider et al. 2014). Furthermore, OHPs exhibit fast separation and high mobility of charges formed from photon absorption, resulting in minimal recombination (Ponseca et al. 2014; Stranks et al. 2014). These compounds also benefit from a manufacturing standpoint since they can be

synthesized at temperatures as low as 100°C, prompting versatile processing conditions and deposition onto different substrates. In fact, films have been generated using a variety of deposition techniques, including spin coating, spray-coating, airbrushing, and thermal evaporation under both ambient and vacuum (Liu et al. 2013; Chiang et al. 2014; Ma et al. 2014; Sessolo et al. 2015; Zhou et al. 2015; Ramesh and Boopathi 2015; Boopathi et al. 2015 Feb 19).

Research opportunities stem from efforts to commercialize OHPs as PV absorbers, elucidating their material properties, extending their operational lifetimes and exploring alternative formulations. Long-term stability is a concern since OHPs are soluble in polar solvents, making humidity a major issue. Degradation from temperature, atmosphere, and UV radiation has also been documented (Leijtens et al. 2013; Aristidou et al. 2015; Murugadoss et al. 2015; Hailegnaw et al. 2015; Conings et al. 2015 Jun 1). Lead poses a toxicological issue, given its detrimental environmental and health impacts. Tin is popular alternative but devices incorporating the tin-based perovskites are inferior in performance due to the chemical instability of element in the desired +2 oxidation state (Jung and Park 2014; Noel et al. 2014). The knowledgebase on OHP thermodynamic, optoelectronic, crystallographic, and chemical properties is still limited. Standardized references on basic parameters, such as reaction rate constant, heat of sublimation, and melting point have yet to be published. Consequently, the lack of a reliable library of material properties and sensitivity to changes in deposition processing variables has spurred little consensus in published characterization data (2015).

The minimal conditions for synthesizing OHP films has resulted in the development of variety of solution and vapor-based deposition techniques. Solution-based techniques introduce the OHP reactants dissolved in a solvent at different stoichiometric ratios simultaneously or sequentially. Notable techniques include spin coating, spray coating, and dip coating (Petrović et al. 2015).

Deposition of OHPs using Solution-Based Techniques

Spin coating is a notable deposition technique that is used in the electronics industry for applications like dispensing photoresists onto silicon wafers and protective coatings on compact and digital versatile disks (Krebs 2009). The technique is one of the most prominent choices for depositing OHPs (Burschka et al. 2013; Chiang et al. 2014; Sadhanala et al. 2014; Boopathi et al. 2015 Feb 19; Smecca et al. 2016). Spin coating involves depositing a minute amount of solvent onto a surface. The surface is then spun at a high speed for a short period of time, applying large levels of centrifugal forces to spread out the material, forming a thin-film. Afterwards, the film is thermally annealed, removing excess solvent. The thickness and morphology of the film are influenced by multiple factors, including spin speed, temperature, and the solvent's viscosity (Krebs 2009). Spin coating of OHPs is normally performed in one step using a solution that contains both reactants. The perovskite film is formed upon driving off the excess solvent during the annealing stage (Petrović et al. 2015). Efforts to optimize the morphology of films have prompted the deposition of dissolved reactants individually. This two-step spin coating technique has shown promise to produce higher quality films and better performing devices (Burschka et al. 2013; Bi et al. 2014).

Spray pyrolysis deposits uniform layers from uniformly sized droplets of a dilute solution through ultrasonic or electrostatic methods. Ultrasonic spray pyrolysis utilizes carrier gases while electrostatic spray pyrolysis relies on a high voltage to generate a solution aerosol, establishing a potential difference between the nozzle and the substrate to ensure uniform distribution (Petrović et al. 2015). Film properties, such as film morphology and crystallinity, are influenced by substrate temperature, solution concentration, solvent type, and deposition rate (Mooney and Radding 1982). Barrows et al. formed I-Cl mixed-halide OHP films using ultrasonic spray coating. Homogeneous films were deposited from dilute solutions with minimal material loss, but moderate surface coverage (> 85%). Planar heterojunction PV cells incorporating these films as absorber layers displayed a maximum conversion efficiency (η) of 11.1%, short-circuit current (J_{SC}) of 16.8 mA/cm^2, open circuit voltage (V_{OC}) of 0.92 V and fill factor (FF) of 72% (Barrows et al. 2014).

Dip coating involves submerging a substrate into the solution. After a period of time, the solvent is slowly removed and dried, producing a uniform film. The nature of the film is governed by gravitational forces, inertia along with the surface tension and viscous drag of the solution along the substrate (Petrović et al. 2015). Dip coating is usually employed as a second step in sequential deposition of reactants using spin coating (Kulkarni et al. 2014; Zhu et al. 2014).

Depositing OHPs using Vapor-Based Techniques

Vapor deposition is a scalable process that operates under more stringent environmental conditions, producing higher purity films with nominal control over stoichiometry, ability to deposit multiple layers, and flexibility in substrate selection (Ono et al. 2016). The technique usually operates under high vacuum conditions,

increasing the rate of deposition and uniformity without relying in more extreme processing temperatures. Deposition can occur either under the presence of an inert gas, minimizing the intrusion of moisture, or with ambient air (Luo et al. 2015; Peng et al. 2015). Properties of the final perovskite film are closely governed by substrate temperature, system pressure, the stoichiometric ratio of the reactants, and morphology of the metallic halide precursor film (Wang et al. 2015; Yang et al. 2015). Unlike solution-based deposition, an annealing step is not mandatory. While the annealing primarily aids in sublimating excess organic reactant, such as methylammonium iodide, it appears to make negligible changes to the crystallinity of the OHP film or the performance of the PV device, potentially eliminating an energy intensive step that is necessary for solution-deposited films (Wang et al. 2015). Elimination of solvents results in OHP PV cells that exhibit better stability and performance than counterparts containing solution-deposited absorber layers. For instance, Leyden and colleagues fabricated planar heterojunction PV devices incorporating formamidinium perovskites that exhibited stable performance for 155 days (Leyden et al. 2015). This is most likely due to the ousting of impurities from high temperature processing and no solvent usage to accelerate moisture-induced degradation (Wang and Chen 2015). Liu and colleagues conducted a comparative study between the morphology, crystallography, and performance of planar heterojunction devices incorporating one-step spun-cast versus vapor-deposited $MAPbI_{3-x}Cl_x$ films. Films fabricated through dual-source deposition were highly uniform in terms of texture and thickness. However, spun-cast films consisted of discontinuities where the underlying TiO_2 layer could be seen. Additionally, spun-cast films exhibited varying film thickness. For instance, SEM cross-section noted

thicknesses between 50 to 410 nm. Devices incorporating solution-deposited films exhibited a V_{OC} of 0.84 V, J_{SC} of 17.6 mA/cm^2, FF of 0.58, and η of 8.6%. In contrast, the best performing devices with vapor deposited OHP films had a V_{OC}, J_{SC}, FF, and η of 1.07 V, 21.5 mA/cm^2, 0.67, and 15.4 %, respectively (Liu et al. 2013). Du compared $MAPbI_3$ films formed from reacting PbI_2 precursor films, deposited via one-step spin coating, with MAI sublimed into a vapor versus dissolved into a solution. Spun cast films exhibited discontinuous arrangement crystals, sporting obvious voids. Films produced from vapor deposition resulted in denser, more uniform films comprised of vertically oriented crystalline columns, ideal for charge transport. As a result, the corresponding devices displayed a V_{OC}, J_{SC}, FF, and η of 0.89 V, 15.7 mA/cm^2, 0.58, and 8.1%, respectively. In contrast, the solution-based devices only obtained V_{OC}, J_{SC}, FF, and η of 0.80 V, 11.8 mA/cm^2, 0.61, and 5.8%, respectively (Du et al. 2015). In both instances, the highest performing solar cell devices incorporated vapor deposited absorber layers.

Physical vapor deposition (PVD) and chemical vapor deposition (CVD) are the two general categories of techniques. Mattox in the *Handbook of Physical Vapor Deposition* defines PVD as:

> ...atomistic deposition processes in which material is vaporized from a solid or liquid source in the form of atoms or molecules and transported in the form of a vapor through a vacuum or low pressure gaseous (or plasma) environment to the substrate, where it condenses (Mattox 2010).

He further distinguishes CVD as:

> …deposition of atoms or molecules by the high temperature reduction or decomposition of a chemical vapor precursor species, which contains the material to be deposited (Mattox 2010).

PVD can also involve reactions of thermally sublimated materials with other substances already deposited onto the substrate, present in the vapor phase, or with the deposition atmosphere (Mattox 2010). However, some attribute this characteristic to define CVD. For instance, Kern and Schuegraf introduce the technique as:

> …materials synthesis process whereby constituents of the vapor phase react chemically near or on a substrate surface to form a solid product (Kern and Schuegraf 2001).

This interpretation of CVD is applied to some deposition techniques that have been developed for OHPs. For example, Leyden and colleagues arranged a deposition system where $PbCl_2$-coated substrates heated to an optimal temperature of 130 °C are exposed to sublimated MAI transferred via inert carrier gas. The technique is coined as "hybrid CVD" given that the product is presumed to be a solid solution of two halides, formed from a heterogeneous reaction between the MAI vapor and $PbCl_2$ film (Leyden et al. 2014). However, based on Mattox's definition of CVD, MAI has not been reduced or decomposed only stimulated to undergo a physical phase change, a quality that is more attributed with PVD. For the purposes of this discussion, the Mattox definitions will be applied. Despite differences in the interpretation of what constitutes PVD versus CVD, the design of their respective systems share similar components. A basic schematic of a vapor deposition system is shown below on page 15. The major components include a chamber pumped down to low pressures (< 100 Torr) with the source heated by a coiled filament. The sublimed material then travels to the substrate that is maintained at a lower temperature through a cooling system, minimizing the risk of re-sublimation of the condensing material.

Alluded to by Leyden's technique, vapor deposition of OHPs can also be performed in one-step/co-evaporation or two-step/sequential sequences. Co-evaporation involves simultaneously releasing of the OHP reactants into the deposition chamber, prompting formation of the perovskite once the sublimed materials make contact with the substrate kept at a lower temperature than that of the sources. The alternative approach is to introduce the reactants in succession, depositing the metal halide precursor layer, followed by an organic halide reactant while the substrate is heated around 100ºC. Otherwise, the organic precursor would decompose or re-sublimate if deposited first (Ono et al. 2016).

Both approaches have produced higher performing devices compared to that of solution-based deposition. However, reproducibility is a challenge with co-evaporation without precise initial calibration to control film thickness, which is more difficult for organic compounds, like the ammonium halides. Deposition of MAI is particularly difficult to control due to its lower molecular weight and volatility compared to the metallic halide precursor (Yang et al. 2015). Sequential deposition usually results in more uniform films exhibiting larger grain sizes by decoupling the processes, allowing for optimization of processing variables pertaining to each reactant (C.-W. Chen et al. 2014).

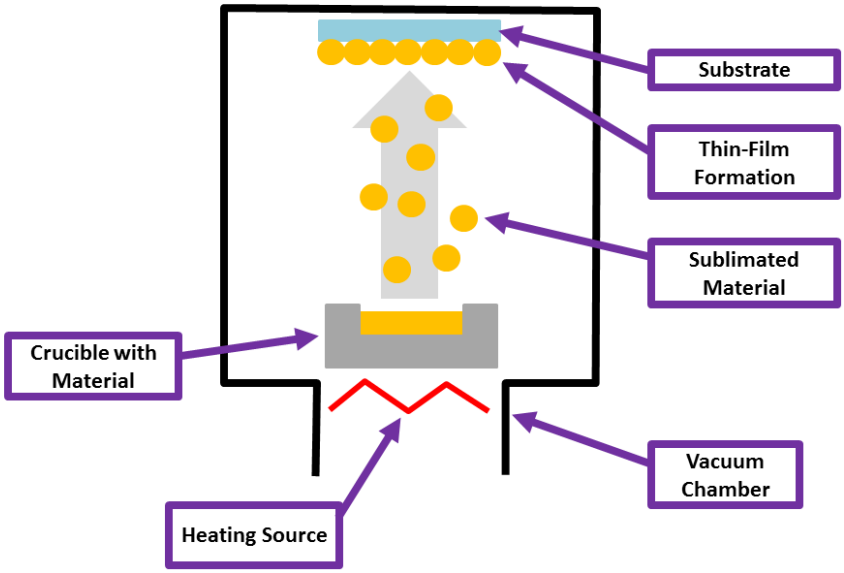

Figure 5 Basic schematic of the major components of a vapor deposition system

CSVT is a sequential physical vapor deposition process that occurs over a deposition length on the order of millimeters. The main components of the system, shown in the figure on page 16, are: 1) two susceptors used to independently heat the source and substrate, allowing greater control over the mass transport of the sublimating material and properties of the fabricated film, 2) masks and spacers made out of an insulating material to govern the deposition area and deposition height, respectively. The insulating spacers placed in between the susceptors also thermally isolate the two regions, maintaining the substrate at a lower temperature than that of the source without relying on a coolant system. The independent variables that govern

deposition rate in this system are the source temperature, substrate temperature, deposition height, deposition time, and system pressure.

CSVT was originally developed for depositing CdTe and is also referred to as close-space sublimation. Depositing CdTe films requires the source to be heated to temperatures above 500 ºC, decomposing the material into Cd and Te_2 vapors. The sublimated product then reforms on the surface of the substrate, forming a film at a specified thickness, grain size, and texture, which influence optoelectronic properties, notably conductivity.

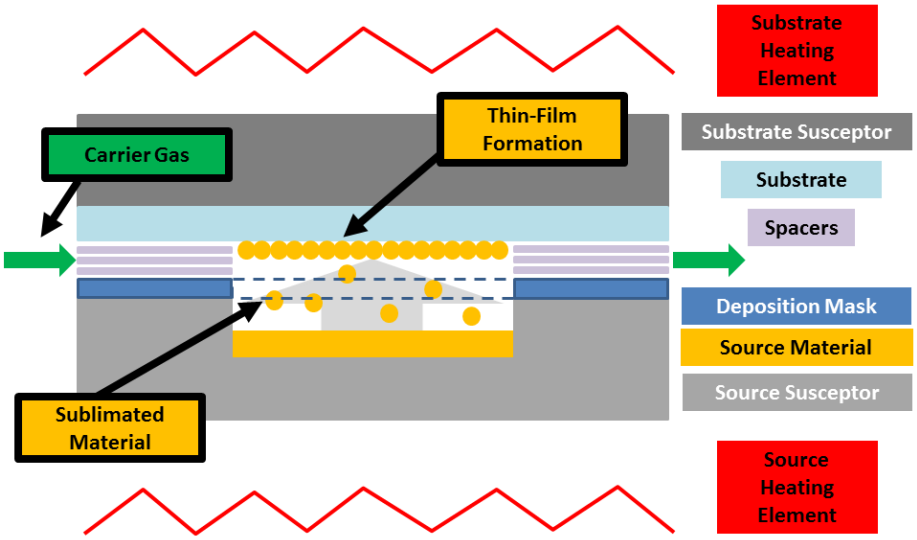

Figure 6 Cross-sectional schematic of a CSVT system. Dashed lines correspond to open region of deposition mask.

CSVT shows potential as a novel, scalable approach for rapid fabrication of continuous, uniform, homogeneous OHP films. Akin to the advantages of vapor deposition, films deposited using CSVT are much more resilient to the ambient environment, unlike their solution-deposited counterparts. Independent temperature control over the source and substrate allows for simultaneous deposition and annealing without breaking vacuum, simplifying the fabrication process and lowering the risk of moisture intrusion. Furthermore, close-proximity between the substrate and source minimizes material losses due to mass transport. As a result, films can be fabricated on the order of a few minutes with minimal material consumption, maximizing the number of deposition runs before replenishing stock. Other vapor fabrication procedures are usually either extensively long to compensate for untargeted deposition onto the substrate or include an additional annealing step between 20 to 60 minutes (Liu et al. 2013; Gao et al. 2015; Liang et al. 2015; Jung et al. 2016). For instance, while Liang and colleagues fabricated $MAPbI_3$ perovskite films using a simultaneous vapor deposition approach in only 15 minutes, they added an additional 20 minutes for annealing for a total fabrication time of 35 minutes, not including start-up and cool-down procedures (Liang et al. 2015). The remainder of this document will expand further on the advantages of CSVT with respect to other popular techniques, notably spin coating, and how is adapted for fabricating OHPs. Chapter 2 will delve into the disadvantages of spin coating OHPs documented both in literature and empirically, reinforcing the advantages of vapor deposition. Chapter 3 will follow-up with a detailed discussion on the novelty of CSVT as a vapor deposition technique for OHPs and establish a theoretical model for predicting deposition flux. Chapter 4 will evaluate the accuracy of the model, comparing actual deposition data to computed

values and overview potential sources of error. Finally, chapter 5 will summarize the major topics of the thesis and suggestions for future work.

Chapter 2

SPIN COATING DEPOSITION OF ORGANOMETALLIC HALIDE PEROVSKITES

Overview of Spin Coating OHP Films

The discussion of spin coating in Chapter 1 noted its establishment in the semiconductor industry, general operation, and as a popular choice for depositing OHPs. The foundation of fabricating OHP films for solar cells is marked by spin coating, making it a technique worthy of discussion, especially to reinforce the notoriety of CSVT. The technique, depicted on page 20, involves depositing a minute amount of a solution containing the precursor solute onto a substrate that is attached to a fixture that rotates at a high speed, usually on the order of 3000 to 10000 revolutions per minute (RPMs). As the substrate spins, the solution spreads out creating a thin film across the surface. Afterwards, a post-annealing step is included to evaporate any excess solvent and generate a crystalline film. The thickness and morphology of spin-cast films are subject to a number of variables, including spin speed, solution viscosity, and volatility of the solvent (Krebs 2009).

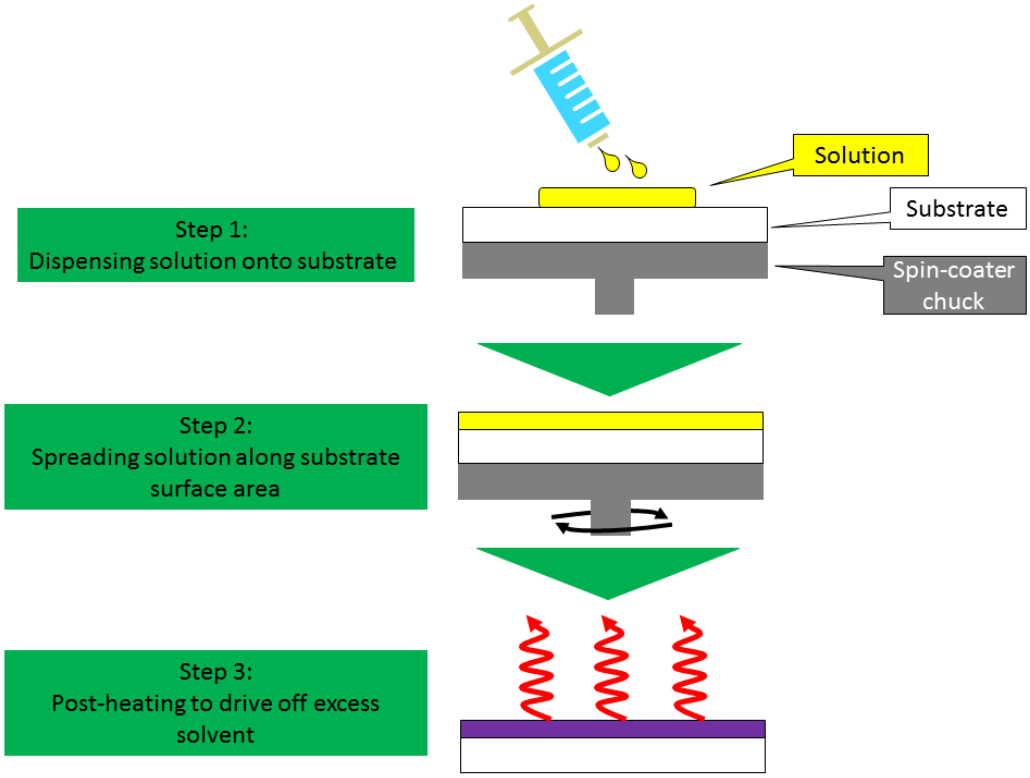

Figure 7 Schematic depicting standard spin coating technique

Spin coating has been a popular choice for depositing OHP thin-films due to its simplicity and accessibility for conducting bench top experiments (Ono et al. 2016). Spin coating deposition of OHPs is divided into two major classes: simultaneous and sequential deposition techniques. Simultaneous or one-step spin coating is the more preferable of the two, due to its obvious simplicity, depositing a solution containing both reactants usually dissolved in dimethyl sulfoxide (DMSO), dimethylformamide (DMF), or gamma-butyrolactone (GBL). The films are then incorporated into planar heterojunction or mesoporous PV architectures. For instance, Liu *et al*. developed planar heterojunction devices incorporating a $MAPbI_{3-x}Cl_x$ perovskite absorber deposited using the simultaneous approach. The cells exhibited a η of 8.6%, J_{SC} of

17.6 mA/cm^2, V_{OC} of 0.84 V and FF of 0.58 (Liu et al. 2013). Gonzalez-Pedro *et al*. fabricated a similar architecture, producing cells with η of 8.5%, V_{OC} of 0.95 V, J_{SC} of 17.5 mA/cm^2, and FF of 0.51 (Gonzalez-Pedro et al. 2014). In contrast, sequential or two-step spin coating involves depositing the dissolved reactants independently. Normally, the metallic halide is initially dispensed, followed by the organic halide. Afterwards, the film is annealed, inducing the reaction to form the OHP (Jung and Park 2014). Two-step spin coating has been documented to produce higher quality films and subsequent devices versus its counterpart (Im, Kim, et al. 2014). Burschka *et al*. first reported the use of sequential OHP formation involving $MAPbI_3$ absorber layers deposited by first spin coating a solution of 462 mg/ml PbI_2 in DMF heated at 70 ºC on the TiO_2 mesoporous layer and then dip-coating the PbI_2/TiO_2 coated substrate into a 10 mg/ml solution MAI dissolved in 2-propanol. An immediate color change was indicative of an instant conversion of the PbI_2 into $MAPbI_3$. The best devices attained a certified η of 14.1%, J_{SC} of 21.3 mA/cm^2, V_{OC} of 1.0 V and FF of 66% (Burschka et al. 2013). Ko *et al*. also generated $MAPbI_3$ mesoporous devices with the best cells performing at an average η of 15.31% with an V_{OC} of 1.01 V, J_{SC} of 20.71 mA/cm^2, and FF 0.73 (Ko et al. 2015 Mar 16). Unlike one-step spin coating, a majority of similar investigations employ two-step deposition to produce mesoporous PV devices (Bi et al. 2014; Im, Kim, et al. 2014; Im, Jang, et al. 2014; Ko et al. 2015 Mar 16). But, planar heterojunction devices have also been produced (Ito et al. 2015).

Shortcomings of Depositing OHPs Using Spin Coating

Despite its simplicity, spin coating is not an all-encompassing technique. Spin coating is not compatible with industry-level continuous processes, thwarting prospects of low-cost commercialization of OHP PV devices. Furthermore, generating

stable, uniform, continuous films is a challenge. As mentioned before, the properties of the resulting film depend on a number of factors, including the viscosity and volatility of the solvent used to generate the precursor solution. A very volatile solvent can evaporate prematurely during deposition, compromising proper film formation and introducing deleterious defects (Krebs 2009). Also, incomplete solvent evaporation may interfere with the formation of a continuous perovskite layer, subsequently decreasing performance of the assembled device. For instance, Dongqin and colleagues synthesized $MAPbI_3$ films using a sequential approach, dipping spun-cast PbI_2 films into a solution of isopropyl alcohol (IPA) and MAI. Unreacted PbI_2 was observed in x-ray diffraction (XRD) patterns of $MAPbI_3$ films and was attributed to the incomplete conversion due to residual IPA (Bi et al. 2014). The impact of the residue was evident when comparing the characteristics of mesoporous PV devices incorporating perovskite layers that were subsequently rinsed with dichloromethane. Devices with rinsed films reached an average η of 12.4%, V_{OC} of 0.97 V, J_{SC} of 21.1 mA/cm^2, and FF of 0.64. In contrast, those without the additional rinsing step achieved an average η of 11.5% when heated to 100 ºC to drive off excess IPA, but only 8.8% when left to dry at room temperature. V_{OC} also decreased to 0.91 and 0.84 V, respectively, likely due to residual IPA still present in the film.

One-step spin coating, arguably the most popular choice for depositing OHP films, is no exception. Films suffer from poor surface coverage and film non-uniformities. In terms of devices, poor surface coverage introduces shunt paths that deviate charge carriers from successfully converting captured photons to electricity, hereby diminishing conversion efficiency (Eperon et al. 2014). Thickness non-uniformities can also interfere with efficient charge separation.

Minimizing these complications is a challenge. Some investigators have attempted to improve film morphology and surface coverage by adjusting processing parameters, such as spin speed and post-annealing conditions. For instance, Sailba and Dualeh studied the impact of annealing on $MAPbI_{3-x}Cl_x$ films. Sailba's films were deposited under a nitrogen atmosphere at ambient pressure using a one-step spin coating technique from a 40 wt% solution comprised of a 3:1 molar ratio of $PbCl_2$ and MAI, respectively, dissolved in DMF. The films were then annealed on a hot plate at a ramp rate of 5 ºC/5 min to a final temperature of 100 ºC. Afterwards, the final step of the annealing process was split into two approaches. The first was maintaining 100 ºC for 45 minutes. The second approach was heating at 100 ºC for an additional 5 minutes and then immediately ramping to 130 ºC for 5 minutes. Films were then incorporated into a planar heterojunction and alumina nanoparticle mesoporous PV architectures. Grazing-incidence x-ray diffraction (GIXRD) and SEM unveiled that films rapidly heated to 130 ºC exhibited more uniform micron-sized grains than those that were continuously heated at 100 ºC, observed to contain grain sizes ranging from 100 to 1000 nm. However, the planar heterojunction devices outperformed the mesoporous devices. This is most likely due to higher surface coverage (≥ 95%) compared to that of the mesoporous films (75-85%). Planar heterojunction devices that included flash-annealed absorber layers performed marginally better than their moderately heated counterparts. On average, the J_{SC} was 19.0 versus 17.9 mA/cm^2, V_{OC} was 0.91 V versus 0.92 V, FF 0.63 versus 0.61, and η was 10.7 versus 9.9 for flash-annealed versus moderately-annealed devices, respectively. In contrast, amongst the nanoparticle alumina mesoporous devices, those with perovskite layers that had been continuously heated at 100 ºC performed better than their flash-annealed

counterparts. On average, the J_{SC} was 17.5 versus 17.7 mA/cm^2, V_{OC} was 0.91 V versus 0.92 V, FF 0.44 versus 0.53, and η was 6.9 versus 8.4 for flash-annealed versus moderately-annealed devices, respectively (Saliba et al. 2014).

Dualeh and colleagues systematically adjusting annealing parameters for the $MAPbI_{3-x}Cl_x$ films they deposited using one-step spin coating. They documented the impact of annealing temperature, from ambient to 200 ºC on films deposited onto mesoporous TiO_2 layers. Film morphology and subsequent impact on device performance was documented using SEM, UV/Vis spectroscopy, and XRD. A minimum temperature of 80 ºC was required to successfully form the perovskite. Below this threshold, there is insufficient energy to drive off excess solvent and send the reaction to completion. The optimum region for annealing was between 80 ºC and 100 ºC. However, surface coverage was consistently poor at all temperatures. At higher temperatures, the product forms islands that do not converge into a continuous film and exhibit higher levels of PbI_2, suggesting temperature-induced degradation. The best device performance recorded had a V_{OC} 0.938 V, J_{SC} 18.37 mA/cm^2, FF of 0.68, and η 11.66% (Dualeh, Tétreault, et al. 2014).

Eperon *et al.* also reported difficulties from optimizing surface coverage of OHP films studying of $MAPbI_{3-x}Cl_x$ by changing deposition parameters, such as types of solvents, solute concentrations, and spin speeds, and annealing conditions. Films generated from more volatile solvents, such as DMF, exhibited higher surface coverage than those fabricated with lower volatility solutions, for example using DMSO or n-methyl-2-pyrrolidone. Optimal coverage of approximately 90% was noted between annealing temperatures of 90 ºC and 100 ºC. Increasing the annealing temperature above this range decreased the frequency of pinholes but resulted in the

formation of larger agglomerates. Film thickness also played a role, governed by solute concentration and spin speed. Films greater than 500 nm and annealed at 95 ºC corresponded with a surface coverage above 90%. But even with optimization of fabrication conditions, the best cell generated had a η of only 11.4%, FF of 0.64, V_{OC} of 0.89 V, and J_{SC} of 20.3 mA/cm^2 (Eperon et al. 2014). To expand on these findings, additional empirical studies were conducted on both $MAPbI_{3-x}Cl_x$ and $MAPbI_3$, the two most studied OHPs, deposited using one-step spin coating.

Optimizing the Spin Coating Processing Variables for Depositing $MAPbI_{3-x}Cl_x$ Films

Attempts were made in this investigation to adjust the solution stoichiometry and deposition parameters of $MAPbI_{3-x}Cl_x$ films to improve in film quality, notably surface coverage, with marginal success. The compound is normally synthesized from a precursor solution comprised of 2.64 M MAI to 0.88 M $PbCl_2$, where the iodide and chloride are provided by the organic and inorganic reactants, respectively (Lee et al. 2012). However, the halide does not necessarily need to be introduced through that route. MACl can be substituted for $PbCl_2$ and PbI_2 for MAI. In fact, both lead halides and organic halides can be combined in solution, as shown in the table on page 26, adjusting the precursor chloride to iodide ratio while maintaining the same overall composition. Four trials, each consisting of two replicates, were generated for each experimental group by depositing 0.20 mL of the corresponding solution onto soda-lime glass coated with a fluorinated tin-oxide (FTO) and spinning at 1000 RPM for 60s. Afterwards, the films were immediately placed on a hot plate and annealed at 100 ºC for 60 minutes. The entire fabrication was performed at ambient atmospheric conditions. Images of the films formed from each experimental set are depicted below.

Films belonging to set A exhibited the most striking color distinction, exhibiting a reddish orange hue versus the anticipated dark greyish hue normally associated with $MAPbI_3$ and $MAPbI_{3-x}Cl_x$. Sets B and D, both containing high chloride to halide ratio, displayed film non-uniformities through the patches of yellowish-green against grey.

Table 1 Precursor solution conditions to monitor effects chloride to iodide ratio in OHP thin film processing by spin coating

Set	Condition	M_{MAI}	M_{MACl}	M_{PbI2}
A	50% PbI2 + 50% PbCl2	2.64	---	0.44
B	50% PbI2 + 50% PbCl2	---	2.64	0.44
C	50% MAI + 50% MACl	1.32	1.32	0.88
D	50% MAI + 50% MACl	1.32	1.32	---

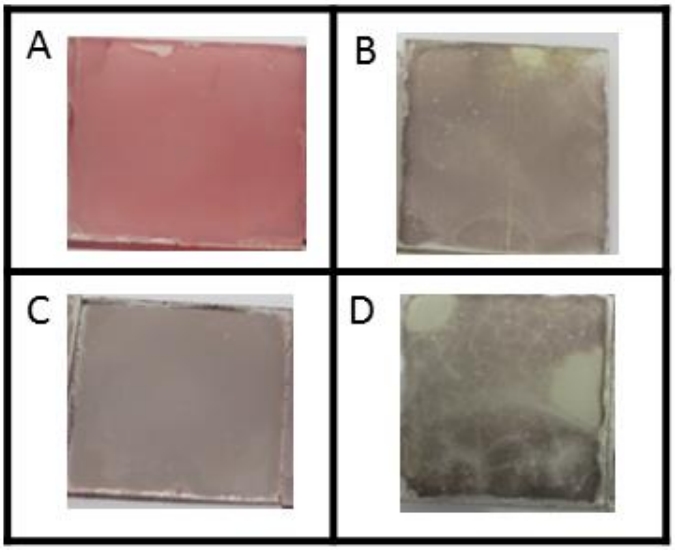

Figure 8 Depiction of films generated from solutions sets A through D. The labels in the top left-hand corner of each image correspond to the respective set.

The resulting films were then observed through SEM imaging and their elemental composition analyzed using Energy dispersive spectroscopy (EDS). Unfortunately, non-continuous films sporting distinct disconnected aggregates were formed, regardless of the solution composition. The corresponding figure on page 29 illustrates films produced based on the variations in precursor stoichiometry. Furthermore, the precursor stoichiometry between chloride and iodide was not maintained in the final product. EDS of films, tabulated on page 27 for each set, revealed that none of the groups produced films with the same chloride to halide ratio as their respective solutions. Sets A and C deviate the furthest from their respective precursor chloride to halide ratios, where chloride is virtually non-existent in the final film.

Table 2 EDS analysis of films. Note that the detection limit is ±1 atomic %.

Element	**$MAPbI_3$ Atomic %**	**Set A Atomic %**	**Set B Atomic %**	**Set C Atomic %**	**Set D Atomic %**
Pb	25	21	21	22	21
I	75	78	24	77	34
Cl	0	1.3	55	0.61	45
Cl/(I+Cl)	0	0.02	0.70	0.01	0.57

However, annealing $MAPbI_{3-x}Cl_x$ films in different atmospheres significantly improves film formation but at the expense of stability. Refer to the figure on page 31. $MAPbI_{3-x}Cl_x$ films illustrated here were synthesized from solutions of 2.64 M MAI to 0.88 M $PbCl_2$ dissolved in DMSO, spun-cast at 1000 RPM for 60 s onto FTO-coated SLG substrates and annealed in a vacuum oven that was double pump purged with

nitrogen gas before being evacuated to a pressure of 76 Torr at the temperatures and times shown in the figure on page 30. All films exhibited uniform grain size, texture, and high surface coverage but were acutely sensitive to brief drastic fluctuations in humidity. The films shown in the next figure on page 31 were exposed to relative humidity above 70% for approximately 60 seconds before housed in an argon environment maintained at less than 16% relative humidity. Evidence of that exposure manifested within 24 hours and continued until a significant portion of the film had degraded. A day later the films began to change in appearance, sporting colorless, slightly transparent regions against their original grayish hue. However, control samples kept in an inert environment retained their pristine state. Overall, adjusting the spin coating parameters, solution composition, and annealing conditions of $MAPbI_{3-x}Cl_x$ films made minimal improvements in their quality or stability.

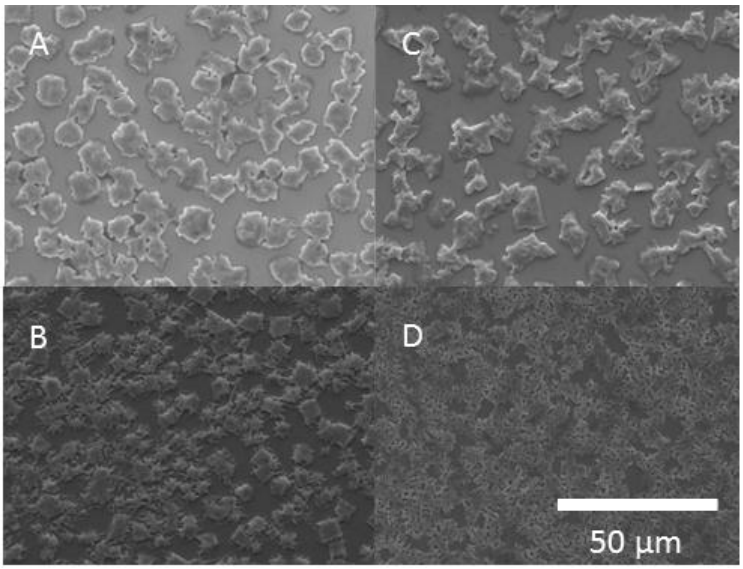

Figure 9 SEM images of $MAPbI_{3-x}Cl_x$ perovskite films generated from DMSO solutions based on the precursor compositions described in the table above. The labels in the top left-hand corner of each image correspond to the respective set.

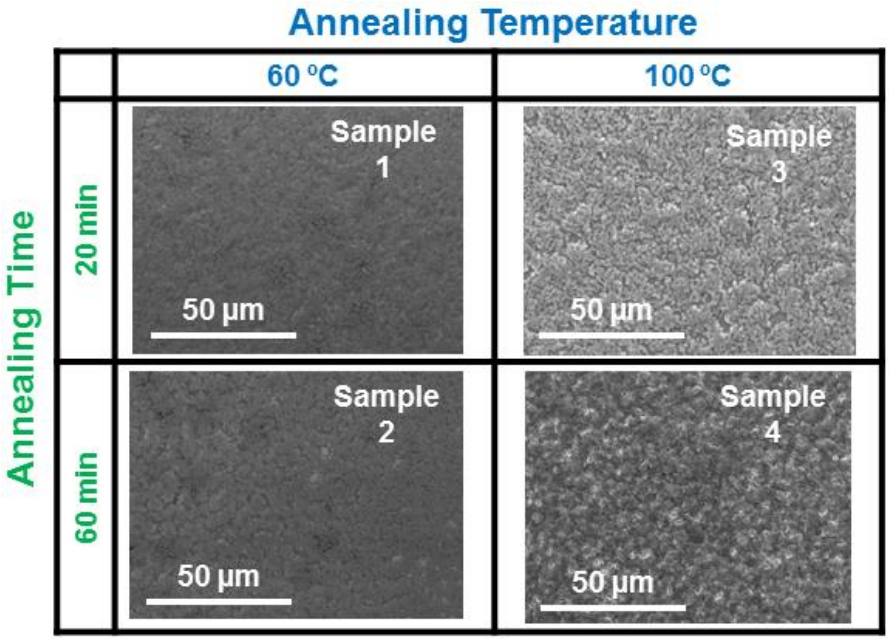

Figure 10 SEM images of $MAPbI_{3-x}Cl_x$ films annealed under a vacuum of 76 Torr.

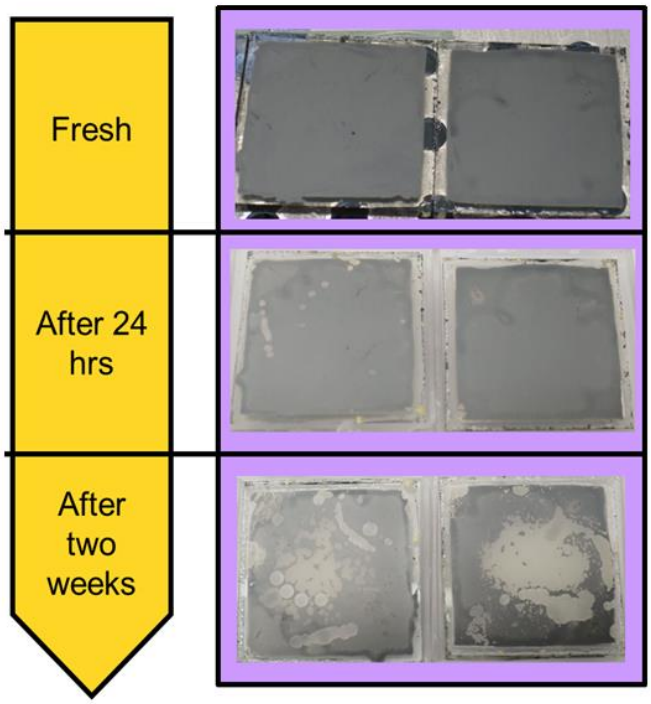

Figure 11 Aging and stability of two $MAPbI_{3-x}Cl_x$ films were annealed at 76 Torr at 100 ºC for 20 (left) and 60 (right) minutes.

Optimizing the Spin Coating Processing Variables for Depositing $MAPbI_3$ Films

Poor film formation is not solved by simply adjusting processing variables for $MAPbI_3$ films deposited through one-step spin coating either. Two replicate sets comprised of 16 $MAPbI_3$ films each were deposited onto 1" x 1" FTO-SLG substrates from a precursor solution of 2.64 M MAI and 0.88 M PbI_2 dissolved in DMSO, adjusting the following spin coating and annealing parameters in a ½ factorial screening test listen in the table on page 32. Both deposition and annealing were performed under ambient conditions.

Table 3 1/2 factorial screening test of parameters that impact the surface coverage of $MAPbI_3$ spun-cast films

Thin-film thickness parameter	Factor	Low	High
Annealing time (minutes)	A	30	90
Annealing temperature (°C)	B	90	110
Spin coating speed (rpm)	C	3000	6000
Spin coating time (seconds)	D	30	60
Amount of coating (mL)	E	0.2	0.4

Each sample was then divided into a grid as illustrated in the figure on page 33. Images of the films were taken at the sites of interest labeled 1-5 using bright field optical microscopy imaging at 400X magnification captured through a PixeLink PL-A662 Digital Camera attached to an Olympus VANOX optical microscope. The surface coverage of each image was determined using the imaging analysis software ImageJ (Yang Yu et al. 2011). The average of these five obtained values was calculated and designated as the overall surface coverage for that sample. The results are organized into a histogram on page 34. The mean coverage was 67.8 ± 3.1%, within 95% confidence, with the minimum, median, and maximum levels of coverage at 46.9%, 67.8%, and 85.7%, respectively.

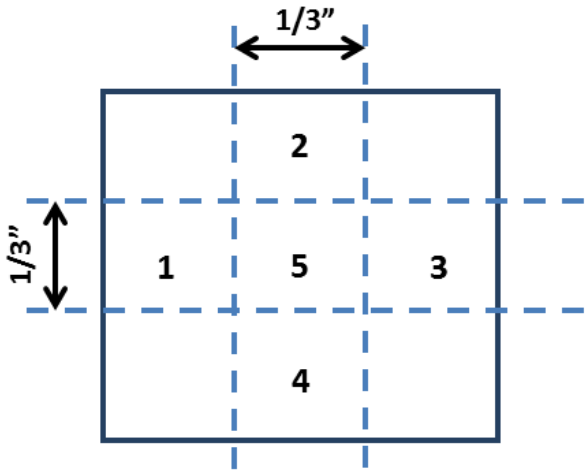

Figure 12 Grid lines and numbers were labeled on the back of each substrate in accordance to this schematic prior to image capture using optical microscopy.

Performing analysis of variance or ANOVA, with 95% confidence, generates a plot depicting the differences between the mean surface coverage of samples with respect to the high and low values of each independent variable or main effect, shown on page 35. The dashed line at the mean 67.8% is a reference point for comparing the magnitude of each main effect line. The largest changes in surface coverage correspond to the most significant factors for controlling surface coverage: spin speed, annealing temperature, and spin time. The best films, with greatest surface coverage, were generated at 3000 RPM for 30s and subsequently annealed at 110 °C. Unfortunately, the surface coverage of those optimized films only averaged 80.0 ± 9.8%, with 95% confidence. Full experimental design and ANOVA details are located in the Appendix.

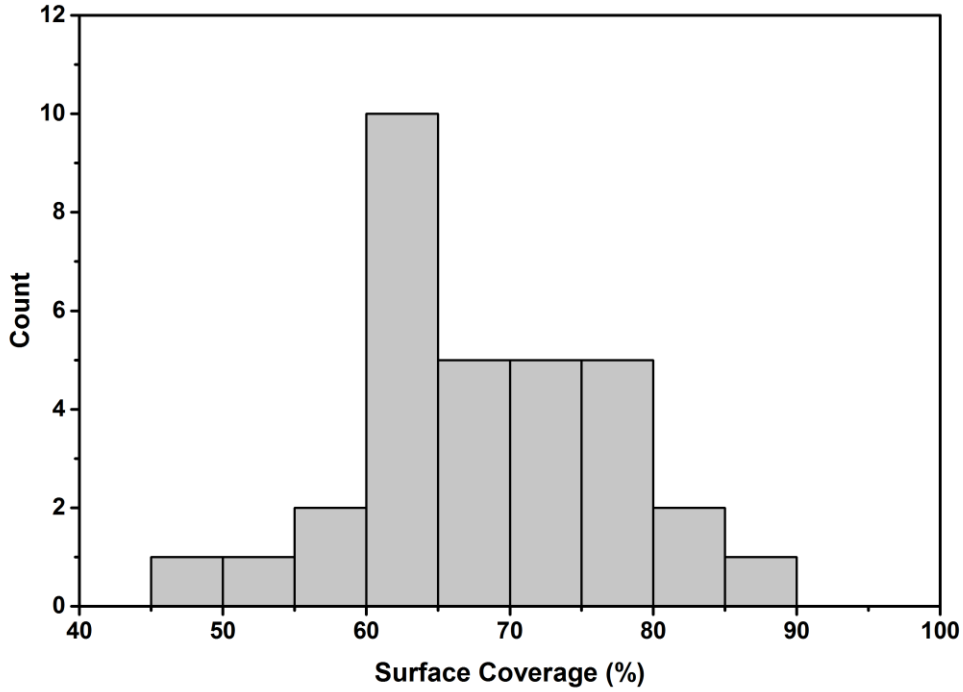

Figure 13 Histogram of surface coverage data from the 32 $MAPbI_3$ samples. More than three-fourths of the films were 60 to 80% covered.

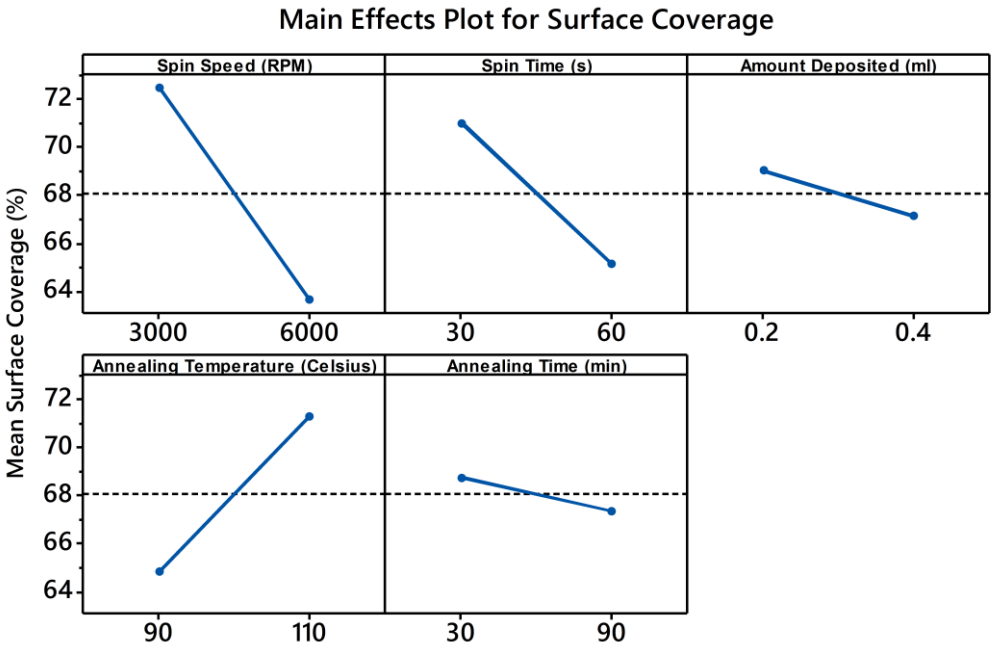

Figure 14 Main Effects Plot of surface coverage of $MAPbI_3$ films

Spin coating is a simple and easily accessible deposition technique commonly used for the deposition of OHPs, particularly the one-step spin coating processes. Unfortunately, the technique provides little control over surface coverage, morphology, film thickness, and chemical composition of films, making reproducibility and optimization of the performance of subsequently assembled PV devices a challenge. For these reasons vapor deposition has gained momentum as a favorable approach to depositing OHP films, particularly due to its commercialization potential versus that of spin coating. CSVT is especially unique in this aspect given that it is already utilized to deposit more mature thin-film PV technologies. The next chapter of this thesis will delve into the fundamentals of CSVT and is benefits compared to that of other vapor based deposition techniques.

Chapter 3

CSVT GROWTH OF $MAPbI_3$ FILMS

Introduction

CSVT, also called close-space sublimation (CSS), is a physical vapor deposition technique in which a material is sublimated onto a substrate over a distance on the order of millimeters. The technique was originally developed for depositing CdTe absorber and CdS window layers for CdTe thin-film PV devices. CdTe is one of the most mature and commercially successful thin-film PV technologies, particularly for large-scale energy projects (Schmidtke 2010). For instance, First Solar constructed the 58 MW Copper Mountain Solar 1 in Las Vegas is comprised of 1,000,000 FS 272, 275, and 277 CdTe modules (First Solar 2016a). Another example is the Avra Valley Solar project in Tuszon, AZ, a 25 MW array comprised of approximately 400,000 modules (First Solar 2016b). CSVT of CdTe and CdS layers can take place at temperatures below 300 ºC, where CdTe dissociates into Cd and Te_2 vapors when sublimated but reforms upon condensing onto the substrate. The CdTe and CdS layers are then exposed to $CdCl_2$ and O_2 at higher temperatures while in the reactor (~500 ºC) to increase the grain size and induce an inter-diffusion between the two layers that improves device performance (McCandless I.; Birkmire, R. W. 1999; Kumar and Rao 2014). CSVT growth conditions, such as deposition rate and substrate temperature, influence the optoelectronic properties of the deposited films, namely the hole carrier concentrations and mobility of minority charge carriers (McCandless I.; Birkmire, R. W. 1999).

As discussed in the previous chapter, OHP films formed using solution-based deposition are plagued with wettability issues, poor surface coverage, poor control

over reaction chemistry, non-uniform film thickness, residual solvent contamination, and the inability to scale-up into a continuous process (Liu et al. 2013; Bi et al. 2014; Eperon et al. 2014). In contrast, vapor deposition techniques, like CSVT, are able to deposit multiple layers of high purity films on a variety of substrates with nominal control over reactant stoichiometry (Ono et al. 2016). Moreover, CSVT has a number of advantages over other vapor deposition techniques that have been used to deposit OHPs. The primary advantage is the aforementioned fact that CSVT is a technique that has already been developed for commercial manufacturing of CdTe modules (Schmidtke 2010). Furthermore, CSVT allows temperature control over the source and substrate allowing for simultaneous deposition and annealing without breaking vacuum, which simplifies the fabrication process and lowers the risk of moisture intrusion. In addition, close-proximity between the substrate and source minimizes material losses due to mass transport. As a result, films can be fabricated on the order of a few minutes with minimal material consumption, maximizing the number of deposition runs before replenishing stock. Other demonstrated vapor fabrication procedures for OHP films are usually either extensively long to compensate for untargeted deposition onto the substrate or include an additional annealing step between 20 to 60 minutes (Liu et al. 2013; Gao et al. 2015; Liang et al. 2015; Jung et al. 2016). For instance, while Liang and colleagues fabricated $MAPbI_3$ perovskite films using a simultaneous vapor deposition approach is only 15 minutes, they added an additional 20 minutes for annealing for a total fabrication time of 35 minutes, not including start-up and cool-down procedures (Liang et al. 2015).

CSVT harbors the advantages of being a highly controlled deposition technique with fast fabrication times. Its degree of control translates to predictable

mass transport rates. Modeling the deposition rates of $MAPbI_3$ reactants would greatly aid in optimizing processing variables to produce thin films exhibiting complete surface coverage, smooth film texture, and comprised of large, uniform grains that result in high performing PV devices. The remainder of this chapter will be devoted to developing this model and how its accuracy will be evaluated.

Development of Fundamental Model for Deposition of OHPs by CVST

Before discussing the mass transfer mechanism in CSVT deposition, it is imperative to identify the relevant physical and thermodynamic properties of all materials involved in the deposition process that are needed to establish the model.

Physical and Thermodynamic Properties of PbI_2

Molecular Weight (M_{PbI_2}): 461.01 g/mol

Density (ρ_{PbI_2}): 6.16 g/cm^3

Melting Point (T_M) (Knacke et al. 1991): 683 K

Density at Melting Point (ρ_M) (Lide 2005): 5.691 g/cm^3

Std. Enthalpy of Sublimation (ΔH°_{sub}) (Knacke et al. 1991): 140.08 kJ/mol

Clausius-Clapeyron Equation for Vapor Pressure (P_{PbI_2}) (Knacke et al. 1991; Konings et al. 1996):

$$\ln\left(P_{PbI_2}\right) = -\frac{(2.00 \pm 0.02)E04}{T} + (31.8 \pm 0.3) \qquad 3.1$$

Where P_{PbI_2} is in Pascals and T is in degrees Kelvin.

Physical and Thermodynamic Properties of MAI

Molecular Weight (M_{MAI}): 158.97 g/mol

Density (ρ_{MAI}) (Yamamuro et al. 1986): 2.22 g/cm^3

ΔH°_{sub} (Dualeh, Gao, et al. 2014): 105±5 kJ/mol

Clausius-Clapeyron Equation for Vapor Pressure (P_{MAI}) (Dualeh, Gao, et al. 2014):

$$\ln(P_{MAI}) = -\frac{1.26E04}{T} + 24.3 \qquad 3.2$$

Where P_{MAI} is in Pa and T is in K.

Physical and Thermodynamic Properties of Argon

Molecular Weight: 39.95 g/mol

Heat Capacity (C_p) (National Institute of Standards and Technology 2016): 20.8 J/mol K

Density (ρ_{Ar}) (National Institute of Standards and Technology 2016):

$$\rho_{Ar} = -1x10^{-12}T^3 + 1x10^{-9}T^2 - 7x10^{-7}T + 2x10^{-4} \qquad 3.3$$

Where ρ is in kg/m^3 and T is in °C.

Viscosity (μ) (National Institute of Standards and Technology 2016):

$$\mu = 5x10^{-8}T + 2x10^{-5} \qquad 3.4$$

Where μ is in Pa*s and T is in °C.

Thermal Conductivity (κ) (National Institute of Standards and Technology 2016):

$$\kappa\left(\frac{W}{mK}\right) = 4x10^{-5}T + 2x10^{-2} \qquad 3.5$$

Where k is in W/m*K and T is in °C.

The maximum deposition flux based on thermodynamic limitations can be calculated using the Hertz-Langmuir relationship, originally proposed by Irving Langmuir in the early 20th century(Langmuir 1913). The relation is reproduced below.

$$J_{max} = P_{vap}\left(\frac{2\pi RT}{M_W}\right)^{-\frac{1}{2}} \qquad 3.6$$

Where J_{max} is in kg/m^{2}s, P_{vap} is in Pa, R is the universal gas constant (8.314 J/mol K), T is in K, and M_W is in kg/mol.

With the above thermodynamic data, the next step is to develop the model for predicting the deposition flux of MAI and PbI_2 in the CSVT deposition region, depicted in the figure below, using Fick's first law of molecular diffusion (Equation 3.6).

$$\overrightarrow{J_{AB}} = -D_{AB}\nabla c_A \qquad 3.7$$

Where D_{AB} is the diffusivity of the diffusing species, A, traveling through the bulk species, B and c_A is the concentration of species A.

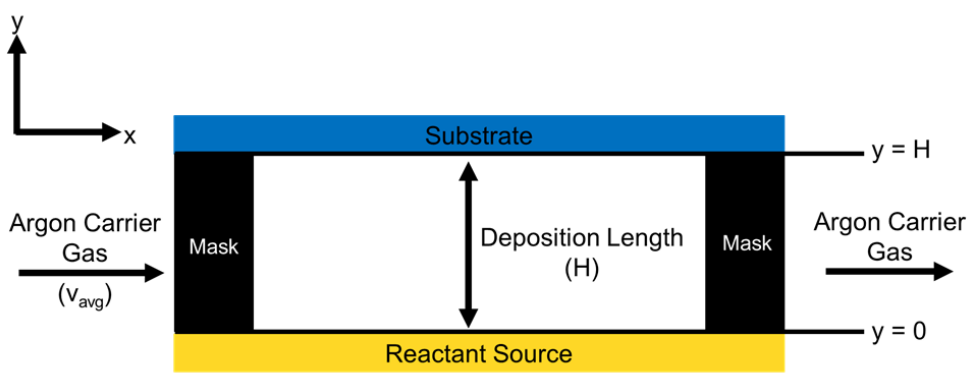

Figure 15 Schematic of the deposition region of the CSVT system, portraying the coordinate system with respect to the source.

Modifying Fick's Law of Molecular Diffusion for CSVT

Fick's law can be modified to accommodate modeling deposition region by applying the following assumptions:

1. The deposition length corresponds to the sum of the depth of the source well, the thickness of the deposition masks and spacers.
2. Deposition is isolated to control volume.
3. Since the deposition of the reactants is sequential, no reactions are occurring between the carrier gas and each reactant.
4. Overall argon carrier gas trajectory is in the x-direction.
5. Both the carrier and sublimated reactants behave like an ideal gas.
6. No re-sublimation of reactant once it deposits onto the substrate.
7. Heat transfer between the source and substrate occurs through conduction only.
8. Pressure inside and outside of deposition region are in equilibrium.
9. Deposition flux is at steady-state and only occurs in the y-direction since the x-dimension is infinitely long with respect to H.
10. Temperature and vapor pressure gradients between the source and substrate are constant.

Assumptions 4 and 9 aid in establishing the boundary conditions, which have been added to the schematic of the deposition region shown on page 40 and reproduced below.

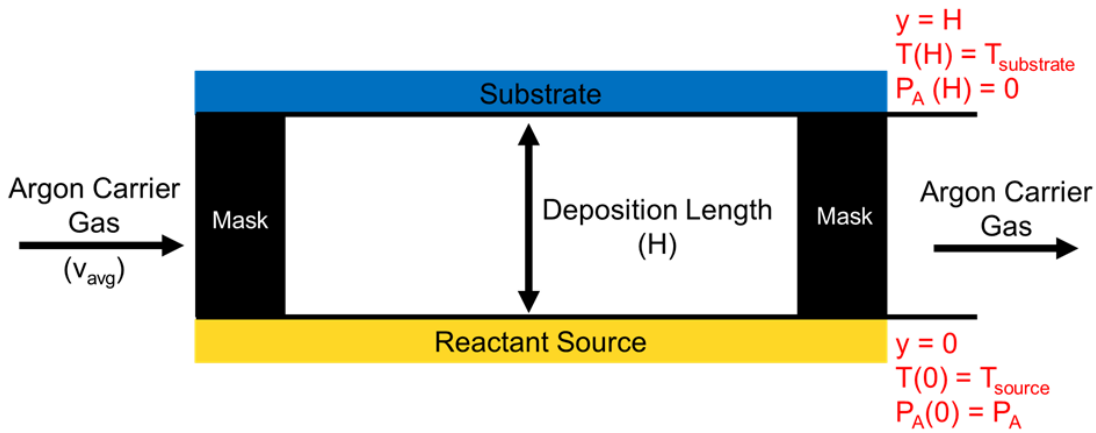

Figure 16 Reproduction of the deposition region with boundary conditions, highlighted in red, fashioned from the model's assumptions.

The addition of assumptions 5 and 7 restrict Fick's law to its one-dimensional form, equation 3.8.

$$J_{AB} = -D_{AB}\left(\frac{dc_A}{dy}\right) \qquad 3.8$$

Where the concentration of diffusing species A is calculated using the ideal gas law, where P_A is the partial pressure of species A.

$$P_A V = n_A RT \rightarrow \frac{n_A}{V} = c_A = \frac{P_A}{RT} \qquad 3.9$$

The concentration gradient is then expanded in equation 3.10 to include a temperature and pressure gradient for species A.

$$-\frac{dc_A}{dy} = -\frac{\partial c_A}{\partial P_A}\left(\frac{dP_A}{dy}\right) - \frac{\partial c_A}{\partial T}\left(\frac{dT}{dy}\right) = \frac{1}{RT}\left(\frac{dP_A}{dy}\right) + \frac{P_A}{RT^2}\left(\frac{dT}{dy}\right) \qquad 3.10$$

As a result, equation 3.7 also expands into the relationship depicted in equation 3.11.

$$J_{AB} = -\frac{D_{AB}}{RT(0)}\left(\frac{dP_A}{dy}\right) + \frac{D_{AB}P_A}{R[T(0)]^2}\left(\frac{dT}{dy}\right) \qquad 3.11$$

Where the vapor pressure gradient, $(dP_A)/dy$, and dT/dy are simplified to equations 3.12 and 3.13, respectively, based on assumption 10.

$$\frac{dT}{dy} = \frac{\Delta T}{\Delta y} = \frac{T_{source} - T_{substrate}}{H} \qquad 3.12$$

$$\frac{dP_A}{dy} = \frac{\Delta P_A}{\Delta y} = \frac{P_A(H) - P_A(0)}{H} = -\frac{P_A(0)}{H} \qquad 3.13$$

Therefore, the modified form of Fick's law for modeling CSVT is depicted below.

$$\boldsymbol{J_{AB} = -\frac{D_{AB}}{RT(0)}\left(\frac{P_A(0)}{H}\right) + \frac{D_{AB}P_A(0)}{R[T(0)]^2}\left(\frac{T_{source} - T_{substrate}}{H}\right)} \qquad \mathbf{3.14}$$

The deposition flux is a function of five processing variables: T_{source} , P_A, their respective temperature and pressure gradients, and H. The diffusivity, D_{AB}, changes based on the selected T_{source} and sum of the system and vapor pressures, P_{total}.

Calculating Diffusivity of MAI and PbI_2

One of the most critical aspects of accurately modeling the deposition flux of each reactant is the calculation of D_{AB}, which in this case is the diffusivity of sublimated MAI or PbI_2 through the bulk argon gas. Unfortunately, published data is unavailable for these two binary systems. Therefore, D_{AB} must be either determined theoretically or empirically. There are two widely accepted approaches for calculating D_{AB} for an unknown binary-systems: the Chapman-Enskog model and the Fuller, Schettler, and Giddings method.

The Chapman-Enskog (CE) model, was originally derived by Sidney Chapman and David Enskog in the early 1900s for monatomic non-polar binary gas systems by solving the Boltzmann equation, assuming that the intermolecular forces between the molecules can be represented by the Lennard-Jones function (Geankoplis 2003).

However, the CE model is applicable to polyatomic non-polar gases and can be modified to accommodate polar and polar/non-polar gas systems. (Poling et al. 2000; Bird et al. 2002). Fortunately, all substances involved in the deposition process are non-polar. Equation 3.14, depicts the CE model.

$$D_{AB} = 0.0018583\sqrt{T^3\left(\frac{1}{M_A}+\frac{1}{M_B}\right)}\left(\frac{1}{P\sigma_{AB}^2\Omega_{D_{AB}}}\right) \qquad 3.15$$

Where M_A and M_B are the molecular weight of species A and B, respectively in g/mol, P is the total pressure in atm, T is in K, and the resulting D_{AB} is in cm^2/s. σ_{AB}^2 is collision diameter or the characteristic length of the intramolecular force described by the Lennard-Jones function for the molecular pair AB, measured in Å. The term $\Omega_{D_{AB}}$ is the collision integral for diffusion, a ratio noting the deviation between the interactions between the actual gas molecules versus if they were rigid, non-interacting spheres. $\Omega_{D_{AB}}$ is a dimensionless term that is a function of dimensionless temperature, kT/ε_{AB} or T*, where ε_{AB} is the characteristic energy or the maximum attractive energy of the AB molecular pair and k is the Boltzmann constant. Neufeld, Jansen, and Aziz generated a regression equation (equation 3.15) for $\Omega_{D_{AB}}$ as a function of T* that is applicable when applying Lennard-Jones function to the CE model (Bird et al. 2002; Geankoplis 2003).

$$\Omega_{AB} = \frac{1.06036}{T^{*0.15610}} + \frac{0.193}{e^{0.47635T^*}} + \frac{1.035887}{e^{1.52996T^*}} + \frac{1.76474}{e^{3.89411T^*}} \qquad 3.16$$

$\Omega_{D_{AB}}$, σ_{AB}^2, and kT/ε_{AB} must be calculated using the individual σ and ε/k values of the carrier gas and sublimated reactants. For argon, σ and ε/k are 3.504 Å and 117.7 K, respectively (Sandler 2010). Unfortunately, at the time of writing this dissertation, σ and ε/k can only be estimated for PbI_2. Therefore, the CE model will be

used to evaluate the D_{AB} of PbI_2 in argon only. Joseph O. Hirschfelder and Charles F. Curtiss derived empirical relations for estimating σ and ε/k using either the critical point, melting point, or normal boiling point and corresponding specific volume of the material (Bird et al. 2002). Equations 3.16 and 3.17 are the relations for estimating σ and ε/k at the melting point of PbI_2, respectively.

$$\frac{\varepsilon}{k} = 1.92\, T_M \qquad 3.17$$

Where T_M in K.

$$\sigma = 1.222\, \bar{V}_M^{1/3} \qquad 3.18$$

$\bar{V}_M$ is the molar specific volume at the melting point in cm^3/mol and can be easily calculated from ρ_M and M_{PbI_2} (Lide 2005).

$$\bar{V}_M = \frac{M_{PbI_2}}{\rho_M} \qquad 3.19$$

The resulting estimates for ε/k and σ_A for PbI_2 are 1310 K and 5.287 Å, respectively. For non-polar molecular pairs, σ_{AB} is then calculated to be 4.396 Å and ε_{AB}/k is 392.7 K using combining rules in equations 3.19 and 3.20, respectively.

$$\sigma_{AB} = \frac{1}{2}(\sigma_A + \sigma_B) \qquad 3.20$$

$$\frac{\varepsilon_{AB}}{k} = \sqrt{\frac{\varepsilon_A}{k}\left(\frac{\varepsilon_B}{k}\right)} \qquad 3.21$$

Unfortunately, the CE model is relatively complex, and in the case of MAI, estimating the necessary parameters is difficult. Fuller, Schettler, and Giddings developed a semi-empirical correlation of D_{AB} to temperature and pressure. The Fuller, Schettler, and Giddings (FSG) method is less accurate than its more theoretical counterpart but is equally as versatile for calculating D_{AB} for both nonpolar and polar-

nonpolar gas systems (Poling et al. 2000; Geankoplis 2003). The relationship, as presented by Fuller, is reproduced below (Fuller et al. 1969).

$$D_{AB} = \frac{1.00x10^{-3}T^{1.75}\left(\frac{1}{M_A}+\frac{1}{M_B}\right)^{\frac{1}{2}}}{P\left[(\sum \upsilon_A)^{\frac{1}{3}}+(\sum \upsilon_B)^{\frac{1}{3}}\right]^2} \qquad 3.22$$

Where computed value for D_{AB} is in m^2/s, M_A and M_B are in g/mol, T is in K, and P in atm. Values υ_A and υ_B are the diffusion volume increments for substances A and B, respectively, in cm^3, listed for a number of compounds by the Fuller, *et al* (Fuller et al. 1966; Fuller et al. 1969). Unfortunately, this tabulation is limited to a select number of substances that are commonly studied in their gaseous state, such as Xe and He. So equation 3.21 is only applicable to MAI, where $\sum \upsilon_A$ and $\sum \upsilon_B$ are 64.1 and 16.2 cm^3 for MAI and argon, respectively. But, from this relationship a simple proportionality arises that is applicable to both reactants:

$$D_{AB} \propto \frac{T^{1.75}}{P} \qquad 3.23$$

Hence, if the diffusivity is known at one temperature and pressure, the value can be extrapolated to a different pair of conditions using equation 3.23.

$$D_{AB,2} = D_{AB,1}\frac{P_1}{P_2}\left(\frac{T_2}{T_1}\right)^{1.75} \qquad 3.24$$

Assessment of the Deposition Model for PbI_2 and MAI Vapors

Both aforementioned approaches were used to calculate the diffusivity of sublimated MAI and PbI_2 vapors in argon, the CE model was applied to PbI_2 and the FSG approach to MAI. From there a number of CSVT deposition case studies were

conducted exploring different combinations of processing variables with the measured deposition flux. This data was used to evaluate how accurate the diffusivity models were at predicting the deposition flux of each reactant under the same processing conditions. A properly developed model will be an essential aid in when conducting optimization studies to locate CSVT processing conditions that form optimal $MAPbI_3$ films for PV devices. The next chapter will introduce the operation of the CSVT system and the experimental design of the deposition case studies. The results will be compared with the corresponding calculated values.

Chapter 4

EVALUATING THE MASS TRANSORT MODEL FOR DEPOSITION OF $MAPbI_3$ USING CSVT

The high degree of control in depositing OHP films using CSVT can be demonstrated by developing a computational model to predict deposition flux of each reactant. The accuracy of this mass transport model, originally introduced in Chapter 3, was assessed through the deposition the $MAPbI_3$ reactants MAI and PbI_2. Information on the design of the system used in this investigation and general experimental procedure for each deposition run are discussed below.

CSVT System Layout and Components

An overall schematic of the CSVT system used in this investigation is located on page 50 accompanied with an image of the assembled system on page 51. A more detailed illustration of the deposition zone on page 52 highlights the main components of the system: 1) two graphite susceptors used to independently heat the source and substrate for greater control over the mass transport of the sublimating material and properties of the fabricated film, 2) mica masks that establish the deposition area and 3) mica spacers to set the deposition height and thermally isolate the two regimes, establishing the thermal driving force that directs the sublimed material. The entire deposition apparatus is suspended on a glass holder and encapsulated in a 5.3 cm diameter quartz tube that is 45.7 cm long, with 5.1 cm and 3.8 cm diameter inlet and outlet custom-sized rounded ends that connect to the inert gas feed and vacuum outlet fixtures. The substrate and source susceptors are heated using 650 W General Electric Quartzline® lamps set in fixtures that are positioned above and below the deposition region, respectively. The lamps are controlled by two Eurotherm® 2404 temperature

controllers, equipped with Omega® KMQSS-020U-12 K type thermocouples that are threaded from the vacuum outlet side into the system and embedded into wells drilled in each susceptor. To prevent overheating, a water coolant loop passes through each lamp into a retention bath kept at ambient temperature. Pressure is maintained through a dynamic vacuum system and measured using a Hastings VT-6 thermocouple vacuum gauge with analog display and DV-6 gauge tube. The flow of inert gas supplied from a compressed gas cylinder is controlled using a MKS 247D four-channel readout with a 1000 SCCM range mass flow controller (MFC) (model # 1179A13CR1BV-S). The MFC was calibrated with argon gas. Under constant flow, the desired pressure within the quartz tube is set by adjusting the orifice valve leading to an IVS 6XJ20BB roughing vacuum pump. A tinted shield is erected during deposition to protect the operator's vision when operating the system due to the high intensity of the illuminated bulbs. Based on these features, the relevant variables that govern deposition flux in the system are the source temperature, substrate temperature, deposition height, deposition time, deposition area, and system pressure.

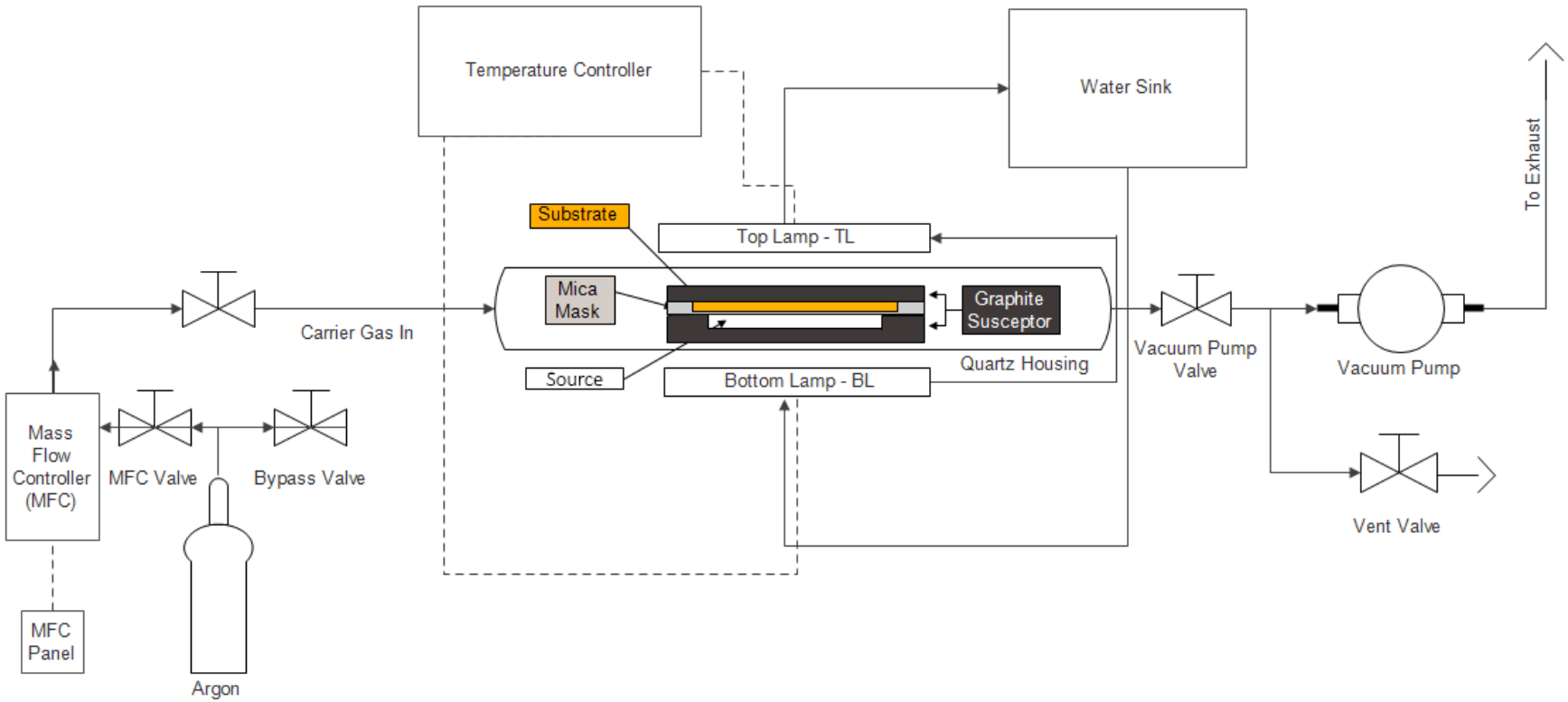

Figure 17 Schematic of CSVT deposition system utilized to deposit OHP films.

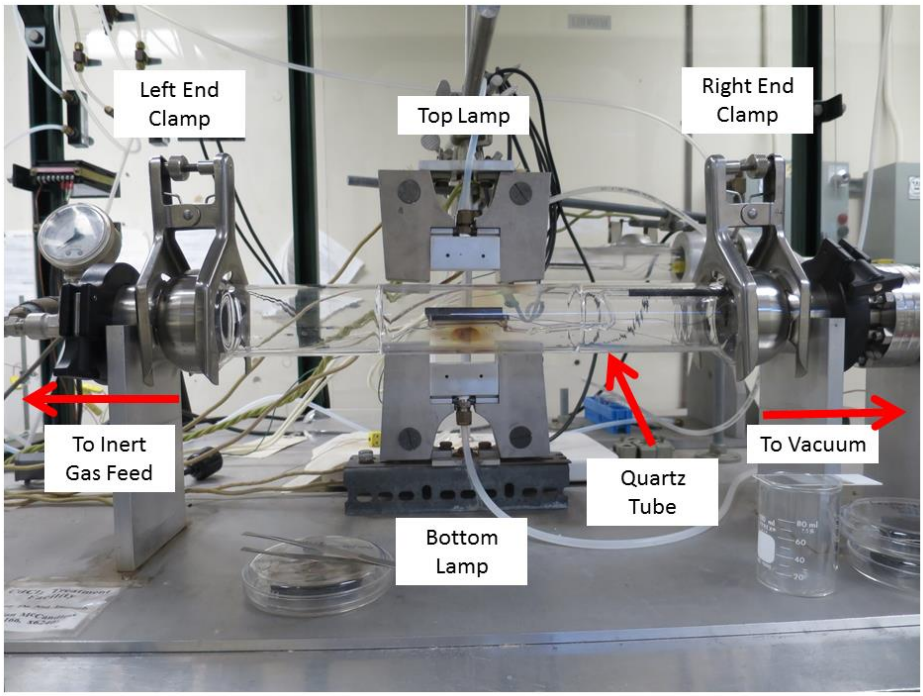

Figure 18 Photo depicting major components of the CSVT system used in this investigation. The details of the deposition region in between the susceptors, located at the center of the image, are presented in more detail in the following figure on page 52.

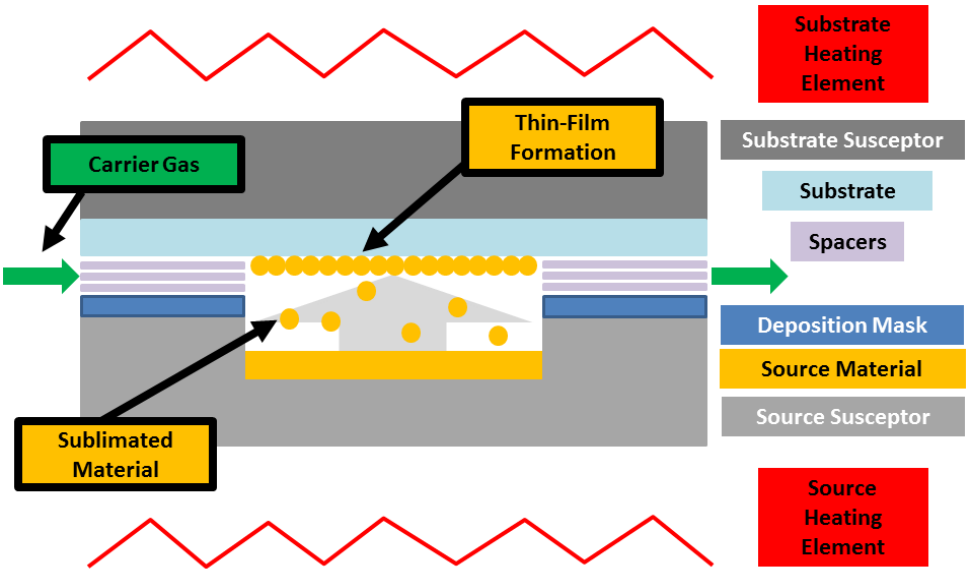

Figure 19 Cross-sectional schematic of a CSVT deposition region. Dashed lines correspond to open region of deposition mask.

Sample Preparation and Standard Operating Procedure

The SLG substrates were scrubbed with a glass-cleaning brush and a solution comprised of 1 g of sodium tripolyphosphate detergent from Sigma Aldrich and 1 g Triton X-100 surfactant (Sigma) dissolved in 100 mL of 18.2 MΩ-cm NanoPure water and subsequently rinsed in NanoPure water. Substrates were then dried and stored in an exclusive desiccator cabinet for later.

PbI_2 was supplied by Sigma Aldrich and MAI was synthesized based on a commonly published procedure (Eperon et al. 2014). First, 19 mL of a 33 wt % solution of methylamine in ethanol (Sigma) was deposited into a flask under constant argon flow. Next, 20 mL of a 57 wt % aqueous solution of HI was introduced in a drop wise fashion using a Pasteur pipet. Afterwards, the solution was stirred for approximately two hours before heating between 100 and 110°C for one to three hours until the first sign of MAI precipitation is noted. At that point the container harboring

the solution was immediately removed from the heat source and allowed to cool to room temperature in a secluded location overnight.

Purification of the synthesized MAI is critical since the product is contaminated with unreacted HI, methylamine solution, water, and ethanol. The product was recrystallized using a minimal amount of ethanol (ThermoFisher Scientific). After 24 hours, the material is then vacuum filtered through a fitted glass or ceramic Buchner funnel and washed with diethyl ether (Sigma)**.** Upon introducing diethyl ether, the solubility of any residual product in the distillate decreases, forcing it out of solution. Thus, a second pass of the distillate was performed to recover as much of this material as possible. After completely drying the material, the recrystallization and filtration steps were conducted two more times before the material was used. Powder XRD confirmed the synthesis of the product seen in the figure on page 54

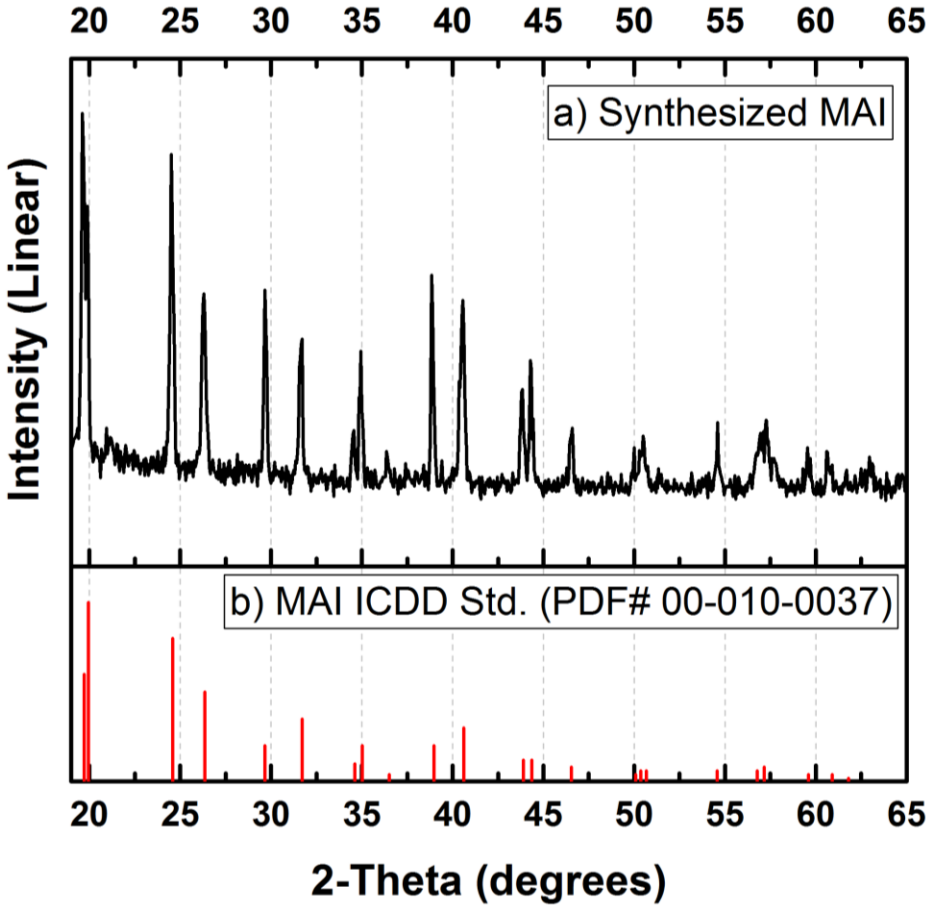

Figure 20 Powder XRD pattern of a) synthesized MAI compared to b)powder diffraction file (PDF) 00-010-0037 obtained from the International Centre for Diffraction Data (ICDD, 2013).

A source and substrate susceptor was assigned to each reactant. PbI_2 and MAI were finely ground using a mortar and pestle and then tightly packed into the susceptor well using a piece of SLG cut to the same size as the area of the well. New sources were sintered to ensure a uniform surface for deposition. Another SLG piece was placed, securing the well-fitted glass in place and minimize unwanted sublimation of the source while sintering, followed by the substrate susceptor. The susceptor

apparatus was then loaded into the system. MAI sources were sintered at 150 °C and PbI_2 sources at 375 °C for fifteen minutes at ambient pressure.

Prior to the start of any run, the temperature controllers were set to their desired set points and the corresponding temperature recording software was initiated. This was followed by a single system pump purge to remove moist contaminated ambient air. Under the constant flow of inert gas, the vacuum orifice was then adjusted until the desired system pressure is observed. After the pressure stabilized, the UV shield was erected and the source temperature controller activated. The deposition time began when the source temperature reached the set point. Once the process began, the pressure, source temperature, and substrate temperature were documented by the operator at 1 minute intervals onto a deposition run sheet that documented observations and results. Source and substrate temperature were also recorded over the entire course of the run by the monitoring program. Upon completion, the temperature recording software was stopped, controller was shut off, and the vacuum orifice was closed. The inert gas flow rate was then gradually increased to maximum rate to purge the system back to ambient pressure and stop the deposition process. The amount of material deposited onto the cleaned substrates was determined from the average of three measurements taken before and after deposition using a Mettler Toledo AT261 DeltaRange® scale with a sensitivity limit of 1-0.1 mg.

In between blocks of replicate runs, and before switching sources, the quartz tubing and glass susceptor holder were cleaned with a dilute solution of Alconox Liquinox® detergent in DI water and a glass-cleaning brush.

Modeling Deposition Flux of $MAPbI_3$ Reactants

PbI_2 Deposition

The PbI_2 deposition case study was conducted using a full-factorial experimental design comprised of three factors, including one hard-to-change (HTC) factor, listed in the table below. Pressure was designated as the HTC factor not because it was difficult to adjust but because the proportional-integral-derivative (PID) tuning parameters of the temperature controllers were dependent on both temperature and pressure. During the development of the experiments, slight adjustments to either parameters without retuning resulted in unstable temperature profiles. Thus, the controllers were tuned to one set of PID parameters at 0.6 Torr and another at 1.0 Torr to ensure that the temperature profile behavior remained the same. The substrate temperature was not controlled. The deposition time was held at five minutes to primarily demonstrate how quickly films could be produced. The rate of mass change in the source and the plain SLG substrate were documented. Due to limited materials for producing different sized masks, the deposition area was held constant at 4 cm^2. The argon carrier gas flow rate was set to 70 SCCM. The experiment contained two replicates, separated into two blocks for a total of 16 runs. As a result, the experiment is of a Resolution III design. Despite the existence of confounded effects other than that of the main factors, the purpose of employing this design was not to determine the most significant factors that impact deposition flux since all processing variables are either directly or indirectly included in the model. Ignoring one of those factors may compromise the model's accuracy. The full factorial design in this case allows for efficient use of time and resources to explore the impact of multiple processing variables on deposition flux.

Table 4 Deposition variables explored in the PbI_2 deposition case study (* = HTC Factor)

Deposition Variable	Factor	Low	High
P_{sys} (Torr)*	A	0.6	1.0
T_{source} (°C)	B	375	385
H (mm)	C	2.83	3.83

The empirical deposition flux was calculated by dividing the rate of mass loss from the source by the deposition area. The arithmetic mean and corresponding standard deviation for each experimental condition is summarized in the table below. Where, P_{sys} is system pressure, H is deposition height, T_{source} is the temperature of the source material, $T_{substrate}$ is the temperature of the substrate, Δm_{source} is the change in the mass of the source, and J_{AB} is the deposition flux. Note that the deposition flux is assumed to be steady state so the negative sign corresponds to the fact that the deposition flux was calculated with respect to the source. Full tabulation of the results is available in Appendix A.

Table 5 Summary of Results for PbI_2 Deposition Case Study

P_{sys} (Torr)	H (mm)	T_{source} (°C)	$T_{substrate}$ (°C)	Δm_{source} (g)	J_{AB} (g/cm^{2}s)
0.6	2.83	375	104.4	-(1.2±0.5)E-02	-(9.8±4.5)E-06
0.6	2.83	385	109.0	-(2.8±0.7)E-02	-(2.4±0.6)E-05
0.6	3.83	375	98.0	-(1.6±0.5)E-02	-(1.3±0.4)E-05
0.6	3.83	385	99.5	-(1.7±0.5)E-02	-(1.4±0.4)E-05
1.0	2.83	375	115.3	-(7.9±3.6)E-03	-(6.5±3.0)E-06
1.0	2.83	385	119.8	-1.0E-02	-(8.5±0.2)E-06
1.0	3.83	375	102.5	-(2.9±0.6)E-03	-(2.4±0.5)E-06
1.0	3.83	385	103.8	-(5.7±2.6)E-03	-(4.7±2.2)E-06

In comparison, the CE model estimates for the diffusivity and deposition flux are listed in the table below.

Table 6 Comparison of Empirical (EMP) and Calculated (CE) Deposition Flux for PbI_2

P_{sys} (Torr)	H (mm)	T_{source} (°C)	$T_{substrate}$ (°C)	Δm_{source} (g)	$J_{AB\text{-}EMP}$ (g/cm^{2}s)	$D_{AB\text{-}CE}$ (cm^2/s)	$J_{AB\text{-}CE}$ (g/cm^{2}s)
0.6	2.83	375	104.4	-(1.2±0.5)E-02	-(9.8±4.5)E-06	280.4	-3.3E-04
0.6	2.83	385	109.0	-(2.8±0.7)E-02	-(2.4±0.6)E-05	282.7	-5.2E-04
0.6	3.83	375	98.0	-(1.6±0.5)E-02	-(1.3±0.4)E-05	280.4	-2.7E-04
0.6	3.83	385	99.5	-(1.7±0.5)E-02	-(1.4±0.4)E-05	282.7	-4.2E-04
1.0	2.83	375	115.3	-(7.9±3.6)E-03	-(6.5±3.0)E-06	170.6	-2.0E-04
1.0	2.83	385	119.8	-1.0E-02	-(8.5±0.2)E-06	173.5	-3.2E-04
1.0	3.83	375	102.5	-(2.9±0.6)E-03	-(2.4±0.5)E-06	170.6	-1.6E-04
1.0	3.83	385	103.8	-(5.7±2.6)E-03	-(4.7±2.2)E-06	173.5	-2.6E-04

The model successfully accounted for the direct correlation between deposition flux and temperature while H and P_{sys} were held constant. However, the estimated values are at least an order of magnitude higher than the actual flux. Reasons for this discrepancy are discussed below.

MAI Deposition

The experimental design for the MAI deposition case study was a simpler two-way classification design, focusing on only adjusting the system pressure and source temperature, the explored parameters tabulated below. The experiment was comprised of two replicates, separated into two blocks for a total of 12 runs. Pressure was not an HTC factor in this case since the challenges with PID tuning that were faced during the PbI_2 case study were resolved by decreasing the power output from the lamps to

25% their maximum output. This approach minimized the likelihood of overshoot upon startup and fluctuations about the set point. The variable H was not adjusted in these studies due to the fact that MAI is much more volatile than its lead counterpart, resulting in poorer control over its trajectory even at such close proximity between the source and substrate. The amount of material that resides within the deposition region is inversely related to H. Therefore, it is best to keep H as low as possible to retain the maximum amount of material while providing enough clearance for the deposition region to reach equilibrium with its surroundings. In this case, the deposition height has held constant at 2.33 mm along with the deposition time at five minutes and deposition area at 4 cm^2. Again, the argon carrier gas flow rate was set to 70 SCCM. The empirical deposition flux was also calculated based on the rate of mass loss from the source. A summary of the results is tabulated below with the details of the individual runs stored in Appendix A.

Table 7 Deposition variables explored in the MAI deposition case study

Deposition Factor	Values
P_{sys} (Torr)	0.6, 1.0
T_{source} (°C)	155, 165, 175

Table 8 Summary of Results for MAI Deposition Case Study

P_{sys} (Torr)	T_{source} (°C)	$T_{substrate}$ (°C)	Δm_{source} (g)	J_{AB} (g/cm2s)
0.6	155	42.3	-(4.6±0.6)E-03	-(3.8±0.5)E-06
0.6	165	43.3	-(6.2±2.3)E-03	-(5.1±1.9)E-06

0.6	175	44.1	-(8.1±0.6)E-03	-(6.8±0.5)E-06
1.0	155	45.4	-(3.8±1.3)E-03	-(3.2±1.1)E-06
1.0	165	48.5	-(4.0±0.4)E-03	-(3.3±0.3)E-06
1.0	175	50.9	-(6.2±1.9)E-03	-(5.1±1.6)E-06

In comparison, the FSG method estimates for the diffusivity and corresponding deposition flux are listed in the table on page 60.

Table 9 Comparison of empirical (EMP) and calculated deposition flux (FSG) for MAI

P_{sys} (Torr)	T_{source} (°C)	$T_{substrate}$ (°C)	Δm_{Source} (g)	$J_{AB\text{-}EMP}$ (g/cm^{2}s)	$D_{AB\text{-}FSG}$ (cm^2/s)	$J_{AB\text{-}FSG}$ (g/cm^{2}s)
0.6	155	42.3	-(4.6±0.6)E-03	-(3.8±0.5)E-06	8.0	-1.1E-03
0.6	165	43.3	-(6.2±2.3)E-03	-(5.1±1.9)E-06	4.6	-1.2E-03
0.6	175	44.1	-(8.1±0.6)E-03	-(6.8±0.5)E-06	2.6	-1.2E-03
1.0	155	45.4	-(3.8±1.3)E-03	-(3.2±1.1)E-06	7.5	-1.0E-03
1.0	165	48.5	-(4.0±0.4)E-03	-(3.3±0.3)E-06	4.3	-1.1E-03
1.0	175	50.9	-(6.2±1.9)E-03	-(5.1±1.6)E-06	2.5	-1.2E-03

Unlike with PbI_2, the model estimates a majority of deposition flux values within the same order of magnitude as the measured quantities. However, a negative correlation between of the calculated D_{AB} to temperature was observed at both system pressures. Furthermore, the change in the calculated J_{AB} is virtually stagnant while the empirical values clearly display a direct relation with temperature under isobaric conditions.

Discussion on Accuracy of Deposition Flux Model

In both instances the model exhibits inaccuracies, overestimating the deposition flux of PbI_2 by at least an order of magnitude and incorrectly depicting the relationship between the mass transfer of MAI and temperature. The main causes of these inaccuracies may stem from the assumptions used to develop the model, the methods used to estimate the diffusivity of each reactant in the bulk phase, or various systematic errors.

Validating Model Assumptions

One of the most critical model assumptions, originally introduced in chapter 3, is that the only means of heat transfer between the source and substrate occurs through conduction. Otherwise, the form of Fick's law that was used to develop equation 3.13 would have to be modified to accommodate the addition of convective mass transfer. Recall that there are two general forms of heat transfer: convection and conduction. Conduction is the transfer of heat through random interactions between molecules or atoms that make up a substance. Hence, the primary means of heat transfer through solids. In contrast, convection occurs through both the transfer of heat through diffusion and the resulting bulk transport of material, a phenomenon normally associated with fluids. Convection can further be classified as forced or natural convection. Forced convection is the transfer of heat through the motion of a fluid directed by an external force, such as a pump or fan. Natural convection is the transfer of heat through differences in buoyancy due to the presence of a temperature gradient (Geankoplis 2003). If convection exists within the deposition region, it would most likely be natural since a temperature differential is maintained between two locales would induce bulk movement of the argon carrier gas, enhancing the deposition flux.

The Peclet and Rayleigh numbers can be calculated for the argon gas, ignoring the concentration of the sublimed reactant, in order to determine if mass transfer is governed by conduction. The Péclet (Pé) number is a ratio of heat transfer originating from convection versus that of conduction calculated from the product of the Reynolds (Re) and Prandtl (Pr) numbers. If the Pé is less than 1, the system is governed primarily by conduction. Otherwise, the dominant heat transfer mechanism is convection. In addition, the onset of natural convection can be determined by calculating the Rayleigh (Ra) number, a dimensionless value named after John William Strutt or Lord Rayleigh. Ra is the product of the Grashof (Gr) and Pr dimensionless numbers. By principle natural convection does not manifest as long as Ra is less than the critical value, which in this case is 1708. Beyond this value, the deposition region would behave like a Poiseuille-Bénard system, featuring Poiseuille flow through a rectangular channel maintaining a temperature gradient between the top and bottom locales. Temperature differential within this arrangement can induce Rayleigh-Bénard convection, where the carrier gas is heated from below by the higher temperature source inducing the convective forces (Nicolas et al. 1997). The relationships for calculating both dimensionless numbers are shown in equations 4.1and 4.2 (Bird et al. 2002; Hauke 2008).

$$Pé = Re\ Pr = \frac{\rho c_P \upsilon H}{\kappa} \qquad 4.1$$

$$Ra = Gr\ Pr = \frac{H^3 \rho^2 g \beta (T_{Source} - T_{substrate}) c_P}{\mu \kappa} \qquad 4.2$$

Where g is the acceleration of gravity (9.81 m/s^2), β is the volumetric coefficient of expansion calculated from the inverse of the average of T_{source} and $T_{substrate}$ in K.

$$\beta = \left[\frac{(T_{source} + T_{substrate})}{2}\right]^{-1} \qquad 4.3$$

Pé and Ra values were calculated at the minimum and maximum operating pressures, 1.0E-3 and 760 Torr, respectively, from 100 to 400 ºC to determine if there is a pressure-temperature combination that would generate convective forces, namely natural convection. These Pé trends calculated for argon at temperature differences between 50 to 200 °C is plotted below show that the primary heat transfer mechanism throughout the entire operating pressure range is conduction.

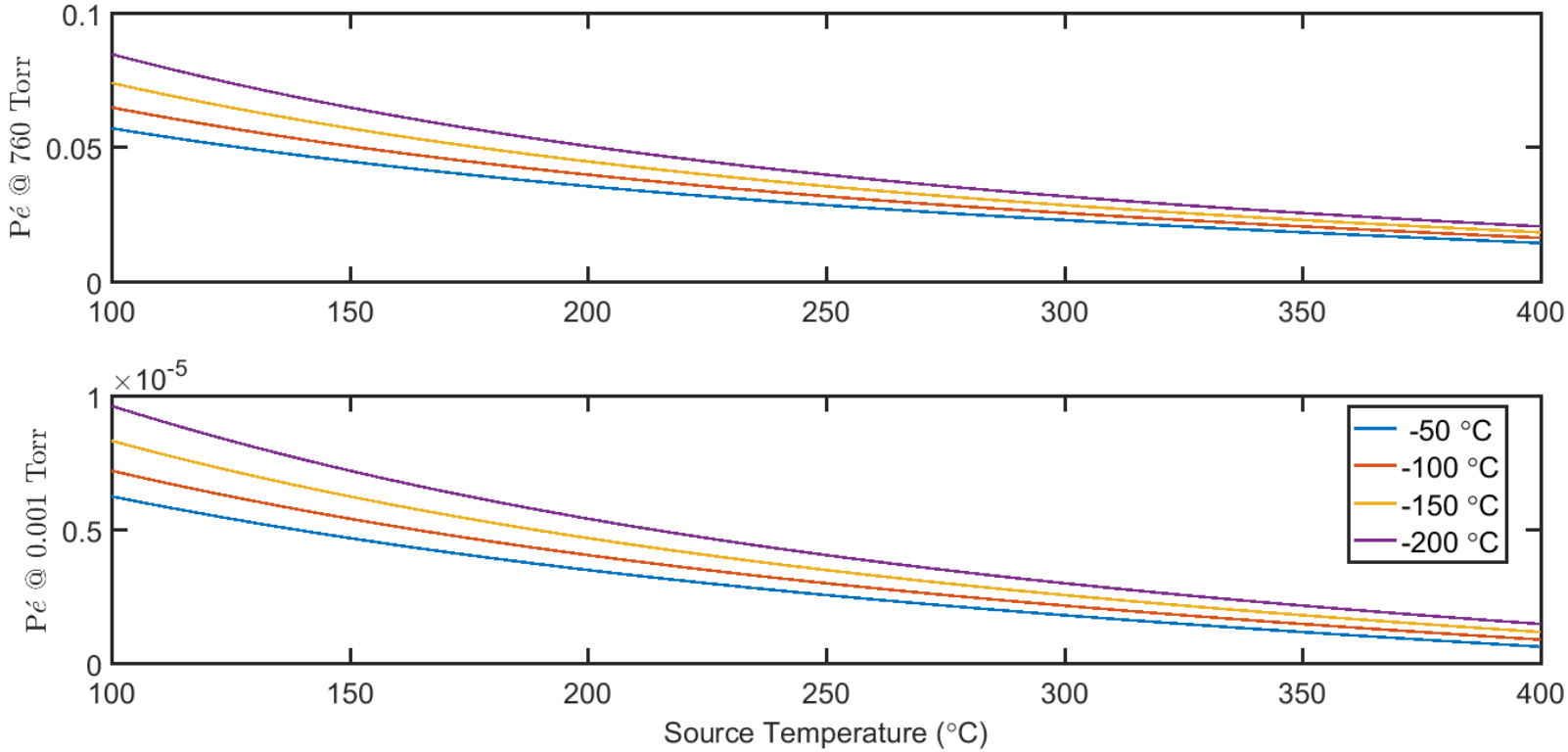

Figure 21 Pé values for the argon carrier gas calculated at multiple temperature drops between the source and substrate at 1.0E-3 and 760 Torr as the source temperature is increased from 100 °C to 400 °C.

Moreover, Ra trends calculated at the same temperature differences reinforce that natural convection is unable to be sustained at any of the system conditions studied in this investigation. These plots are shown below. Therefore, the primary heat transfer mechanism in the CSVT deposition region has been confirmed to be conduction based on dimensionless number calculations.

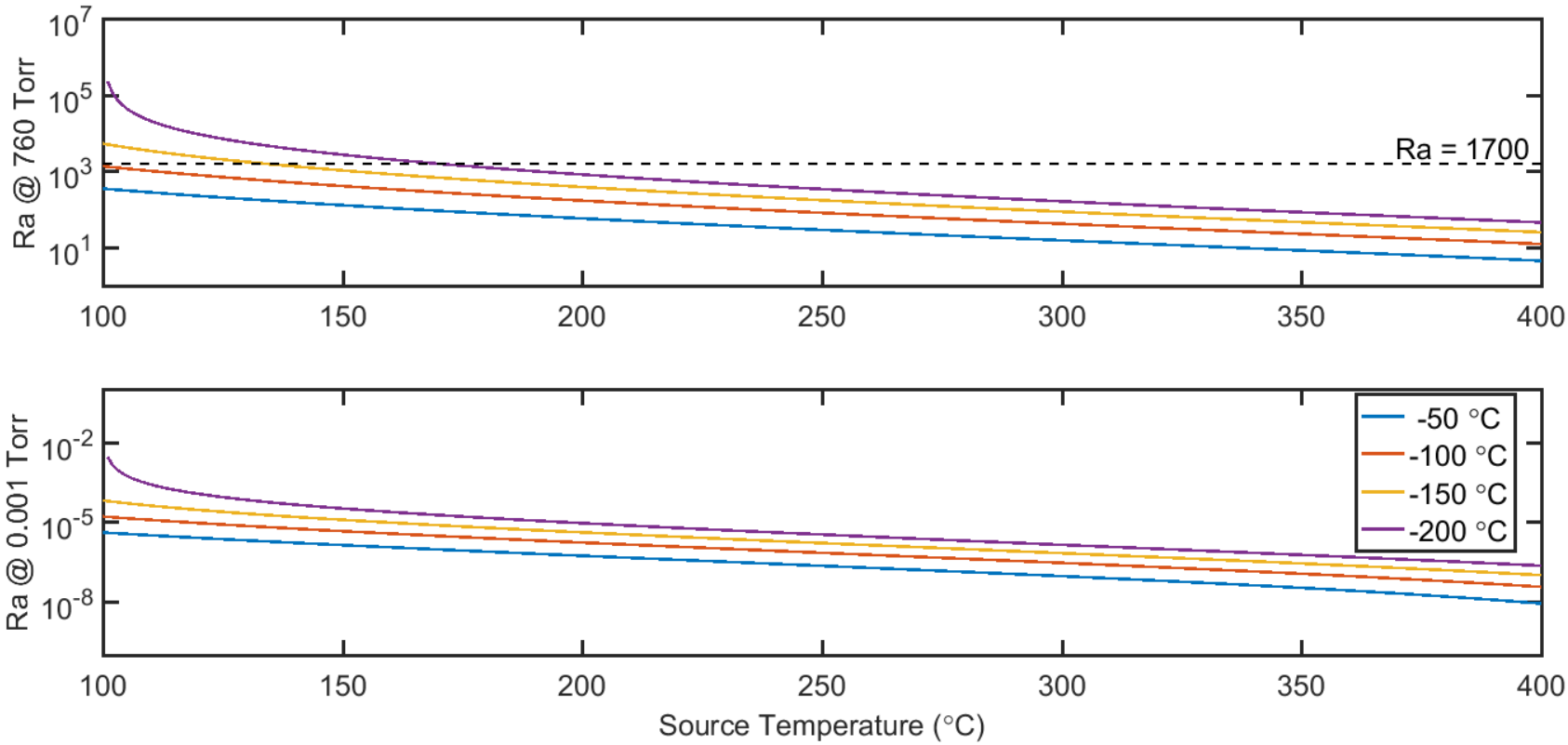

Figure 22 Ra values for the argon carrier gas calculated at multiple temperature drops between the source and substrate at 1.0E-3 and 760 Torr. The critical Ra value is labeled on the trends calculated at 760 Torr to note the onset of natural convection.

However, some of the other assumptions utilized to develop the deposition flux model were not observed during the case studies. The validity of assumptions 9 and 10 are called into question because the temperature driving force was observed to change as a function of time. Hence, the deposition flux was not at steady state. The mica insulation was unable to completely eliminate conduction between the source and substrate susceptors, due to their close proximity and additionally, conduction through the carrier gas, even at low pressures (~1 Torr). As a result, the temperature of the substrate increased within the time-scale of the deposition. This transient phase could take up to 30 minutes to stabilize, as illustrated by a selected number of PbI_2 deposition runs at ambient pressure featured in the figure on page 68.

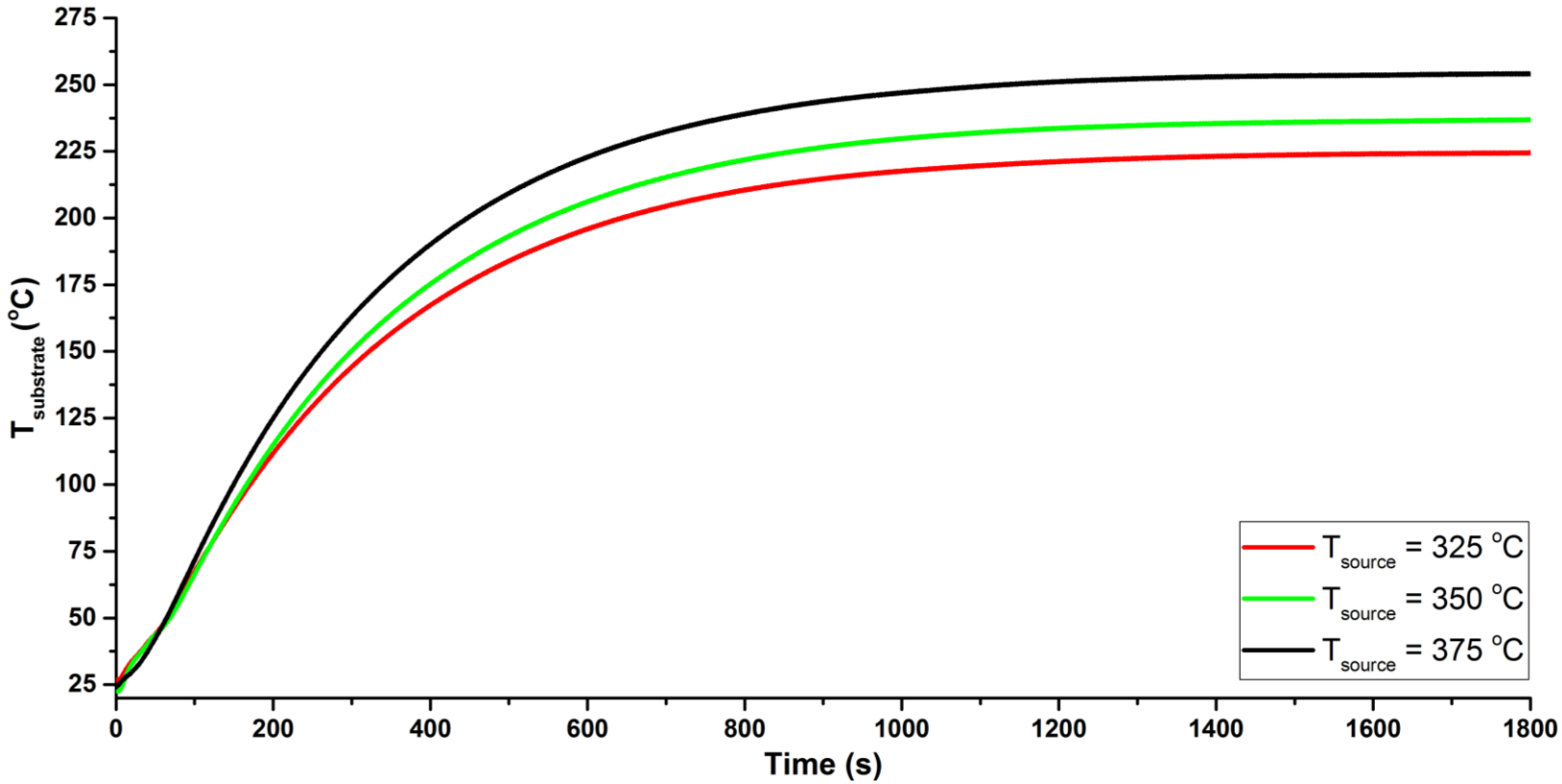

Figure 23 Substrate temperature profile during deposition of PbI_2 for 30 minutes at 760 Torr with a deposition area of 8.55 cm^2.

Mica is an ideal choice as an insulating material, having a very low thermal conductivity, high melting point, and is chemically inert and resistant to most substances. For instance, the results for the PbI_2 case studies show that the temperature difference between the source and substrate was on the order of 100 °C. But its inability to completely isolate heat emitted from the source susceptor results in a diminished driving force to the substrate. Instead, the sublimed material gradually defuses outside the deposition region. The material then deposits onto the cooler inner walls of the quartz tubing or is carried away by the cooler carrier gas.

Adjusting processing variables does not alleviate the issue. For instance, increasing the deposition height to further isolate the two sources only offsets the magnitude of the gradient, as shown in the figure below for PbI_2.

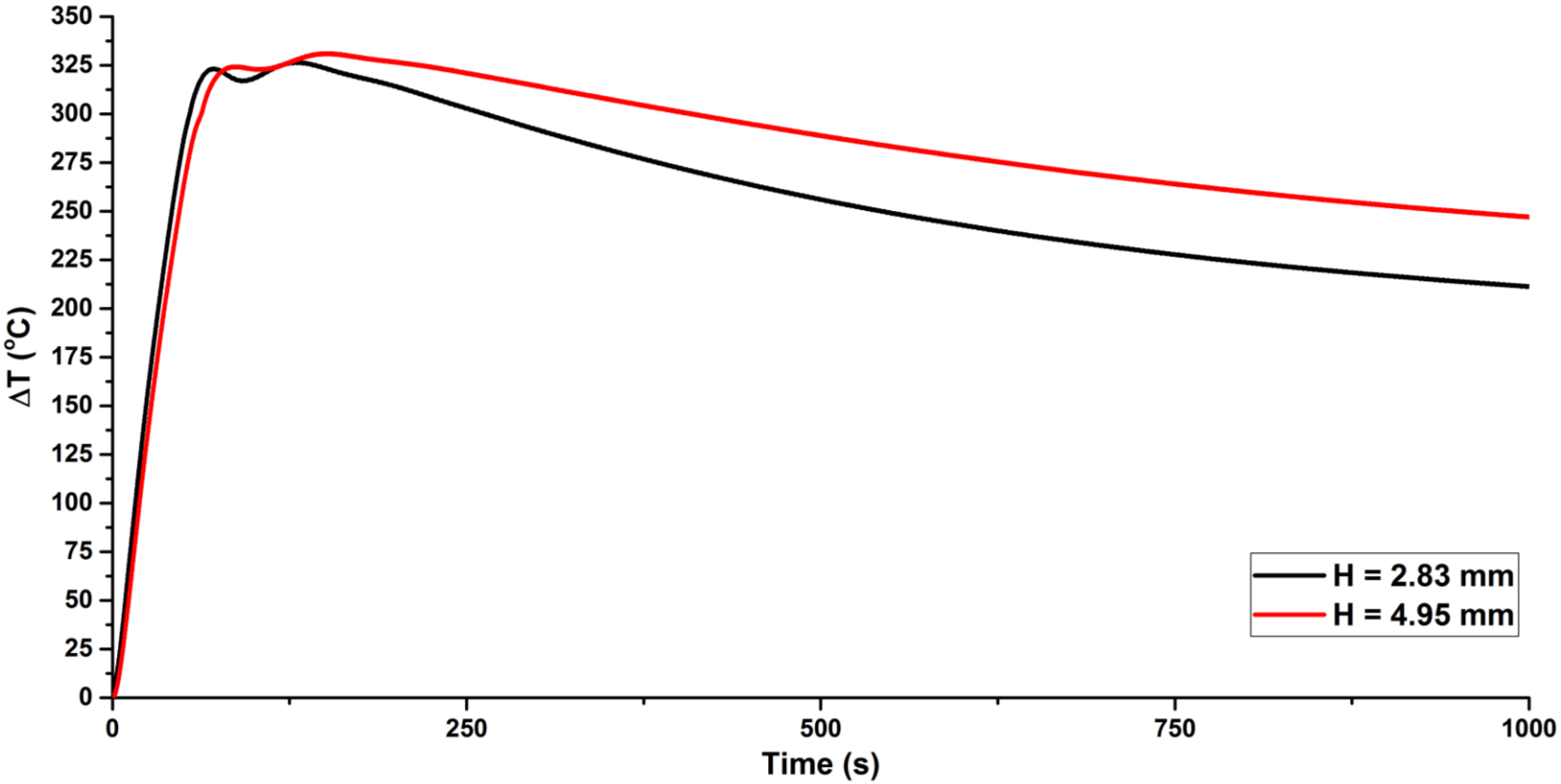

Figure 24 Temperature profiles of the temperature difference between the source and substrate susceptors recorded for two 4 cm^2 PbI_2 films deposited at 1 Torr and a source temperature of 375 °C for 15 minutes.

Based on the above, experimental times were set as short as five minutes to not only demonstrate fast deposition but also minimize the change in the temperature gradient. Thus, the substrate temperature shown in the result tables for PbI_2 and MAI is actually the median substrate temperature of the source selected as the representative value in the model. This approach was more successful with MAI due to the lower source temperature, hence smaller deviation in temperature gradient. Though, the application of the median source temperature in the model may have contributed to the overestimation in the deposition flux calculated for PbI_2. Since the temperature gradient between the source and substrate decreases over time, the deposition flux also decreases over that same period. However, by calculating the flux using a fixed value for the substrate temperature, the calculated gradient is larger than that of the empirical gradient, resulting in the calculated flux being greater than the actual flux.

The existence of a time-dependent temperature gradient also invalidates assumption 2 since material is diffusing outside of the deposition region. The mass change in the substrate was not equal to that of the source. The case study results for PbI_2 are reproduced in the table on page 72 with the arithmetic mean for the mass change in both sites. No consistent trends with temperature and pressure were observed in the discrepancy between the changes in the mass of the source versus that of the substrate.

Table 10 Reproduction of PbI_2 case study results with mass change in source and substrate according to each experimental condition

P_{sys} (Torr)	H (mm)	T_{source} (°C)	$T_{substrate}$ (°C)	Δm_{source} (g)	$\Delta m_{substrate}$ (g)
0.6	2.83	375	104.4	-(1.2±0.5)E-02	(1.1±0.4)E-02
0.6	2.83	385	109.0	-(2.8±0.7)E-02	(2.6±0.8)E-02
0.6	3.83	375	98.0	-(1.6±0.5)E-02	(1.1±0.5)E-02
0.6	3.83	385	99.5	-(1.7±0.5)E-02	(1.7±0.6)E-02
1.0	2.83	375	115.3	-(7.9±3.6)E-03	(5.9±4.2)E-03
1.0	2.83	385	119.8	-1.0E-02	(9.3±0.5)E-03
1.0	3.83	375	102.5	-(2.9±0.6)E-03	(3.2±0.1)E-03
1.0	3.83	385	103.8	-(5.7±2.6)E-03	(4.6±0.6)E-03

For MAI, even lower amounts of material reached the substrate, shown in the table on page 73. Unlike PbI_2, the discrepancy between the source and substrate increases with temperature under isobaric conditions. The empirical deposition flux was determined using the rate of mass loss from the source due to two observations: 1) the discrepancy in the mass change of the source and substrate observed in the PbI_2 deposition runs and 2) the proximity of the change in the mass of the substrate in the MAI case studies to the sensitivity limits of the balance. Though, theoretically the diffusion flux should be at steady state.

Table 11 Reproduction of MAI case study results with mass change in source and substrate according to each experimental condition

P_{sys} (Torr)	T_{source} (°C)	$T_{substrate}$ (°C)	Δm_{source} (g)	$\Delta m_{substrate}$ (g)
0.6	155	42.3	-(4.6±0.6)E-03	(4.0±1.0)E-04
0.6	165	43.3	-(6.2±2.3)E-03	1.1E-03
0.6	175	44.1	-(8.1±0.6)E-03	(1.9±0.1)E-03
1.0	155	45.4	-(3.8±1.3)E-03	(5.0±1.0)E-04
1.0	165	48.5	-(4.0±0.4)E-03	(1.1±0.1)E-03
1.0	175	50.9	-(6.2±1.9)E-03	(1.3±0.6)E-03

Alternative Approaches to Estimating Diffusivity of MAI and PbI_2 in Argon

Based on the PbI_2 case study results, the CE model overestimated the diffusivity of PbI_2 in argon. The cause of the overestimation most likely originated from the inaccuracies in estimating σ and ε/k using equations 3.16 and 3.17. But, estimating these constants using different thermo-physical parameters, such as the molar volume data at the normal boiling point or critical point, would be even more challenging since that information is difficult to locate for PbI_2. The best alternative would be locate experimental data of a PbI_2 vapor with another inert gas or for a compound with similar structure to PbI_2 in argon. But, limited availability to this type of data is the reason why the theoretical route was taken. Other options would be to select another estimation method, or measure the value empirically.

However, alternative methods are closely related to the CE model. For instance, the Hirschfelder, Bird, and Spotz (HBS) method is essentially the CE method modified with the inclusion of a collision integral data calculated by the Hirschfelder and colleagues (Wilke and Lee 1955). In fact, the collision integral relationship shown in equation 3.16, which was developed by Nefeld, Jansen, and Aziz, is based on an

improved calculation of the HBS values performed by Monchick and Mason (Bird et al. 2002). Hence, the CE and HBS methods will most likely produce similar results. Wilke and Lee also proposed a correction factor for the molecular weight term in the HBS method (Wilke and Lee 1955). However, this method is also a modification of the CE model, still harboring the same challenges with estimating σ and ε/k.

Other options closely follow the FSG method. For example, the relationship for the Arnold method is similar to that of the FSG method, introducing the Sutherland constant as a correction term to improve the model's response to temperature (Wilke and Lee 1955). Another alternative, the Gilliland method, has a format that is also akin to the FSG method, shown in equation (Gilliland 1934). Again, the similarities in the alternative models would not make a significant difference in the calculated D_{AB}

Overall, the challenges with theoretically calculating D_{AB} reinforces the need for empirical validation. Some commonly employed techniques for measuring D_{AB} include closed tube, evaporation tube, two-bulb apparatus, point source, and gas chromatography approaches, which are elaborated on by Marrero and Mason (Marrero and Mason 1972). However, a majority of these techniques require specially designed experimental apparatus which may not be readily available to an investigator, especially for the closed tube and two-bulb apparatus methods. Also, most approaches have temperature restrictions given the operating limitations of working mechanisms in the experimental apparatus.

The evaporation tube approach is the most applicable to measuring the diffusivity of the reactants studied in this investigation due to its well-documented application to a large number of binary systems with a diffusing species evaporating from a solid or liquid. This technique consists of a vertical tube of uniform cross

sectional area being filled with the solid or liquid state of the diffusing material, to a known height, while the remainder of the tube is filled with the bulk gas. Outside of the tube, the gas passes by at a flow rate that quickly dissipates any of the evaporating species as it leaves the tube, setting the boundary condition for the concentration of diffusing species at the top of the tube to zero. A schematic of the experimental design is shown on page 75.

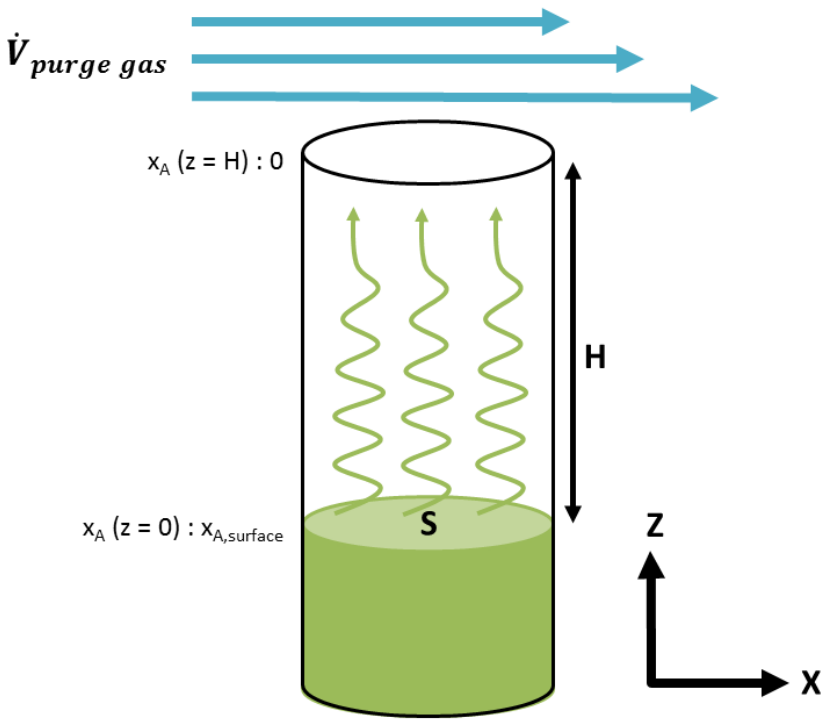

Figure 25 Evaporation Tube experimental apparatus

However, the approach is extremely sensitive to temperature and pressure fluctuations and requires accurate recording of initial sample height, meaning that a highly precise measurements would be necessary to ensure reproducibility (Marrero

and Mason 1972). Siddiqi and Atakan, adapted the evaporation tube approach for use with a TGA to perform measurements on the diffusivity of a number of organometallic compounds used in CVD applications, including ferrocene (Siddiqi and Atakan 2007). In their technique, a measured amount of material was packed, to a particular height, in a sample pan of known dimensions. The rate of mass loss was then recorded at a number of isothermal steps, held for a long period of time while the bulk gas passed over the pan at rates on the order of 100 cm^3/min. Since the experiments were conducted under ambient pressure, any deviation in the mole fraction of the bulk gas from unity was assumed to be negligible due to the significantly lower vapor pressure of the subliming material. This assumption simplified the materials balance on the diffusing species from the surface of the source to the top of the tube. The resulting relationship calculated D_{AB} as the product of the vapor pressure and actual value, shown in equation 4.4. The actual D_{AB} was then determined by measuring the vapor pressure of the material using the Knudsen effusion method. A similar approach is recommended for measuring the D_{AB} of MAI and PbI_2.

$$P_A D_{AB} = \left\{ \left(\frac{\Delta m}{S \rho_A} + H \right)^2 - H^2 \right\} \frac{RT \rho_A}{2 M_W t} \qquad 4.4$$

Where Δm is the change in the mass in kg, S is the surface area in m^2, t is the measurement time in s, and T is the measurement temperature in K.

Another approach is to estimate $P_A D_{AB}$ from the J_{AB} case study data. However, this route produces values that are dependent on processing conditions that D_{AB} is normally not a function of, such as deposition height and the temperature gradient, and are subject to systematic errors associated with the CSVT deposition apparatus. Below is a tabulation of $P_A D_{AB}$ calculated from the PbI_2 and MAI case studies using the mass

transport model (equation 3.13). The values are then compared to the product of D_{AB} calculated through respective theoretical models and P_A based on the Clausius-Clapeyron relations shown in equations 3.1and 3.2, respectively.

Table 12 $P_{PbI2}D_{AB}$ values calculated based on PbI_2 case study results versus CE method

P_{sys} (Torr)	H (mm)	T_{source} (°C)	$T_{substrate}$ (°C)	$P_{PbI2}D_{AB\text{-}EMP}$ (Pa*cm^2/s)	$P_{PbI2}D_{AB\text{-}CE}$ (Pa*cm^2/s)
0.6	2.83	375	104.4	24.0±7.9	8.1E02
0.6	2.83	385	109.0	58.7±10.7	1.3E03
0.6	3.83	375	98.0	40.7±8.3	8.1E02
0.6	3.83	385	99.5	44.2±9.4	1.3E03
1.0	2.83	375	115.3	16.0±5.2	5.0E02
1.0	2.83	385	119.8	21.3±0.3	8.0E02
1.0	3.83	375	102.5	7.2±1.1	5.0E02
1.0	3.83	385	103.8	14.6±4.8	8.0E02

Table 13 $P_{MAI}D_{AB}$ values calculated based on MAI case study results versus FSG method. P_{MAI}

P_{sys} (Torr)	T_{source} (°C)	$T_{substrate}$ (°C)	$P_{MAI}D_{AB\text{-}EMP}$ (Pa*cm^2/s)	$P_{MAI}D_{AB\text{-}FSG}$ (Pa*cm^2/s)
0.6	155	42.3	15.6±1.4	1.0E03
0.6	165	43.3	21.5±5.8	1.4E03
0.6	175	44.1	29.1±1.4	1.9E03
1.0	155	45.4	12.9±3.1	6.9E02
1.0	165	48.5	13.8±0.9	9.8E02
1.0	175	50.9	22.1±4.9	1.4E02

The theoretical product for PbI_2 and MAI under each set of process parameters is at least an order of magnitude greater than the corresponding values calculated out of equation 3.13. The cause in the discrepancy between the theoretical and empirical values could be associated with either D_{AB} or P_A. The inaccuracies originating from calculating or measuring D_{AB} have already been discussed. In terms of P_A, the likelihood of P_{PbI2} being an issue is low since its vapor pressure data is well-documented (Knacke et al. 1991; Konings et al. 1996). But P_{MAI} data is in need of verification, responsible for the large discrepancies in $P_{MAI}D_{AB\text{-}FSG,}$ the inverse relationship between D_{AB} values calculated using the FSG method, and virtually no change in the corresponding flux. D_{AB} is directly related to temperature and inversely related to pressure, a relationship that is present in all the theoretical and empirical models that have been showcased to this point. But, in the case study data the change in $D_{AB\text{-}FSG}$ was inversely related to temperature under isobaric conditions. Furthermore, the corresponding $J_{AB\text{-}FSG}$ trends were stagnant under the same conditions. MAI has not been studied as extensively as PbI_2, resulting in few sources for reliable thermos-physical and mass transport property data. The P_{MAI} data used in this investigation originates from the only known published source from Dualeh and colleagues (Dualeh, Gao, et al. 2014) and suggests that MAI volatility is higher than what was observed. The MAI case study results are reproduced below with the corresponding P_{MAI} data. If P_{MAI} was as high as Dualeh's suggests, then the decrease in $D_{AB\text{-}FSG}$ with temperature and the minimal change in J_{ABFSG} would be justified since the overall pressure of the system would increase.

Table 14 MAI case study results with corresponding vapor pressure data predicted from Dualeh and colleagues (Dualeh, Gao, et al. 2014)

P_{sys} (Torr)	T_{source} (°C)	$T_{substrate}$ (°C)	P_{vap} (Torr)	Δm_{source} (g)	J_{AB} (g/cm^{2}s)
0.6	155	42.3	4.1	-(4.6±0.6)E-03	-(3.8±0.5)E-06
0.6	165	43.3	8.1	-(6.2±2.3)E-03	-(5.1±1.9)E-06
0.6	175	44.1	15.4	-(8.1±0.6)E-03	-(6.8±0.5)E-06
1.0	155	45.4	4.1	-(3.8±1.3)E-03	-(3.2±1.1)E-06
1.0	165	48.5	8.1	-(4.0±0.4)E-03	-(3.3±0.3)E-06
1.0	175	50.9	15.4	-(6.2±1.9)E-03	-(5.1±1.6)E-06

The conflict between the trends in the observed and calculated deposition parameters prompts validation of P_{MAI}. Thermogravimetric analysis (TGA) was employed to quantify the sublimation properties of MAI, starting with differential scanning calorimetry (DSC) to analyze the material's stability from room temperature to 300°C, the maximum temperature Dualeh and colleagues studied their MAI samples. These measurements were performed on approximately 40 mg material housed in a 90 µL alumina sample pan under a 100 cm^3/min of nitrogen flow in a TA Instruments SDT Q600 TGA/DSC system with calibrated mass flow controller. The results revealed that the material undergoes two thermodynamic phase changes, shown in the figure below.

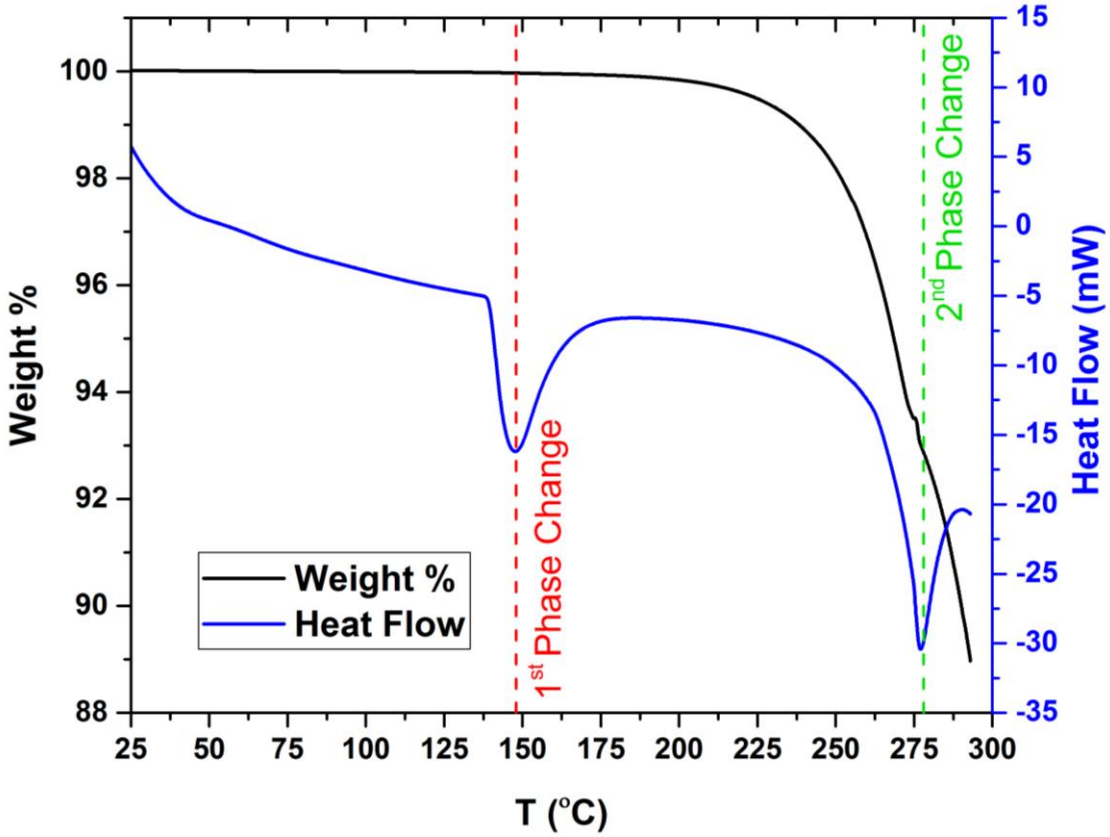

Figure 26 DSC temperature survey of MAI in nitrogen gas noted two thermodynamic phase changes. Significant weight loss was not seen until temperatures reached above 200 °C.

The first phase change was observed around 150°C corresponds with sintering. Dualeh calculated the temperature at which the vapor pressure of MAI is 760 Torr, or the T_{sub}, to be greater than 250 °C (Dualeh, Gao, et al. 2014). In the DSC results, mass loss was observed at that temperature but its proximity to the second phase transition at 275 °C calls into question if that temperature truly corresponds to sublimation since the material was observed to rapidly deteriorate and melt. If degradation does occur or the melting point is reached over the temperature ranges Dualeh studied, it may have impacted the vapor pressure data. Dualeh employed TGA but did not disclose enough

details on experimental design, particularly the pressure at which they operated their TGA system. Based on the inclusion of T_{sub}, the experiments were most likely conducted at ambient pressure but that is never explicitly stated. While utilizing TGA to measure P_A is a simple technique, the experimental design is critical to obtaining accurate results. Lack of full details of their procedure is a concern since their values cannot be reproduced and elements of the design could result in measuring inaccurate values, such as the sample decomposition and measuring values at ambient pressure. The rate of mass loss will be suppressed within this diffusion-limited regime due to the pressure of the surrounding atmosphere being significantly higher than the P_A of the material. Further analysis is required to determine the exact melting point of the material, what the MAI decomposes into, and if the behavior varies with the source of the MAI. But, based on Dualeh's published experimental procedure, the discrepancy observed in the case study data, and degradation of MAI observed during DSC, the accuracy of the vapor pressure data and corresponding ΔH_{sub}° published by Dualeh and colleagues requires validation.

Experiments for validating the vapor pressure of a material like MAI are well-documented. Please refer to selected references from Gillan and Vieyra-Eusebio for further details (Gillan et al. 1997; Vieyra-Eusebio and Rojas 2011). The vapor pressure of MAI was also estimated using TGA in this investigation. Vapor pressure determination using TGA involves measuring the rate of mass loss of the material at selected temperatures below the melting point for an extended period of time under vacuum. The desired trend is linear, translating to no degradation in the material or change in the surface area of the material over that period of time. The data can then be incorporated into the Hertz-Langmuir relation (equation 3.6) to calculate the vapor

pressure. Linear regression of the natural logarithm of the vapor pressure data versus the inverse of the temperature, in K, will compute the constants for the Clausius-Clapeyron equation, including ΔH_{sub}° (Gillan et al. 1997). The Hertz-Langmuir relation was originally developed for calculating P_A using mass loss data collected under vacuum due to the possibility of underestimating the rate of mass loss. Thus, P_A determination of TGA should be performed under the same conditions even though the common approach is to conduct the experiments at ambient pressure. Unfortunately, such facilities were not available to illustrate this concept in this investigation but an alternative approach was explored. The CSVT system was employed to collect rate loss data under 200 °C. A preliminary experiment was conducted, assuming that the rate of mass loss would be linear. These experiments predated the case studies, when the change in the mass of the source and substrate were assumed to be equal. Hence, only the rate of change in the mass of the substrate was recorded. Deposition runs were conducted for 15 minutes at 150, 160, and 170 °C at 0.5 Torr and argon flow rate of 70 SCCM. The results are shown in the table below. Vapor pressure was calculated using equation 3.6 and used to derive Clausius-Clapeyron coefficients. The fit and corresponding equation displayed in the figure on page 84. The ΔH_{sub}° was calculated to be 55.8±1.6 kJ/mol, approximately half of that published by Dualeh. Note that at this point in the time temperature control within this range was a challenge so actual T_{source} values fluctuated around 2 °C from the set point and changes in the mass were close to the sensitivity limits of the mass balance. Future replicates should be conducted under much more accurate temperature profiles and performed under deposition times that are at least twice as long to ensure a change in the mass that is well above the sensitivity limit of the balance.

Table 15 Preliminary data from CSVT system for empirically determining P_{vap} , calculated using the Hertz-Langmuir (HL) relationship

T_{source} (°C)	$T_{substrate}$ (°C)	$\dot{m}_{substrate}$ (g/s)	J_{AB} (g/cm^{2}s)	$P_{vap\text{-}HL}$ (Pa)
150	68.6	(5.6±1.6)E-07	-(1.4±0.4)E-07	5.2E-04
160	74.0	(7.8±2.5)E-07	-(1.9±0.6)E-07	7.3E-04
170	80.0	(1.1±0.3)E-06	-(2.8±0.6)E-07	1.1E-03

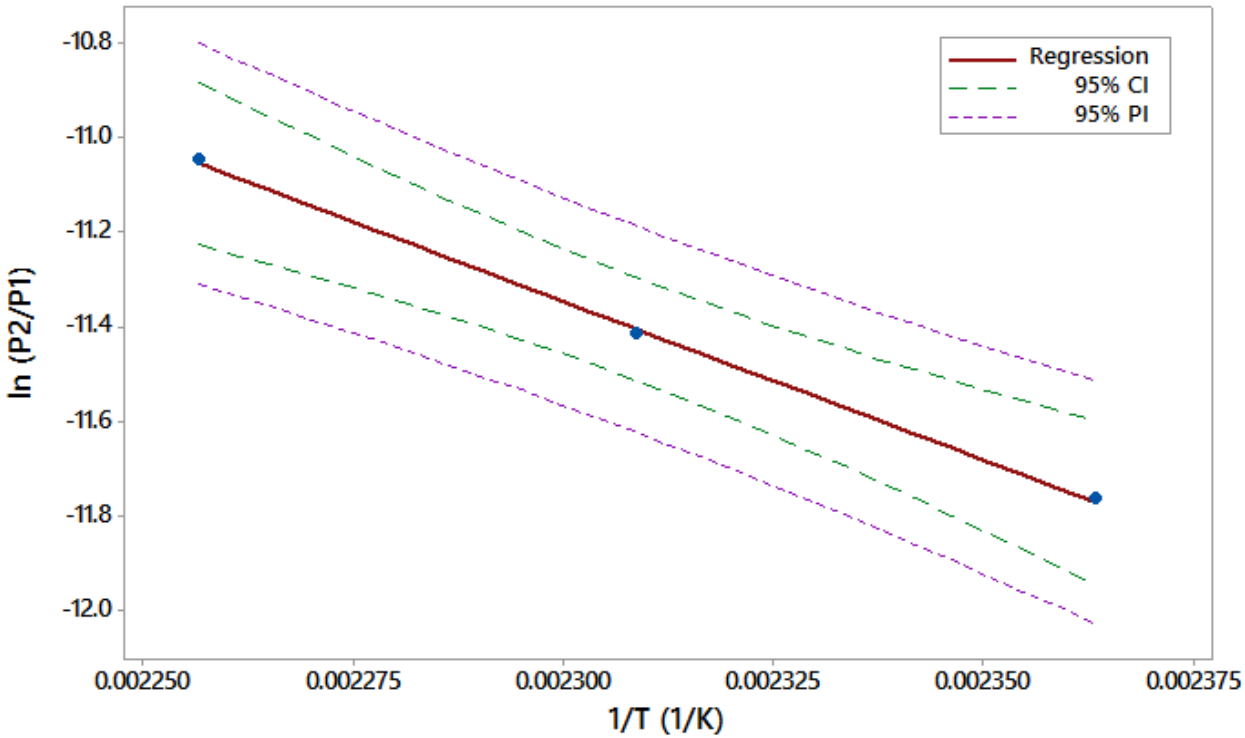

Figure 27 Clausius-Clapeyron curve fit for MAI based on preliminary data collected using CSVT system, displaying the 95% confidence interval (CI) and prediction interval (PI) from 150 to 170 °C. The linear model is ln (P_2/P_1) = -(6.7±0.2)E3/T+4.0±0.5, where P_1 = 0.5 Torr and the uncertainty values for each constant are the standard error of the estimate, which is calculated in a similar fashion as the standard deviation. Full regression analysis is located in the appendix.

To show the result of collecting mass loss data at ambient pressure the measurements were also conducted in the same Q600 SDT system employed for the DSC measurements. A sample of 0.20 g of MAI was packed and sintered at 150 °C for 15 minutes in a 90 µL alumina sample pan prior to analysis. The rate of mass loss was recorded under argon gas flow rate of 5 cm^3/min from 75 to 200 °C with isothermal step times of 15 minutes each at ambient pressure. The temperature and rate mass loss profiles are shown in the figure on page 86, accompanied by a table of the results and calculated P_{MAI} values. The Clausius-Clapeyron coefficients were generated in the same manner, the empirical data along with the corresponding fit displayed in the figure on page 87. The ΔH°_{sub} was calculated to be 71±5.5 kJ/mol, a higher value than that of the preliminary results but still lower than published by Dualeh.

The comparison of J_{AB} calculated with both the preliminary and TGA derived P_{MAI} data is tabulated on page 88. The values calculated from the TGA data are about two orders of magnitude lower than that of the actual flux. In contrast, the preliminary measurements are closer in agreement to that of the empirical results. Again, while the approach of determining P_A at ambient pressures has been adopted as a common practice, based on the vapor pressure data collected in this investigation, any further validation of these values should be conducted under vacuum (Langmuir 1913; Siddiqi and Atakan 2007).

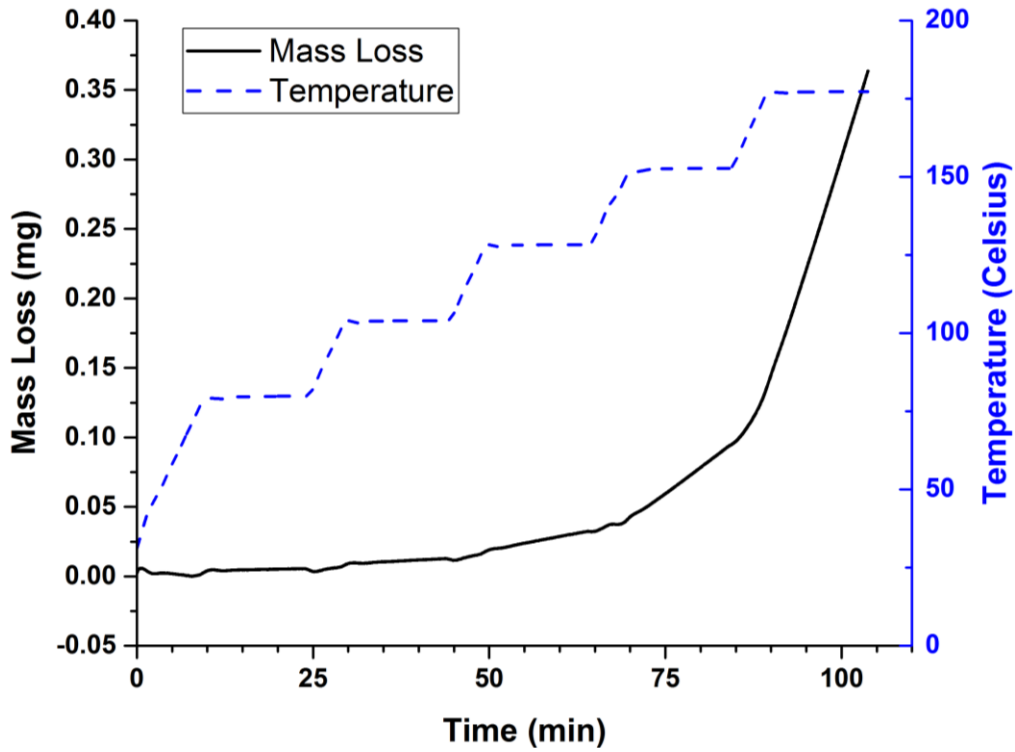

Figure 28 TGA results for MAI, depicting mass loss at each programmed isothermal step

Table 16 TGA data for empirically determining P_{vap} , calculated using the Hertz-Langmuir (HL) relationship

T (°C)	$\dot{m}_{loss}$ (g/s)	J_{AB} (g/cm2s)	$P_{vap\text{-}HL}$ (Pa)
80	-1.7E-09	-7.1E-09	2.4E-05
104	-4.7E-09	-2.0E-08	7.1E-05
128	-1.6E-08	-6.9E-08	2.5E-04
153	-6.1E-08	-2.6E-07	9.8E-04
177	-2.7E-07	-1.2E-06	4.5E-03

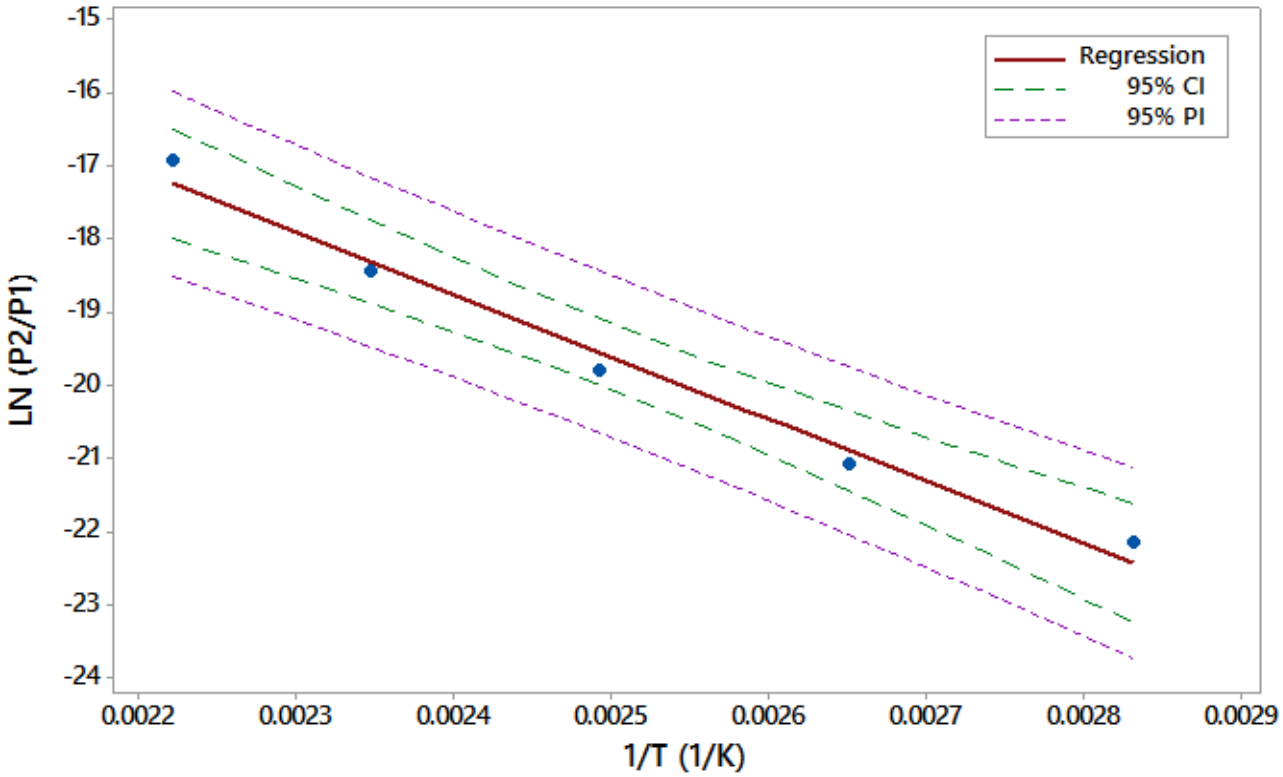

Figure 29 Derivation of Clausius-Clapeyron relationship for TGA mass loss survey of MAI, displaying the 95% confidence interval (CI) and prediction interval (PI) from 80 to 177 °C. The linear model is ln (P_2/P_1) = -(8.5±0.7)E3/T+1.6±1.7, where P_1 = 760 Torr and the uncertainty values for each constant are the standard error of the estimate. Full regression analysis is located in the appendix.

Table 17 Reproduction of MAI case study results in comparison to that generated using P_{vap} measured from both preliminary (PRE) and TGA methods.

P_{sys} (Torr)	T_{source} (°C)	$T_{substrate}$ (°C)	Δm_{source} (g)	$J_{AB\text{-}EMP}$ (g/cm2s)	$P_{vap\text{-}TGA}$ (Pa)	$J_{AB\text{-}TGA}$ (g/cm2s)	$P_{vap\text{-}PRE}$ (Pa)	$J_{AB\text{-}PRE}$ (g/cm2s)
0.6	155	42.3	-(4.6±0.6)E-03	-(3.8±0.5)E-06	0.12	-1.9E-08	6.0E-04	-1.4E-05
0.6	165	43.3	-(6.2±2.3)E-03	-(5.1±1.9)E-06	0.20	-3.0E-08	9.0E-04	-2.0E-05
0.6	175	44.1	-(8.1±0.6)E-03	-(6.8±0.5)E-06	0.30	-4.7E-08	1.2E-03	-2.9E-05
1.0	155	45.4	-(3.8±1.3)E-03	-(3.2±1.1)E-06	0.12	-1.1E-08	6.0E-04	-8.5E-06
1.0	165	48.5	-(4.0±0.4)E-03	-(3.3±0.3)E-06	0.20	-1.8E-08	9.0E-04	-1.2E-05
1.0	175	50.9	-(6.2±1.9)E-03	-(5.1±1.6)E-06	0.30	-2.8E-08	1.2E-03	-1.7E-05

Sources of Systematic Errors

Variability in replicated results and inaccuracies in J_{AB} calculated by the model may have also been due to a number of systematic errors, including lack of control in adjusting the vacuum valve orifice to counteract fluctuations in the extraction rate of the carrier gas, the transient temperature gradient, and accuracy of the analog readout of the pressure gauge.

Overall, the mass transfer model developed for predicting the diffusion flux of PbI_2 and MAI in argon overestimates actual values based on case study results. However, the values are within the same order of magnitude. Sources of inaccuracies may originate from the assumptions applied to the model, the method used to calculate D_{AB} and, in the case of MAI, the accuracy of vapor pressure data. Counteracting the impact of the transient temperature difference during deposition will be a challenge. But, further investigation to compute more accurate diffusivities is feasible. The final chapter of this discussion will elaborate more on suggested future experiments generate more accurate constants for evaluating the model.

Chapter 5

CONCLUSIONS AND FUTURE WORK

OHP PV devices have gained momentum in the past few years as a potential contender to more mature PV technologies, particularly CIGS and crystalline silicon. Part of their success has been attributed to their minimal requirements for synthesis, making them applicable with a versatile range of solution-based and vapor-based deposition techniques. Initially, solution-based deposition, particularly spin coating, was the most commonly employed approach to generating OHP films. However, work presented in this thesis reinforced issues regarding spin coating films: the lack of control over processing variables, challenges with reproducibility, and poor scalability. In contrast, vapor deposition techniques generate films in highly-controlled environments and have better potential for upscale manufacturing. CSVT is one notable example that has already been employed in the PV industry to manufacture CdTe cells which is a highly controllable vapor deposition technique that is potential scalable technique for depositing OHP films for PV applications. To demonstrate its capabilities, a model was developed based on Fick's law of molecular diffusion to predict the deposition flux of the sequentially deposited reactants used to make $MAPbI_3$, MAI and PbI_2. This model will aid in optimizing the processing conditions of the system to generate high-quality $MAPbI_3$ films to be incorporated into devices.

Overall, the mass transport model demonstrates the high degree of control for synthesizing $MAPbI_3$ films using CSVT but some assumptions used to develop it require reevaluation. Notably, the transient temperature gradient in the actual system corresponds to a diminishing deposition flux and a portion of the sublimating material

depositing outside of the deposition region. This observation calls in to question two major assumptions: 1) a constant temperature gradient and 2) diffusion of material is isolated to the deposition region. Consequently, the model will always overestimate the deposition flux since its calculations are based on the maximum amount of available material is being transported to the substrate. Also, the model needs to be modified to better incorporate additional aspects of the deposition system. For instance, the bulk gas is not purely argon and is moving, two factors that were ignored when calculating the Ra for determining the primary mechanism for heat transfer. The Ra calculations may reach a different conclusion upon incorporating those aspects of the system. Furthermore, a more accurate calculation of the diffusivity of MAI and PbI_2 in argon is required to improve the model's accuracy. The empirical route may be the most appropriate approach given challenges with calculating these constants, discussed in chapter 4, but will require reliable P_{vap} data in order to determine the diffusivity of MAI. Other aspects include the need to identify the maximum pressure which deposition is feasible and the maximum source temperature for heating MAI to set clearer operational limits based on the thermodynamic properties of each reactant and not just based on that of the limits of the system. The remainder of this chapter will further discuss these shortcomings and suggestions on how to rectify them.

Understanding system limitations will also aid in improving the accuracy of the model. The thermally isolating the source and substrate is a challenge due to the applicable scale for the deposition height. As a result, a transient temperature gradient is generated that impacts the deposition flux. Quantifying this discrepancy under different operating conditions would help minimize one of the major challenges with

adjusting the model to accurately portray the deposition system. This would be done by measuring the change in the rate of mass loss of each reactant when subject to a diminishing temperature gradient using TGA, similar to that observed during deposition in the CSVT system. This would quantify the magnitude by which the deposition flux decreases with respect to if the CSVT system maintained a constant driving force.

Identifying the primary method of heat transfer during CSVT was determined by analyzing dimensionless numbers, assuming that the composition of the carrier gas was strictly argon. However, the inclusion of another species may lead to a different results. Further investigation is needed to identify how to modify the calculations of Ra and Pé for gas mixtures. Also, though the carrier gas moves at a very slow rate through the system, comparing the arrangement of the deposition region to that of the Poiseuille-Bénard system would be more valid if the carrier gas was stagnant. Hence, the method used to calculate Ra needs to be re-evaluated to account for a system where the bulk gas is moving. Overall, these follow-up calculations would provide a more accurate depiction of how heat is transferred throughout the deposition region of the system.

Of the options for empirical methods discussed to determine the diffusivity of MAI and PbI_2 in the previous chapter, the evaporation tube technique was cited as the most appropriate approach to implement given available resources and ease of experimental design. But in order to employ the evaporation tube method on MAI, P_{MAI} data is necessary. Unfortunately, the accuracy of current available data for this

material is debatable based the observed discrepancy between empirical and calculated deposition flux trends and independent evaluation of P_{MAI} versus the data published by Dualeh, et al. (Dualeh, Gao, et al. 2014). The preliminary rate mass loss data collected using the CSVT system under vacuum suggested the P_{MAI} and ΔH_{sub}° published by Dualeh were overestimated. Conducting a similar approach as Dualeh employed by utilizing TGA to measure rate mass loss data under ambient pressure also lead to the same conclusion. But, the TGA studies would need to be conducted under vacuum to ensure that the MAI sublimates unhindered. Therefore, an appropriate follow-up investigation would be to perform TGA studies under high vacuum to measure vapor pressure of MAI and properly validate Dualeh's data. Also, additional data needs to be obtained on the physical properties of MAI, particularly its melting point and thermal decomposition route to set a maximum threshold for heating the material and distinguish impurities originating from the synthesis procedure from that of the decomposed product when analyzing films, respectively.

From a processing standpoint, the maximum pressure for depositing films needs to be determined. The system pressure can be changed by adjusting the carrier gas flow rate or the degree the vacuum orifice valve is opened. However, adjusting the carrier gas flow rate also influences the fluid dynamics and heat transfer within the deposition system. Based to the dimensionless number analysis, the system operates in a laminar flow regime, which corresponds to conductive heat transfer through the susceptor apparatus and the carrier gas. However, the transfer of sublimed material from the source to the substrates ceases above a certain flow rate, which may still correspond to laminar flow. In fact, flooding the system with carrier gas is the

standard procedure for ending a deposition run. This carrier gas flow rate threshold translates to the maximum operational system pressure, which unfortunately could not be located in the time allotted for this study but should be identified for future investigations.

REFERENCES

1. A checklist for photovoltaic research. 2015. Nat. Mater. 14:1073–1073.

2. Aristidou N, Sanchez-Molina I, Chotchuangchutchaval T, Brown M, Martinez L, Rath T, Haque S a. 2015. The role of oxygen in the degradation of methylammonium lead trihalide perovskite photoactive layers. Angew. Chemie - Int. Ed.

3. Barrows A, Pearson A, Kwak C, Dunbar A, Buckley A, Lidzey D. 2014. Efficient planar heterojunction mixed-halide perovskite solar cells deposited via spray-deposition. Energy Environ. Sci. 7:1–7.

4. Bi D, El-Zohry AM, Hagfeldt A, Boschloo G. 2014. Improved morphology control using a modified two-step method for efficient perovskite solar cells. ACS Appl. Mater. Interfaces 6:18751–18757.

5. Bird RB, Stewart WE, Lightfoot EN. 2002. Transport Phenomena. 2nd ed. New York: John Wiley & Sons.

6. Boix PP, Agarwala S, Koh TM, Mathews N, Mhaisalkar SG. 2015 Feb. Perovskite solar cells: beyond methylammonium lead iodide. J. Phys. Chem. Lett. [accessed 2015 Feb 23]. http://dx.doi.org/10.1021/jz502547f

7. Boopathi KM, Ramesh M, Perumal P, Huang Y-C, Tsao C-S, Chen Y-F, Lee C-H, Chu CW. 2015 Feb 19. Preparation of metal halide perovskite solar cells through liquid droplet assisted method. J. Mater. Chem. A.

8. Bretschneider SA, Weickert J, Dorman J a., Schmidt-Mende L. 2014. Research Update: Physical and electrical characteristics of lead halide perovskites for solar cell applications. APL Mater. 2:40701.

9. Burschka J, Pellet N, Moon S-J, Humphry-Baker R, Gao P, Nazeeruddin MK, Grätzel M. 2013. Sequential deposition as a route to high-performance perovskite-sensitized solar cells. Nature 499:316–9.

10. Chen C-W, Kang H-W, Hsiao S-Y, Yang P-F, Chiang K-M, Lin H-W. 2014. Efficient and uniform planar-type perovskite solar cells by simple sequential vacuum deposition. Adv. Mater. 26:6647–6652.

11. Chen L, Lee J, McCandless BE, Soltanmohammad SS, Shafarman WN. 2014. Characterization of group I-rich growth during (Ag,Cu)(In,Ga)Se2 three-stage co-evaporation. 2014 IEEE 40th Photovolt. Spec. Conf. PVSC 2014:332–336.

12. Chiang C-H, Tseng Z-L, Wu C-G. 2014. Planar heterojunction perovskite/PC71BM solar cells with enhanced open-circuit voltage via a (2/1)-step spin-coating process. J. Mater. Chem. A 2.

13. Conings B, Drijkoningen J, Gauquelin N, Babayigit A, D'Haen J, D'Olieslaeger L, Ethirajan A, Verbeeck J, Manca J, Mosconi E, et al. 2015 Jun 1. Intrinsic thermal instability of methylammonium lead trihalide perovskite. Adv. Energy Mater.

14. Du T, Wang N, Chen H, Lin H, He H. 2015. Comparative study of vapor and solution-crystalized perovskite for planar heterojunction solar cells.

15. Dualeh A, Gao P, Seok S Il, Nazeeruddin MK, Grätzel M. 2014. Thermal behavior of methylammonium lead-trihalide perovskite photovoltaic light harvesters. Chem. Mater. 26:6160–6164.

16. Dualeh A, Tétreault N, Moehl T, Gao P, Nazeeruddin MK, Grätzel M. 2014. Effect of Annealing Temperature on Film Morphology of Organic-Inorganic Hybrid Pervoskite Solid-State Solar Cells. Adv. Funct. Mater. 24:3250–3258.

17. Eperon GE, Burlakov VM, Docampo P, Goriely A, Snaith HJ. 2014. Morphological control for high performance, solution-processed planar heterojunction perovskite solar cells. Adv. Funct. Mater. 24:151–157.

18. First Solar. 2016a. Copper Mountain Solar 1.

19. First Solar. 2016b. Avra Valley Solar Project.

20. Fuller EN, Ensley K, Giddings JC. 1969. Diffusion of halogenated hydrocarbons in helium. The effect of structure on collision cross sections. J. Phys. Chem. 73:3679–3685.

21. Fuller EN, Schettler PD, Giddings JC. 1966. A new method for prediction of binary gas-phase diffusion coefficients. Ind. Eng. Chem. 16:551.

22. Gao C, Liu J, Liao C, Ye YQ, Zhang Y, He X, Guo X, Mei J, Lau LWM. 2015. Formation of organic-inorganic mixed halide perovskite films by thermal evaporation of PbCl2 and CH3NH3I compounds. RSC Adv. 5:26175–26180.

23. Geankoplis C. 2003. Transport processes and separation process principles. 4th ed. Upper Saddle River, NJ, USA: Prentice Hall Press.

24. Gillan EG, Bott SG, Barron AR. 1997. Volatility studies on gallium chalcogenide cubanes: thermal analysis and determination of sublimation enthalpies. Chem. Mater. 9:796–806.

25. Gilliland ER. 1934. Diffusion coefficients in gaseous systems. Ind. Eng. Chem. 26:681–685.

26. Gonzalez-Pedro V, Juarez-Perez EJ, Arsyad WS, Barea EM, Fabregat-Santiago F, Mora-Sero I, Bisquert J. 2014. General working principles of CH3NH3PbX3 perovskite solar cells. Nano Lett. 14:888–893.

27. Green MA. 2005. Silicon photovoltaic modules: A brief history of the first 50 years. Prog. Photovoltaics Res. Appl. 13:447–455.

28. Green MA, Emery K, Hishikawa Y, Warta W, Dunlop ED. 2015. Solar cell efficiency tables (version 46). Prog. Photovoltaics Res. Appl. 23:805–812.

29. Hailegnaw B, Kirmayer S, Edri E, Hodes G, Cahen D. 2015. Rain on methylammonium lead iodide based perovskites: possible environmental effects of perovskite solar cells. J. Phys. Chem. Lett.:1543–1547.

30. Hauke G. 2008. An introduction to fluid mechanics and transport phenomena. Dordrecht: Springer Netherlands (Fluid mechanics and its applications).

31. Hegedus S. 2006. Thin film solar modules: the low cost, high throughput and versatile alternative to Si wafers. Prog. Photovoltaics Res. Appl. 14:393–411.

32. ICDD. 2013. PDF 00-010-0037.

33. Im J-H, Jang I-H, Pellet N, Grätzel M, Park N-G. 2014. Growth of CH3NH3PbI3 cuboids with controlled size for high-efficiency perovskite solar cells. Nat. Nanotechnol. 9:927–932.

34. Im J-H, Kim H-S, Park N-G. 2014. Morphology-photovoltaic property correlation in perovskite solar cells: One-step versus two-step deposition of CH3NH3PbI3. APL Mater. 2:81510.

35. Ito S, Tanaka S, Nishino H. 2015. Lead-halide perovskite solar cells by CH3NH3I-dripping on PbI2-CH3NH3I-DMSO precursor layer for planar and porous structures using CuSCN hole transporting material. J. Phys. Chem. Lett.:150218122650001.

36. Jordan DC, Kurtz SR. 2013. Photovoltaic degradation rates-an analytical review. Prog. Photovoltaics Res. Appl. 21:12–29.

37. Jung HS, Park N-G. 2014. Perovskite solar cells: from materials to devices. Small 11:10–25.

38. Jung M-C, Raga SR, Qi Y. 2016. Properties and solar cell applications of Pb-free perovskite films formed by vapor deposition. RSC Adv. 6:2819–2825.

39. Kern W, Schuegraf KK. 2001. Deposition technologies and applications: introduction and overview. In: Seshan K, editor. Handbook of thin film deposition processes and techniques. 2nd ed. Norwich, NY: William Andrew Publishing. p. 11–43.

40. Kim H-S, Lee C-R, Im J-H, Lee K-B, Moehl T, Marchioro A, Moon S-J, Humphry-Baker R, Yum J-H, Moser JE, et al. 2012. Lead iodide perovskite sensitized all-solid-state submicron thin film mesoscopic solar cell with efficiency exceeding 9%. Sci. Rep. 2:591.

41. Knacke O, Kubaschewski O, Hesselmann K. 1991. Thermochemical Properties of Inorganic Substances. 2nd ed. Knacke O, Kubaschewski O, Hesselmann K, editors. Berlin: Spriner-Verlag.

42. Ko H-S, Lee J-W, Park N-G. 2015 Mar 16. 15.76% efficiency perovskite solar cell prepared under high relative humidity: importance of PbI2 morphology in two-step deposition of CH3NH3PbI3. J. Mater. Chem. A.

43. Kojima A, Teshima K, Shirai Y, Miyasaka T. 2009. Organometal halide perovskites as visible-light sensitizers for photovoltaic cells. J. Am. Chem. Soc. 131:6050–6051.

44. Konings RJM, Cordfunke EHP, Fearon JE, van der Laan RR. 1996. The infrared spectrum and vapour pressure of lead diiodide. Thermochim. Acta 273:231–238.

45. Krebs FC. 2009. Fabrication and processing of polymer solar cells: A review of printing and coating techniques. Sol. Energy Mater. Sol. Cells 93:394–412.

46. Kulkarni SA, Baikie T, Boix PP, Yantara N, Mathews N, Mhaisalkar SG. 2014. Band-gap tuning of lead halide perovskites using a sequential deposition process. J. Mater. Chem. A 2:9221–9225.

47. Kumar SG, Rao KSRK. 2014. Physics and chemistry of CdTe/CdS thin film heterojunction photovoltaic devices: fundamental and critical aspects. Energy Environ. Sci. 7:45–102.

48. Langmuir I. 1913. The vapor pressure of metallic tungsten. Phys. Rev. 2:329–342.

49. Lee MM, Teuscher J, Miyasaka T, Murakami TN, Snaith HJ. 2012. Efficient hybrid solar cells based on meso-superstructured organometal halide perovskites. Science (80-.). 338:643–647.

50. Leijtens T, Eperon GE, Pathak S, Abate A, Lee MM, Snaith HJ. 2013. Overcoming ultraviolet light instability of sensitized TiO2 with meso-superstructured organometal tri-halide perovskite solar cells. Nat. Commun. 4:2885. [accessed 2013 Dec 11]. http://www.ncbi.nlm.nih.gov/pubmed/24301460

51. Leyden MR, Lee MV, Raga SR, Qi Y. 2015. Large formamidinium lead trihalide perovskite solar cells using chemical vapor deposition with high reproducibility and tunable chlorine concentrations. J. Mater. Chem. A 3:16097–16103.

52. Leyden MR, Ono LK, Raga SR, Kato Y, Wang S, Qi Y. 2014. High performance perovskite solar cells by hybrid chemical vapor deposition. J. Mater. Chem. A 2:18742–18745.

53. Liang G-X, Fan P, Luo J-T, Gu D, Zheng Z-H. 2015. A promising unisource thermal evaporation for in situ fabrication of organolead halide perovskite CH3NH3PbI3 thin film. Prog. Photovoltaics Res. Appl. 20.

54. Lide DR, editor. 2005. CRC handbook of chemistry and physics, internet version. Boca Raton, FL: CRC Press.

55. Liu M, Johnston MB, Snaith HJ. 2013. Efficient planar heterojunction perovskite solar cells by vapour deposition. Nature 501:395–8.

56. Loi MA, Hummelen JC. 2013. Hybrid solar cells: perovskites under the sun. Nat. Mater. 12:1087–9.

57. Luo P, Liu Z, Xia W, Yuan C, Cheng J, Lu Y. 2015. Uniform, stable, and efficient planar-heterojunction perovskite solar cells by facile low-pressure chemical vapor deposition under fully open-air conditions. ACS Appl. Mater. Interfaces 7:2708–2714.

58. Ma Y, Zheng L, Chung Y-H, Chu S, Xiao L, Chen Z, Wang S, Qu B, Gong Q, Wu Z, et al. 2014. A highly efficient mesoscopic solar cell based on CH3NH3PbI3-xClx fabricated via sequential solution deposition. Chem. Commun.:5–8.

59. Marrero TR, Mason EA. 1972. Gaseous diffusion coefficients. J. Phys. Chem. Ref. Data 1:3.

60. Mattox DM. 2010. Introduction. In: Mattox DM, editor. Handbook of Physical Vapor Deposition (PVD) Processing. 2nd ed. Boston: William Andrew Publishing. p. 1–24.

61. McCandless I.; Birkmire, R. W. BE. Y. 1999. Optimization of vapor post-deposition processing for evaporated CdS/CdTe solar cells. Prog. Photovoltaics Res. Appl. 7:21–30.

62. Mitzi DB. 2001. Templating and structural engineering in organic–inorganic perovskites. J. Chem. Soc. Dalt. Trans.:1–12.

63. Mooney JB, Radding SB. 1982. Spray pyrolysis processing. Annu. Rev. Mater. Sci. 12:81–101.

64. Murugadoss G, Tanaka S, Mizuta G, Kanaya S, Nishino H, Umeyama T, Imahori H, Ito S. 2015. Light stability tests of methylammonium and formamidinium Pb-halide perovskites for solar cell applications. Jpn. J. Appl. Phys. 54:08KF08.

65. National Institute of Standards and Technology. 2016. Thermophysical properties of argon. NIST Chem. Webb.

66. Nicolas X, Mojtabi A, Platten JK. 1997. Two-dimensional numerical analysis of the poiseuille–bénard flow in a rectangular channel heated from below. Phys. Fluids 9:337.

67. Noel NK, Stranks SD, Abate A, Wehrenfennig C, Guarnera S, Haghighirad A-A, Sadhanala A, Eperon GE, Pathak SK, Johnston MB, et al. 2014. Lead-free organic-inorganic tin halide perovskites for photovoltaic applications. Energy Environ. Sci. 7:3061–3068.

68. NREL. 2016. National Center for Photovoltaics. United States Dep. Energy.

69. Ono LK, Leyden MR, Wang S, Qi Y. 2016. Organometal halide perovskite thin films and solar cells by vapor deposition. J. Mater. Chem. A.

70. Peng Y, Jing G, Cui T. 2015. High performance perovskite solar cells through vapor deposition with optimized PbI2 precursor films. RSC Adv. 5:95847–95853.

71. Petrović M, Chellappan V, Ramakrishna S. 2015. Perovskites: solar cells & engineering applications – materials and device developments. Sol. Energy 122:678–699.

72. Poling BE, Prausnitz JM, O'Connell JP. 2000. Properties of gases and liquids. 5th ed. New York: McGraw-Hill Professional.

73. Ponseca CS, Savenije TJ, Abdellah M, Zheng K, Yartsev A, Pascher T, Harlang T, Chabera P, Pullerits T, Stepanov A, et al. 2014. Organometal halide perovskite solar cell materials rationalized: ultrafast charge generation, high and microsecond-long balanced mobilities, and slow recombination. J. Am. Chem. Soc. 136:5189–5192.

74. Ramesh M, Boopathi KM. 2015. Using an airbrush pen for layer-by-layer growth of continuous perovskite thin films for hybrid solar cells Using an airbrush pen for layer-by-layer growth of continuous perovskite thin films for hybrid solar cells.

75. Sadhanala A, Deschler F, Thomas TH, Dutton SE, Goedel KC, Hanusch FC, Lai ML, Steiner U, Bein T, Docampo P, et al. 2014. Preparation of single-phase films of CH3NH3Pb(I 1– x Br x)3 with sharp optical band edges. J. Phys. Chem. Lett. 5:2501–2505.

76. Saliba M, Tan KW, Sai H, Moore DT, Scott T, Zhang W, Estroff LA, Wiesner U, Snaith HJ. 2014. Influence of thermal processing protocol upon the crystallization and photovoltaic performance of organic–inorganic lead trihalide perovskites. J. Phys. Chem. C 118:17171–17177.

77. Sandler SI. 2010. An introduction to applied statistical thermodynamics. New York: John Wiley & Sons.

78. Schmidtke J. 2010. Commercial status of thin-film photovoltaic devices and materials. Opt. Express 18:A477.

79. Sessolo M, Momblona C, Gil-Escrig L, Bolink HJ. 2015. Photovoltaic devices employing vacuum-deposited perovskite layers. MRS Bull. 40:660–666.

80. Siddiqi MA, Atakan B. 2007. Combined experiments to measure low sublimation pressures and diffusion coefficients of organometallic compounds. Thermochim. Acta 452:128–134.

81. Smecca E, Numata Y, Deretzis I, Pellegrino G, Boninelli S, Miyasaka T, La Magna A, Alberti A. 2016. Stability of solution-processed MAPbI 3 and FAPbI 3 layers. Phys. Chem. Chem. Phys. 18:13413–13422.

82. Snaith HJ. 2013. Perovskites: The Emergence of a New Era for Low-Cost, High-Efficiency Solar Cells. J. Phys. Chem. Lett. 4:3623–3630.

83. Soltanmohammad S, Berg DM, Chen L, Kim K, Simchi H, Shafarman WN. 2014. Effect of sputtering sequence on the properties of Ag-Cu-In-Ga metal precursors and reacted (Ag,Cu)(In,Ga)Se2 films. 2014 IEEE 40th Photovolt. Spec. Conf. PVSC 2014:1707–1711.

84. Stranks SD, Burlakov VM, Leijtens T, Ball JM, Goriely A, Snaith HJ. 2014. Recombination kinetics in organic-inorganic perovskites: excitons, free charge, and subgap states. Phys. Rev. Appl. 2:34007.

85. Vieyra-Eusebio MT, Rojas A. 2011. Vapor pressures and sublimation enthalpies of nickelocene and cobaltocene measured by thermogravimetry. J. Chem. Eng. Data 56:5008–5018.

86. Wang B, Chen T. 2015. Exceptionally stable CH3NH3PbI3 films in moderate humid environmental condition. Adv. Sci.

87. Wang S, Ono LK, Leyden MR, Kato Y, Raga SR, Lee MV, Qi Y. 2015. Smooth perovskite thin films and efficient perovskite solar cells prepared by the hybrid deposition method. J. Mater. Chem. A 3:14631–14641.

88. Wilke CR, Lee CY. 1955. Estimation of diffusion coefficients for gases and vapors. Ind. Eng. Chem. 47:1253–1257.

89. Yamamuro O, Oguni M, Matsuo T, Suga H. 1986. Calorimetric and dilatometric studies on the phase transitions of crystalline CH3NH3I. J. Chem. Thermodyn. 18:939–954.

90. Yang D, Yang Z, Qin W, Zhang Y, Liu SF, Li C. 2015. Alternating precursor layer deposition for highly stable perovskite films towards efficient solar cells using vacuum deposition. J. Mater. Chem. A 3:9401–9405.

91. Yang Yu B, Elbuken C, Ren CL, Huissoon JP. 2011. Image processing and classification algorithm for yeast cell morphology in a microfluidic chip. J. Biomed. Opt. 16.

92. Zhou H, Chen Q, Yang Y. 2015. Vapor-assisted solution process for perovskite materials and solar cells. MRS Bull. 40:667–673.

93. Zhu Z, Bai Y, Zhang T, Liu Z, Long X, Wei Z, Wang Z, Zhang L, Wang J, Yan F, et al. 2014. High-performance hole-extraction layer of sol-gel-processed nio nanocrystals for inverted planar perovskite solar cells. Angew. Chemie - Int. Ed.:1–6.

Appendix A

DETAILED EXPERIMENTAL DESIGNS AND RESULTS

Surface Coverage of Spun-Cast $MAPbI_{3-x}Cl_x$ OHP Films

Table 18 Reproduction of explored parameters and alias structure generated by MINITAB statistical analysis software.

Thin-film thickness parameter	Factor	Low	High
Annealing time (minutes)	A	30	90
Annealing temperature (°C)	B	90	110
Spin coating speed (rpm)	C	3000	6000
Spin coating time (seconds)	D	30	60
Amount of coating (mL)	E	0.2	0.4

```
Fractional Factorial Split-Plot Design
 Factors:           5   Whole plots:             8   Resolution:    V
 Hard-to-change:    2   Runs per whole plot:     4   Fraction:    1/2
 Runs:             32   Whole-plot replicates:   2
 Blocks:            2   Subplot replicates:      1

Design Generators: E = ABCD
Hard-to-change factors: A, B
Whole Plot Generators: A, B

Alias structure

   I + ABCDE
   A + BCDE
   B + ACDE
   C + ABDE
   D + ABCE
   E + ABCD
   AB + CDE
   AC + BDE
   AD + BCE
   AE + BCD
   BC + ADE
   BD + ACE
   BE + ACD
   CD + ABE
   CE + ABD
   DE + ABC
```

Table 19 Run order, results for the 32 random experiments

Run Order	Blocks	Annealing Time (min)	Annealing Temp (°C)	Spin Speed (RPM)	Spin Time (s)	Amount (mL)	Surface coverage (%)
1	1	30	90	3000	30	0.4	63.7
2	1	30	90	6000	30	0.2	64.8
3	1	30	90	6000	60	0.4	61.1
4	1	30	90	3000	60	0.2	74.8
5	1	90	90	6000	30	0.4	60.3
6	1	90	90	6000	60	0.2	62.3
7	1	90	90	3000	60	0.4	69.1
8	1	90	90	3000	30	0.2	76.4
9	1	30	110	6000	30	0.4	69.8
10	1	30	110	3000	60	0.4	75.1
11	1	30	110	3000	30	0.2	85.7
12	1	30	110	6000	60	0.2	76.0
13	1	90	110	6000	30	0.2	78.5
14	1	90	110	6000	60	0.4	63.7
15	1	90	110	3000	30	0.4	80.0
16	1	90	110	3000	60	0.2	73.5
17	2	30	90	6000	30	0.2	69.3
18	2	30	90	3000	30	0.4	74.1
19	2	30	90	3000	60	0.2	64.0
20	2	30	90	6000	60	0.4	54.9
21	2	90	90	3000	60	0.4	58.5
22	2	90	90	6000	30	0.4	61.9
23	2	90	90	3000	30	0.2	75.2
24	2	90	90	6000	60	0.2	46.9
25	2	30	110	3000	30	0.2	71.8
26	2	30	110	6000	60	0.2	60.2
27	2	30	110	6000	30	0.4	64.8
28	2	30	110	3000	60	0.4	70.1
29	2	90	110	3000	60	0.2	66.4

30	2	90	110	3000	30	0.4	81.3
31	2	90	110	6000	60	0.4	65.3
32	2	90	110	6000	30	0.2	58.5

Analysis of Variance for Surface Coverage

Source	DF	Adj SS	Adj MS	F-Value	P-Value
Blocks	1	262.549	262.549	8.70	0.060
Annealing Time	1	15.810	15.810	0.52	0.521
Annealing Temp	1	334.023	334.023	11.07	0.045
Annealing Time*Annealing Temp	1	3.098	3.098	0.10	0.770
WP Error	3	90.485	30.162	0.82	0.506
Spin Speed	1	625.840	625.840	17.08	0.001
Spin Time (s)	1	277.388	277.388	7.57	0.018
Amount (mL)	1	28.648	28.648	0.78	0.394
Annealing Time*Spin Speed	1	18.918	18.918	0.52	0.486
Annealing Time*Spin Time (s)	1	45.859	45.859	1.25	0.285
Annealing Time*Amount (mL)	1	39.006	39.006	1.06	0.322
Annealing Temp*Spin Speed	1	1.555	1.555	0.04	0.840
Annealing Temp*Spin Time (s)	1	6.013	6.013	0.16	0.693
Annealing Temp*Amount (mL)	1	27.413	27.413	0.75	0.404
Spin Speed*Spin Time (s)	1	11.595	11.595	0.32	0.584
Spin Speed*Amount (mL)	1	0.053	0.053	0.00	0.970
Spin Time (s)*Amount (mL)	1	9.869	9.869	0.27	0.613
SP Error	12	439.608	36.634		
Total	31				

PbI_2 Deposition

Table 20 Reproduction of explored parameters in PbI_2 deposition case study and alias structure generated by MINITAB statistical analysis software (* = HTC Factor)

Deposition Variable	Factor	Low	High
Pressure (Torr)*	A	0.6	1.0
Source Temperature (°C)	B	375	385
Deposition height (mm)	C	2.83	3.83

```
Factors:           3   Whole plots:             4
Hard-to-change:    1   Runs per whole plot:     4
Runs:             16   Whole-plot replicates:   2
Blocks:            2   Subplot replicates:      1


Hard-to-change factors: A


Whole Plot Generators: A


All terms are free from aliasing.


Design Table (randomized)

Run  Blk  WP  A  B  C
  1    1   2  +  -  -
  2    1   2  +  +  +
  3    1   2  +  -  +
  4    1   2  +  +  -
  5    1   1  -  +  -
  6    1   1  -  -  +
  7    1   1  -  -  -
  8    1   1  -  +  +
  9    2   3  -  -  +
 10    2   3  -  +  -
 11    2   3  -  -  -
 12    2   3  -  +  +
```

13	2	4	+	-	+
14	2	4	+	+	+
15	2	4	+	+	-
16	2	4	+	-	-

Table 21 Full Results for PbI_2 Deposition Case Study with standard deviation included for mass loss and deposition flux

Run Order	Blocks	P_{sys} (Torr)	T_{source} (°C)	H (mm)	$T_{substrate}$ (°C)	ΔT (°C)	Source Mass Loss (g)	Substrate Mass Gain (g)	Difference (g)	J_{AB} (g/cm^2s)
1	1	1.0	375	2.83	115.50	260.5	-(5.3±0.1)E-03	(2.9±0.1)E-03	(2.4±0.1)E-03	-(4.4±0.1)E-06
2	1	1.0	385	3.83	106.80	279.2	-(3.8±0.2)E-03	(4.1±0.1)E-03	-(3.0±0.2)E-04	-(3.2±0.1)E-06
3	1	1.0	375	3.83	105.30	271.0	-(3.3±0.1)E-03	(3.1±0.3)E-03	(2.0±3.0)E-04	-(2.8±0.1)E-06
4	1	1.0	385	2.83	121.35	264.6	-1.0E-02	(9.6±0.1)E-03	(5.0±1.0)E-04	-(8.4±0.1)E-06
5	1	0.6	385	2.83	110.00	279.0	-3.3E-02	3.2E-02	(1.7±0.2)E-03	-2.8E-05
6	1	0.6	375	3.83	98.95	276.4	-1.9E-02	1.7E-02	(2.3±0.1)E-03	-1.6E-05
7	1	0.6	375	2.83	107.50	268.8	-1.5E-02	1.4E-02	(1.7±0.2)E-03	-1.3E-05
8	1	0.6	385	3.83	102.65	283.1	-2.1E-02	2.1E-02	-(1.0±2.0)E-04	-1.7E-05
9	2	0.6	375	3.83	97.10	278.5	-1.3E-02	1.0E-02	(2.6±0.1)E-03	-1.1E-05
10	2	0.6	385	2.83	108.00	278.4	-2.3E-02	2.1E-02	(2.2±0.1)E-03	-1.9E-05
11	2	0.6	375	2.83	101.35	274.6	-(7.9±0.2)E-03	(8.7±0.2)E-03	-(8.0±3.0)E-04	-6.6E-06
12	2	0.6	385	3.83	96.30	288.9	-1.4E-02	1.2E-02	(1.4±0.1)E-03	-1.1E-05
13	2	1.0	375	3.83	99.65	276.2	-(2.4±0.1)E-03	(3.2±0.2)E-03	-(8.0±2.0)E-04	-(2.0±0.1)E-06
14	2	1.0	385	3.83	100.70	285.5	-(7.5±0.1)E-03	(5.0±0.1)E-03	(2.5±0.1)E-03	-(6.3±0.1)E-06
15	2	1.0	385	2.83	118.20	267.9	-1.0E-02	(8.9±0.1)E-03	(1.5±0.1)E-03	-8.7E-06
16	2	1.0	375	2.83	115.15	261.2	-1.0E-02	(8.9±0.1)E-03	(1.5±0.1)E-03	-8.7E-06

MAI Deposition

Table 22 Full Results for MAI Deposition Case Study with standard deviation included for mass loss and deposition flux

Run Order	Block	P_{sys} (Torr)	T_{source} (°C)	$T_{substrate}$ (°C)	ΔT (°C)	Source Mass Loss (g)	Substrate Mass Gain (g)	Difference (g)	J_{AB} (g/cm^{2}s)
1	1	1.0	155	42.6	112.5	-(4.7±0.1)E-03	(6.0±1.0)E-04	(4.1±0.1)E-03	-(3.9±0.1)E-06
2	1	0.6	175	42.8	132.3	-(7.7±0.1)E-03	(2.0±0.1)E-03	(5.7±0.1)E-03	-(6.4±0.1)E-06
3	1	0.6	165	42.7	122.5	-(7.8±0.4)E-03	1.1E-03	(6.7±0.4)E-03	-(6.5±0.3)E-06
4	1	1.0	175	52.2	123.2	-(4.8±0.1)E-03	(1.7±0.2)E-03	(3.1±0.2)E-03	-(4.0±0.1)E-06
5	1	0.6	155	42.8	112.3	-(4.2±0.1)E-03	(3.0±3.0)E-04	(3.9±0.3)E-03	-(3.5±0.1)E-06
6	1	1.0	165	48.5	116.6	-(4.2±0.1)E-03	(1.2±0.1)E-03	(3.0±0.1)E-03	-(3.5±0.1)E-06
7	2	0.6	165	43.9	121.3	-(4.5±0.2)E-03	(1.1±0.1)E-03	(3.4±0.2)E-03	-(3.8±0.2)E-06
8	2	0.6	175	45.5	129.6	-(8.5±0.2)E-03	(1.8±0.1)E-03	(6.7±0.2)E-03	-(7.1±0.2)E-06
9	2	1.0	155	48.2	106.8	-(2.9±0.1)E-03	(4.0±0.1)E-04	(2.5±0.1)E-03	-(2.4±0.1)E-06
10	2	1.0	165	48.5	116.6	-(3.7±0.2)E-03	(1.0±0.2)E-03	(2.7±0.3)E-03	-(3.1±0.2)E-06
11	2	0.6	155	41.7	113.4	-(5.0±0.1)E-03	(4.0±1.0)E-04	(4.6±0.1)E-03	-(4.2±0.1)E-06
12	2	1.0	175	49.7	125.8	-(7.5±0.1)E-03	(8.0±4.0)E-04	(6.7±0.4)E-03	-(6.3±0.1)E-06

Appendix B

DETAILED REGRESSION ANOVA RESULTS FROM MINITAB

Regression Analysis Report for MAI Preliminary CSVT Data

Analysis of Variance

Source	DF	Adj SS	Adj MS	F-Value	P-Value
Regression	1	0.256343	0.256343	1156.48	0.019
1/T (1/K)	1	0.256343	0.256343	1156.48	0.019
Error	1	0.000222	0.000222		
Total	2	0.256565			

Model Summary

S	R-sq	R-sq(adj)	R-sq(pred)
0.0148882	99.91%	99.83%	98.83%

Coefficients

Term	Coef	SE Coef	T-Value	P-Value	VIF
Constant	4.093	0.456	8.98	0.071	
1/T (1/K)	-6713	197	-34.01	0.019	1.00

Regression Equation

ln (P2/P1) = 4.093 - 6713 1/T (1/K)

Regression Analysis Report for MAI TGA Mass Loss Data

Analysis of Variance

Source	DF	Adj SS	Adj MS	F-Value	P-Value
Regression	1	16.8873	16.8873	166.77	0.001
1/T (1/K)	1	16.8873	16.8873	166.77	0.001
Error	3	0.3038	0.1013		
Total	4	17.1911			

Model Summary

S	R-sq	R-sq(adj)	R-sq(pred)
0.318214	98.23%	97.64%	92.17%

Coefficients

Term	Coef	SE Coef	T-Value	P-Value	VIF
Constant	1.64	1.66	0.99	0.396	
1/T (1/K)	-8500	658	-12.91	0.001	1.00

Regression Equation

LN (P2/P1) = 1.64 - 8500 1/T (1/K)

Appendix C

PERMISSION FORMS FOR REPRODUCED FIGURES

Figure 1

ROYAL SOCIETY OF CHEMISTRY LICENSE

TERMS AND CONDITIONS

Jun 28, 2016

This Agreement between Trishelle Copeland ("You") and Royal Society of Chemistry ("Royal Society of Chemistry") consists of your license details and the terms and conditions provided by Royal Society of Chemistry and Copyright Clearance Center.

License Number 3897941171715

License date Jun 28, 2016

Licensed Content Publisher Royal Society of Chemistry

Licensed Content Publication Journal of the Chemical Society Dalton Transactions

Licensed Content Title Templating and structural engineering in organic–inorganic perovskites

Licensed Content Author David B. Mitzi

Licensed Content Date Dec 5, 2000

Licensed Content Issue Number 1

Type of Use Thesis/Dissertation

Requestor type academic/educational

Portion figures/tables/images

Number of figures/tables/images 1

Format print and electronic

Distribution quantity 1

Will you be translating? no

Order reference number

Title of the thesis/dissertation Deposition of Methylammonium Lead Tri-Iodide Organometallic Halide Perovskites using Close Space Vapor Transport

Expected completion date Jul 2016

Estimated size 200

Requestor Location Trishelle Copeland-Johnson

Institute of Energy Conversion

451 Wyoming Road

NEWARK, DE 19716

United States

Attn: Trishelle Copeland-Johnson

Billing Type Invoice

Billing Address Trishelle Copeland-Johnson

Institute of Energy Conversion

451 Wyoming Road

NEWARK, DE 19716
United States
Attn: Trishelle Copeland-Johnson

Total 0.00 USD

Terms and Conditions

This License Agreement is between {Requestor Name} ("You") and The Royal Society of Chemistry ("RSC") provided by the Copyright Clearance Center ("CCC"). The license consists of your order details, the terms and conditions provided by the Royal Society of Chemistry, and the payment terms and conditions.

RSC / TERMS AND CONDITIONS
INTRODUCTION

For suggestions or comments regarding this order, contact Rightslink Customer Support: customercare@copyright.com or +1-855-239-3415 (toll free in the US) or +1-978-646-2777.

Questions? customercare@copyright.com or +1-855-239-3415 (toll free in the US) or +1-978-646-2777.

Figures 2 and 3

NATURE PUBLISHING GROUP LICENSE

TERMS AND CONDITIONS

Jun 28, 2016

This Agreement between Trishelle Copeland ("You") and Nature Publishing Group ("Nature Publishing Group") consists of your license details and the terms and conditions provided by Nature Publishing Group and Copyright Clearance Center.

License Number	3897950938392
License date	Jun 28, 2016
Licensed Content Publisher	Nature Publishing Group
Licensed Content Publication	Nature Materials
Licensed Content Title	Hybrid solar cells: Perovskites under the Sun
Licensed Content Author	Maria Antonietta Loi, Jan C. Hummelen
Licensed Content Date	Nov 21, 2013
Licensed Content Volume Number	12
Licensed Content Issue Number	12
Type of Use	reuse in a dissertation / thesis
Requestor type	academic/educational
Format	print and electronic
Portion	figures/tables/illustrations

Number of figures/tables/illustrations 1

High-res required no

Figures Figure 2

Author of this NPG article no

Your reference number

Title of your thesis / dissertation Deposition of Methylammonium Lead Tri-Iodide Organometallic Halide Perovskites using Close Space Vapor Transport

Expected completion date Jul 2016

Estimated size (number of pages) 200

Requestor Location Trishelle Copeland-Johnson

Institute of Energy Conversion

451 Wyoming Road

NEWARK, DE 19716

United States

Attn: Trishelle Copeland-Johnson

Billing Type Invoice

Billing Address Trishelle Copeland-Johnson

Institute of Energy Conversion

451 Wyoming Road
NEWARK, DE 19716
United States
Attn: Trishelle Copeland-Johnson

Total 0.00 USD

Terms and Conditions

Terms and Conditions for Permissions

Nature Publishing Group hereby grants you a non-exclusive license to reproduce this material for this purpose, and for no other use, subject to the conditions below:

1. NPG warrants that it has, to the best of its knowledge, the rights to license reuse of this material. However, you should ensure that the material you are requesting is original to Nature Publishing Group and does not carry the copyright of another entity (as credited in the published version). If the credit line on any part of the material you have requested indicates that it was reprinted or adapted by NPG with permission from another source, then you should also seek permission from that source to reuse the material.

2. Permission granted free of charge for material in print is also usually granted for any electronic version of that work, provided that the material is incidental to the work as a whole and that the electronic version is essentially equivalent to, or substitutes for, the print version. Where print permission has been granted for a fee, separate permission must be obtained for any additional, electronic re-use (unless, as in the case of a full paper, this has already been accounted for during your initial request in the calculation of a print run).NB: In all cases, web-based use of full-text articles must be authorized separately through the 'Use on a Web Site' option when requesting permission.

3. Permission granted for a first edition does not apply to second and subsequent editions and for editions in other languages (except for signatories to the STM Permissions Guidelines, or where the first edition permission was granted for free).

4. Nature Publishing Group's permission must be acknowledged next to the figure, table or abstract in print. In electronic form, this acknowledgement must be visible at the same time as the figure/table/abstract, and must be hyperlinked to the journal's homepage.

5. The credit line should read:
   Reprinted by permission from Macmillan Publishers Ltd: [JOURNAL NAME] (reference citation), copyright (year of publication) For AOP papers, the credit line should read:
   Reprinted by permission from Macmillan Publishers Ltd: [JOURNAL NAME], advance online publication, day month year (doi: 10.1038/sj.[JOURNAL ACRONYM].XXXXX)
   Note: For republication from the *British Journal of Cancer,* the following credit lines apply.

Reprinted by permission from Macmillan Publishers Ltd on behalf of Cancer Research UK: [JOURNAL NAME] (reference citation), copyright (year of publication)For AOP papers, the credit line should read:
Reprinted by permission from Macmillan Publishers Ltd on behalf of Cancer Research UK:
[JOURNAL NAME], advance online publication, day month year (doi: 10.1038/sj.[JOURNAL ACRONYM].XXXXX)

6. Adaptations of single figures do not require NPG approval. However, the adaptation should be credited as follows:

   Adapted by permission from Macmillan Publishers Ltd: [JOURNAL NAME] (reference citation), copyright (year of publication)
   Note: For adaptation from the *British Journal of Cancer,* the following credit line
   applies.
   Adapted by permission from Macmillan Publishers Ltd on behalf of Cancer Research UK:
   [JOURNAL NAME] (reference citation), copyright (year of publication)
7. Translations of 401 words up to a whole article require NPG approval. Please visit http://www.macmillanmedicalcommunications.com for more information.Translations of up to a 400 words do not require NPG approval. The translation should be credited as follows:

   Translated by permission from Macmillan Publishers Ltd: [JOURNAL NAME] (reference citation), copyright (year of publication).
   Note: For translation from the *British Journal of Cancer,* the following credit line applies.
   Translated by permission from Macmillan Publishers Ltd on behalf of Cancer Research UK:
   [JOURNAL NAME] (reference citation), copyright (year of publication)

We are certain that all parties will benefit from this agreement and wish you the best in the use of this material. Thank you.
Special
Terms: v1.1

Questions? customercare@copyright.com or +1-855-239-3415 (toll free in the US) or +1-978-646-2777.